Republic of Iraq
Ministry of Higher Education & Scientific Research
University of Babylon
College of Education for Pure Sciences
Department of Physics

Fabrication and Analysis of New Nanocomposites Use in Bioenvironmental Applications

A thesis

Submitted to the Council of the College of Education for Pure Sciences

University of Babylon in Partial Fulfillment of the Requirements for the

Degree of Doctorate of Philosophy in Education/ Physics

By

Dhay Ali Sabur Ali

B. Sc. in Physics
(University of Babylon, 2009)
M. Sc. in Physics
(University of Bucharest, 2018)

Supervised by

Prof. Dr Majeed Ali Habeeb **Prof. Dr Ahmed Hashim Mohaisen**

2023 A.D. **1445A.H**

بسم الله الرحمن الرحيم

﴿ آتُونِي زُبَرَ الْحَدِيدِ ۖ حَتَّىٰ إِذَا سَاوَىٰ بَيْنَ الصَّدَفَيْنِ قَالَ انفُخُوا ۖ حَتَّىٰ إِذَا جَعَلَهُ نَارًا قَالَ آتُونِي أُفْرِغْ عَلَيْهِ قِطْرًا ﴾

صدق الله العلي العظيم

سورة الكهف ٩٦

Acknowledgements

In the name of Allah the Merciful. I thank God, Lord of Earth and Heaven, for completing my research. I would like to express my thanks and gratitude to my supervisors ***(Dr. Majed Ali Habeeb , Dr. Ahmed Hashim Mohaisen)*** *for suggesting this topic to me and for his distinguished efforts, advice and sound guidance that helped alleviate all the difficulties I encountered during my work.*

Thank you to the Deanship of the College of Education for Pure Sciences / University of Babylon and the Department of Physics for giving me this opportunity to complete my research. I also would like to express my grateful thanks to all lecturers, instructors, and students of the Department of Physics for their assistance.

Finally, many thanks go to those who support me and alleviate difficulties I have faced during my work and to everyone who helped me in a way or another during my preparation of this thesis,. I wish success to all.

Dhay ..✍

Dedication

To the soul of my father

To my mother

TO my husband

To my daughters (Aya &Zainab)

To my brother's and sister

To my close friends

and

Everyone who has helped me …

With my Respect

Dhay ..✍

Summary

This study include two types of (polymethyl methacrylate-polycarbonate / indium trioxide - graphene oxide) (PMMA-PC/In_2O_3-GO) and (polymethyl methacrylate-polycarbonate / antimony trioxide - graphene oxide) (PMMA-PC/Sb_2O_3-GO) nanocomposites were prepared by solution casting method. The (PMMA-PC) blend was prepared for different concentrations (80 wt.%)PMMA and (20 wt.%) PC as well indium trioxide, antimony trioxide, and graphene nanoparticles were added to (PMMA-PC) blend with different weight percentages as (1.4, 2.8, 4.2 and 5.6) wt.%. The effect of indium trioxide, antimony trioxide, and graphene nanoparticle additives on structural, A.C electrical, and optical properties of (the PMMA-PC) blend were studied. Photodegradation and antibacterial activities applications were fabricated.

Optical microscope and scanning electron microscope images indicate that the indium trioxide, antimony trioxide, and graphene nanoparticle additives distribution was homogeneous in the blend. The XRD patterns of the prepared pure Sb_2O_3, In_2O_3, and GO nanoparticles show three peaks near 13.70°, 26°, and 30.8° which were matched to (111), (222), and (400) reflections of (Sb_2O_3) respectively, and three peaks corresponding to (100), (400), and (440) directions of the cubic In_2O_3 crystal structure which is corresponding to the positions 2θ = 29.9 o, 34.1 o, and 47.8o respectively. The XRD pattern of graphene oxide shows a peak at 2θ = 10.1° (d-spacing of 8.9 Å), the (100) diffraction peak at 2θ = 43.0° according to a d-spacing of 2.13 Å. FT-IR indicates that no change in chemical structures between the blend and the additives.

The optical properties of (PMMA-PC/In_2O_3-GO) and (PMMA-PC/Sb_2O_3-GO) nanocomposites showed that the absorbance, absorption coefficient, extinction coefficient, refractive index, and real and imaginary dielectric constants of the PMMA-PC blend increased with higher nanoparticle

concentrations. Conversely, transmittance and the energy gap decreased with increasing concentrations of indium trioxide, antimony trioxide, and graphene oxide nanoparticles.

The A.C. electrical properties of the nanocomposites were studied within a frequency range (100Hz-5MHz), revealing that the dielectric constant, dielectric loss, and A.C. electrical conductivity increased with higher concentrations of nanoparticles. Additionally, the dielectric constant and dielectric loss decreased with increasing frequency, while A.C. electrical conductivity increased. Regarding to the applications, the nanocomposites exhibited photocatalytic activity, with the ability to decrease the concentration of MO dye as the additive concentrations increased. The kinetics of methyl orange (MO) dye decay were analyzed using the Langmuir-Hinshelwood model, and a minimum half-life period of 38 minutes was observed. The nanocomposites also showed antibacterial properties against gram-positive *(S. aureus)* and gram-negative *(E. coli)* bacteria, with the inhibition zone increasing with increasing concentrations of indium trioxide, antimony trioxide, and graphene oxide nanoparticles.

Contents

List of Figures

List of Tables

List of abbreviations and Symbols

Definition	Items
A. C electrical conductivity	$\sigma_{A.C}$
Absorbance	A
Absorbance of MO Dye after Irradiation	X_1
Absorbed Light Intensity	I_A
Absorption Coefficient	α
Angular Frequency	w
Antimony Trioxide	Sb_2O_3
Complex permittivity	ε^*
Complex Refractive Index	n^*
Conduction Band	$C.B$
Degradation Percentage	D_{MO}
Dielectric Constant	$\acute{\varepsilon}$
Dielectric Loss	ε''
Displacement factor	D
Electron	e^-
Escherichia Coli	$E.coli$
Extinction Coefficient	k
Fourier Transform-Infrared Radiation	$FT\text{-}IR$
Frequency	v

Glass Transition	T_g
Graphene Oxide	GO
Hole	h^+
Hydrogen Peroxide	H_2O_2
Hydroxyl Radical	$OH^{\bullet}$
Hyper Oxide Radical	$HO_2^{\bullet}$
Imaginary Dielectric Constant	ε_2
Incident intensity of Light	I_o
Indium Trioxide	In_2O_3
Initial Absorbance of MO Dye	X_0
Lattice Constants	a,b,c
melting Temperature	T_m
Methylene Orange Dye	MO
Nanoparticles	NPs
Optical Conductivity	σ_{opt}
Optical Energy Gap	$E_g^{opt.}$
Parallel capacitance	C_p
Permittivity in the Free Space.	ε_o
Phonon Energy	E_{ph}
Photon Energy	$h\upsilon$
Photon Wavelength	λ
Planck's Constant	h
Polycarbonate	PC
Polymethyl methacrylate	$PMMA$

Real Dielectric Constant	ε_1
Reflectance	*R*
Refractive Index	*n*
Scanning Electron Microscopy	*SEM*
Staphylococcus Aureus	*S.aureus*
Superoxide Radical Anion	$O_2^{\bullet -}$
The imaginary part of the complex permittivity	ε_b
The real part of the complex permittivity	ε_a
Thickness of the Sample	*t*
Transmittance	*T*
Ultra-Violet	*UV*
Vacuum capacitor	C_0
Valence Band	*V.B*
Velocity of Light	*C*
Wave Number	*K*
X-Ray Diffraction	*XRD*

1.1 Introduction

The science of nanoscale measurement is known as nanoscience. Nanotechnology and nanoscience include the ability to regulate the movement of atoms and molecules at the nanoscale to form substances, composites, components, and devices.Scientists have concluded that materials with nano sizes, such as small particles and thin films, can have different properties than materials with larger sizes. Nanotechnology applications have been overgrown recently, with materials with the most significant potential, followed by electronics and medicine .Promises for improved structures, devices, and materials. For example, silver may be considered nontoxic,but when converted into nanoparticles, it can kill viruses when in contact with them [1].

Furthermore, its characteristics, such as colour, electrical conductivity, and strength, change when a material becomes nanosized .When metal is converted to the nanoscale level, it can become an insulator or a semiconductor understanding these various promises for improved structures, devices, and materials. Nanomaterials exhibit unique physical, chemical, and biological properties that are a result of their small size. One of the most significant properties of nanomaterials is their high surface area-to-volume ratio. Because of this, nanomaterials have many atoms on their surface compared to their interior, which results in enhanced reactivity[2]. This increased reactivity is helpful in catalysis and chemical sensing applications. Nanomaterials also exhibit size-dependent electronic, optical, and magnetic properties. For example, some nanomaterials, such as quantum dots and nanowires, have tunable electronic properties that depend on size and shape. This property makes them useful in electronics applications such as solar cells, transistors, and sensors[3]. Nanomaterials also have unique optical properties, such as plasmonic resonance, utilized in sensing and imaging applications. In addition to these properties, nanomaterials can also be designed to have specific

chemicals and properties. Nanomaterials can also be designed to have specific chemical and physical properties by controlling their size, shape, composition, and surface chemistr [4].This level of control allows for the synthesis of nanomaterials with tailored properties for specific applications. Nanomaterials have many potential applications in various fields, such as electronics, medicine, energy, catalysis, and environmental remediation. In electronics, nanomaterials are being developed to create smaller, faster, and more efficient devices. For example, carbon nanotubes have created field-effect transistors and memory devices. In addition, quantum dots and nanowires are being used to develop solar cells, light-emitting diodes, and sensors. In medicine, nanomaterials have been used to create targeted drug delivery systems, imaging agents, and sensors [5].These nanomaterials are designed to selectively target and deliver drugs to specific cells or tissues, minimizing the side effects of the drug on healthy cells. In addition, nanomaterials have been used in medical imaging to improve the accuracy of diagnosis and treatment. Nanomaterials are also being developed for energy applications such as solar cells, batteries, and fuel cells. For example, nanomaterials such as titanium dioxide and zinc oxide have been used as photocatalysts in solar cells to improve their efficiency. Nanomaterials are also being investigated for use in energy storage applications such as batteries and supercapacitors.In catalysis, nanomaterials have been used as catalysts in various chemical reactions. Nanomaterials high surface area to volume ratio allows for enhanced reactivity and selectivity in catalytic reactions. Nanomaterials also used in environmental remediation applications to remove pollutants from water and air. Despite the numerous potential applications of nanomaterials, their unique properties also pose potential risks to human health and the environment[6].

The small size of nanomaterials allows them to easily enter the body through inhalation, ingestion, or skin absorption [7]. Once inside the body, nanomaterials can interact with cells and tissues, potentially causing toxicity, inflammation, and other adverse effects.The following are some of the potential applications of nanotechnology [8]:

- Highly effective drugs and precisely targeted drug delivery.
- Microsensors and diagnostic tools for effective health.
- Dressings and coatings that are antibacterial.
- Thin protective coatings and nanocomposite polymers for structural and electronic applications.
- Filters for cost-effective water desalination.
- Barriers to optical and thermal applications.
- Non-volatile memory, miniaturized computers.
- Materials that are ultra-lightweight, strong, and precisely forme.

1.2 The Structure of Polymer

The physical characteristics of polymer materials depend on molecular weight, shape, and structure. The different types of polymer chains are shown in Figure (1.1):

1. Linear polymers: Van der Waals bonding between chains. Examples: polyethylene and nylon.

2. Branched polymers: chain packing efficiency is reduced compared to linear polymers .

3. Cross-linked polymers: chain is connected by covalent bonds. Often, it is achieved by adding atoms or molecules that form covalent links between chains. Many rubbers have this structure.

4.Network polymers: 3D networks made from trifunctional mers. Examples: epoxies and phenol-formaldehyde [9].

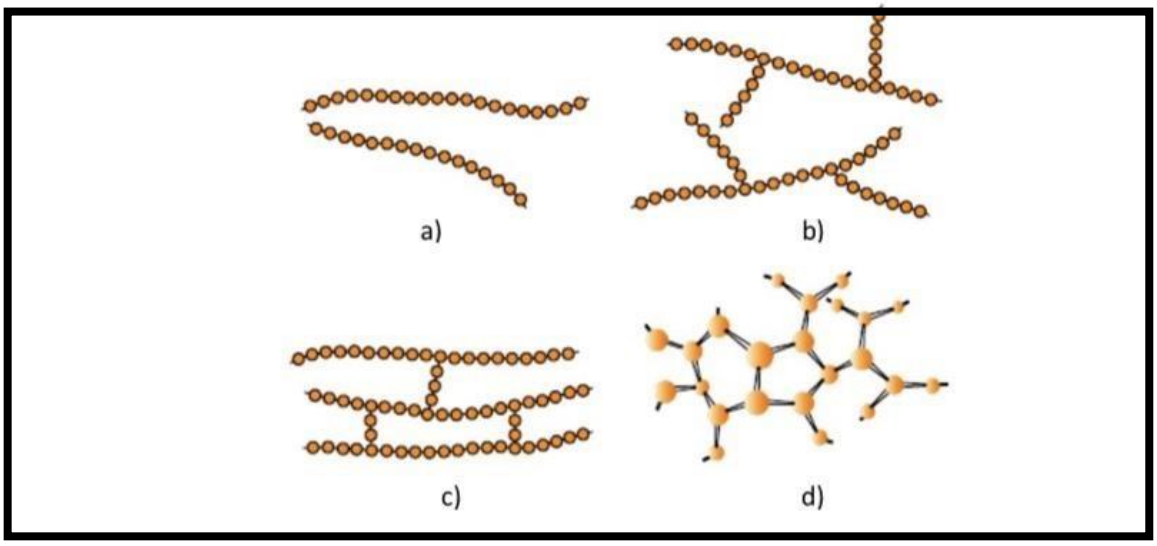

Figure (1.1) Polymer Chains [10].

a) Linear polymers b) Branched polymers

c) Cross-linked d) Network polymers

1.3 Biopolymers

Biopolymers are natural polymers derived from plants, animals, and microorganisms. These polymers are made up of monomers that are linked together to form long chains, just like synthetic polymers. However, biopolymers are unique because they are biodegradable, renewable, and environmentally friendly [11]. Here are some of the types and applications of biopolymers:

1- Proteins: Proteins are a type of biopolymer made up of amino acids. They are found in many living organisms, including animals, plants, and microorganisms. As a result, proteins have various applications in various industries, including food, pharmaceuticals, and cosmetics. For example, proteins such as collagen and gelatin are used in the food industry to improve food products' texture and nutritional value [12].

2- Polysaccharides: polysaccharides are a type of biopolymer made up of sugar molecules. They are found in many living organisms, including plants, animals, and microorganisms[13]. As a result, polysaccharides have a wide range of applications in various industries, including food, textiles, and pharmaceuticals. For example, polysaccharides such as cellulose and starch are used in the food industry as thickeners and stabilizers [14].

3- Nucleic Acids: nucleic acids are a type of biopolymer made up of nucleotides. They are found in all living organisms and play a crucial role in storing and transmitting genetic information. As a result, nucleic acids have a wide range of applications in the pharmaceutical and biotechnology industries. For example, nucleic acids such as DNA and RNA are used to develop vaccines and gene therapy [15].

4- Polyesters: Polyesters are a type of biopolymer made up of repeating units of ester groups. They are found in many living organisms, including plants and bacteria. As a result, polyesters have various applications in various industries, including textiles, packaging, and biomedical engineering. For example, polyesters such as polylactic acid (PLA) produce biodegradable packaging materials [16].

5- Polyhydroxyalkanoates (PHAs): PHAs are a type of biopolymer produced by some bacteria as a storage material. They are biodegradable and have properties similar to petroleum-based plastics. PHAs have various applications in various industries, including packaging, biomedical engineering, and agriculture. For example, PHAs such as polyhydroxybutyrate (PHB) produce biodegradable packaging materials. The biopolymers have a wide range of applications in various industries due to their unique properties, such as biodegradability and renewability [17]. The ability to produce biopolymers from renewable resources such as plants and bacteria has made them an essential part of modern material

science. The biopolymer applications are expected to grow as new materials with improved properties are developed**.** In today's world, biopolymers are a promising candidate for mitigating negative environmental effects, which is why a variety of industrial fields, such as nanotechnology, are interested in biopolymers to develop electrospun nanofibrous membranes for their eco-friendliness, sustainability, renewable nature, degradability, biocompatibility, and, most importantly, they have no detrimental effect on human health and our habitat universe[11].Biopolymers are polymers usually created during all organisms' growth periods. As a result, they are also known as natural polymers [15].Complex metabolic reactions within cells produce them. Cellulose and starch are the most exciting materials for material applications. However, there is growing interest in more complex hydrocarbon polymers produced by bacteria and fungi, particularly polysaccharides like xanthan, pullulan, chitin, chitosan, and hyaluronic acid. Biodegradable polymers are becoming increasingly important, and current research focuses on developing newer biodegradable polymers. Many biodegradable polymers have been synthesized or formed typically during all organisms' growth periods [19].

1.4 The Polymers Blends

The development of polymer blends is essential as it offers a means of overcoming the limitations of individual polymers. The properties of the polymer blends depend on the chemical structure and molecular weight of the polymers, as well as the blend's processing conditions. The use of polymer blended allows for the combination of desirable properties of different polymers, such as mechanical strength, thermal stability, chemical resistance, and optical, leading to the formation of new materials with superior properties. The blending of polymers can be done through various methods [20]. One of the most common methods is solution blending, which involves dissolving them in a common solvent and mixing them together

[21]. The resulting solution is then evaporated to obtain the final product. Solution blending for blending polymers with different or incompatible melting points. Polymer blends have several advantages over individual polymers.One of the significant benefits of polymer blends is the ability to improve the properties of the resulting material. For example, blending polypropylene (PP) with high-density polyethylene (HDPE) results in a material with improved mechanical properties, such as impact resistance and tensile strength[22].Another method of blending polymers is melt blending, which involves mixing the polymers in the melt state. This process is carried out by heating the polymers above their melting point and then mixing them together. The resulting blend is then cooled and solidified to obtain the final product. Melt blending is a simple and cost-effective method of producing polymer blends. Adding a small amount of a compatibilizer, a third polymer added to the blend to improve the compatibility between the two polymers, can significantly enhance the properties of the blend. Polymer blends can be classified into three categories: miscible blends, immiscible blends, and interpenetrating polymer networks (IPNs). Miscible blends refer to blends in which two or more polymers are completely soluble in each other. This results in a uniform material with unique properties.Immiscible blends, on the other hand, refer to blends in which the polymers are not soluble in each other. This results in a material with distinct phases, each with its properties. IPNs refer to blends in which two or more polymers are cross-linked to each other, resulting in a material with unique properties. Miscible polymer blends have several advantages over immiscible blends. For example, miscible blends result in a material with uniform properties and a single glass transition temperature (Tg), making it easier to process[23]. On the other hand, immiscible blends have distinct phases that can result in poor mechanical properties, such as reduced impact strength[24]. However, immiscible blends have unique properties that can benefit specific

applications. The properties of polymer blends are determined by various factors, including the chemical structure and molecular weight of the polymers, the compatibility of the polymers, and the processing conditions[25].

1.5 Nanocomposites

Nanocomposites are materials made by combining a polymer matrix with nanoparticles or nanofibers. These materials have unique properties that make them useful in various applications. The most common type of nanocomposite is the polymer nanocomposite, a polymer matrix reinforced with nanoparticles. Nanoparticles can be made from various materials, including metals, metal oxides, carbon nanotubes, and graphene [26]. These nanoparticles are typically less than 100 nm in size, and when incorporated into a polymer matrix, can significantly improve the material's properties. For example, adding nanoparticles to a polymer matrix can increase the material's strength, stiffness, thermal stability, and electrical conductivity [27].

There are several types of nanocomposites, including:

1. Carbon Nanotube Nanocomposites: Carbon nanotubes are long, cylindrical structures made of carbon atoms. When added to a polymer matrix, they can significantly improve the material's mechanical properties, including strength and stiffness. Carbon nanotube nanocomposites are used in a variety of applications, including aerospace, automotive, and electronics [28].
2. Metal Oxide Nanocomposites: Metal oxide nanoparticles, such as titanium dioxide and zinc oxide, can be added to a polymer matrix to improve the material's properties. Metal oxide nanocomposites are used in various applications, including coatings, sensors, and biomedical implants [29].
3. Ceramic Nanocomposites: in ceramic nanocomposites, the matrix material is a ceramic, and the nanoparticles are typically ceramic or metallic. The addition of nanoparticles improves the mechanical, thermal, or electrical

properties of the ceramic matrix [27].

4. Polymer Nanocomposites: These are nanocomposites in which the matrix material is a polymer. The nanoparticles dispersed within the polymer matrix can be metal nanoparticles, such as silver or gold, or inorganic nanoparticles, such as clay or silica nanoparticles [28].

1.6 Polymer Nanocomposite

Polymer nanocomposites have been widely investigated not for their numerous fields but to understand their physical properties. In light of these Studies, it was observed that adding a small fraction of the nanoparticles to the polymer matrix develops considerable properties for several applications. Polymer nanocomposites have attracted great interest of scientific communities due to their encouraging properties and widened applications, such as conductive coatings, sensors, energy storage devices, microwave absorbers and other devices [29]. Mostly, polymer composites with excellent dielectric characteristics are highly desirable for designing supercapacitors and electronic devices [30]. Generally, the properties of the polymers are modified by adding nanofillers into the polymer matrix. The properties of polymer nanocomposites (PNCs) depend primarily on the particle size, shape, concentration, and the method by which the nanofillers are dispersed. Further, much attention has been given to the PNCs due to their unique properties which can be attained by employing these materials. Polymers can be selected as excellent host materials for the nanoparticles (NPs), which shows the outstanding properties[31] .

1.7 Polymer Used in the Study

1.7.1 Poly (methyl methacrylate) (PMMA)

Poly (methyl methacrylate) is one of the earliest and best-known polymers. It is an essential and exciting polymer because of its attractive physical and optical properties and broad application. It is a polymer with several interesting biological properties, as shown in Table (1.1). PMMA is a non-biodegradable polymer with good transparency, mechanical strength, less weight, and chemical resistance [35].Thermoplastic material with good tensile strength and hardness, high rigidity, transparency, colourlessness, resistance to weathering corrosion, and sound insulating properties. Poly (methyl methacrylate) has disadvantages, such as brittleness and low chemical resistance, which can be eliminated by chemical or physical modification. PMMA contains both hydrophobic (ethylene) and hydrophilic (carbonyl) groups in each unit. The additional polymerization of methyl methacrylate produces poly (methyl methacrylate). PMMA is the most commonly used polymer among the methacrylate family and has tremendous applications in automotive. A chemical structure of the repeating unit of PMMA polymer [35], as shown in Figure (1.2).

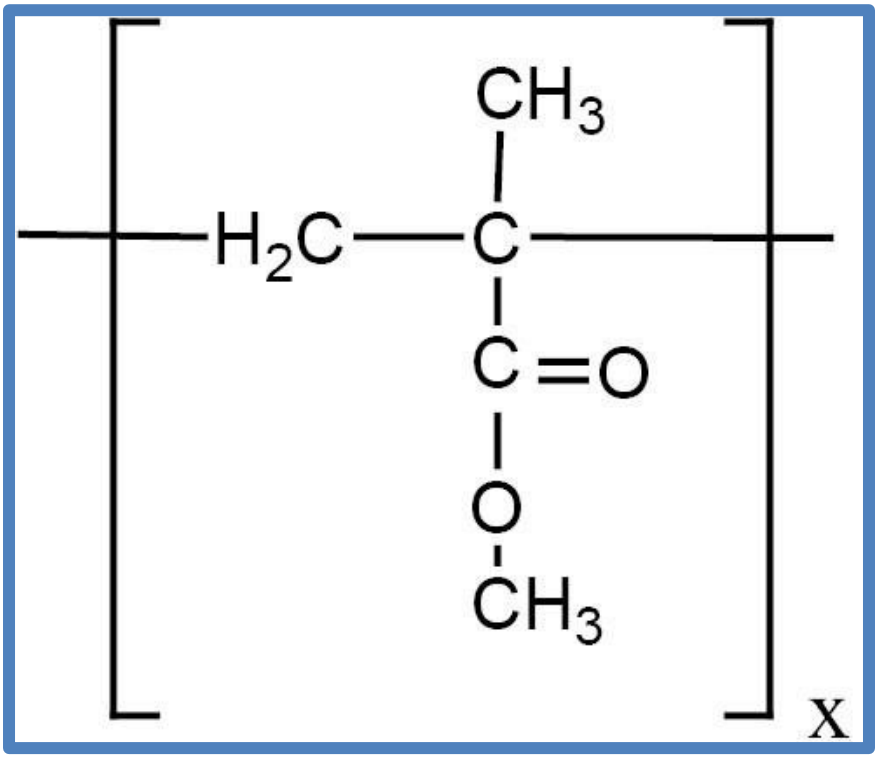

Figure (1.2) Chemical structure of PMMA [36].

Table (1.1) Physical and chemical properties of Poly (methyl methacrylate) [37].

Properties	PMMA
Chemical formula	$CH_2=C(CH_3)\ COOCH_3$
Tg	105 ^{o} C
Refractive index	1.49
Density	1.19 g/cm^3
Melting point	180 ^{o} C

1.7.2 Polycarbonate (PC)

Polycarbonate (PC) is a thermoplastic polymer with excellent temperature, impact, and transparency properties. In addition to its superior optical qualities, it possesses a high elastic modulus and mechanical strength. Medical applications, including optical lenses, CDs, DVDs, and electronic instruments, frequently employ PC. Polycarbonate, one of the most popular technical polymers, is amorphous, transparent, entirely recyclable, and derived from natural resources. As a result, it has received a lot of attention [38]. In addition, it is capable of withstanding a variety of harsh and extreme environmental conditions.Additionally, it aids in reducing carbon impact [39].

The global polycarbonate market is expected to be worth more than 4,100 kilotons in 2021, with an average annual rate of more than 2% in revenue during the forecast timeframe (2022-2027). The global polycarbonate market is divided into end-user applications: automotive and transportation, electrical and electronics, construction, medical, and others. Most use cases in the electronics industry are for optical media storage discs. Compared to conventional recycled sources, waste optical discs manufactured with top-grade high-quality PC can be considered a low-cost source of superior-quality PC. A large volume of CDs comes from industrial waste (about 1% of total production) and unsold optical media that must be destroyed. Polycarbonate is chemically resistant enough for single use with dilute or weak acids, bases, oxidizing agents, aqueous solutions, and detergents/surfactants [40].The Characteristics of the Polycarbonate nanoparticles as shown in Table (1.2).

Table (1.2) Characteristics of the Polycarbonate nanoparticles [41]**.**

Appearance	PC
PH	(9-11)
Bulk density	1200 kg/m^3
Specific gravity	1.20
Thermal conductivity, W/(m.K)	0.19
Thermal Expansion (K^{-1})	6.75×10^{-6}
Melting point (unplasticized)	110
Tensile Elastic Modulus (GPa)	2.38
Hardness (Rockwell)	M70
Refractive Index	1.586
Water Absorption, %	0.15
Stability to sunlight	Excellent

1.8 Nanomaterial Used in the Study

1.8.1. Antimony Trioxide (Sb_2O_3)

Antimony trioxide (Sb_2O_3) has wide applications as an effective catalyst, retardant, conductive materials, functional filler, and optical materials. In addition, Sb_2O_3 is very useful as a conductive material , with high-efficiency flame-retardant synergist in plastics, paints, adhesives, and textile back coating. Antimony trioxide (Sb_2O_3) is a semiconducting material and an an excellent catalyst for the production of PET plastic used in the packaging of mineral water and soft drinks [42]. Its safe use in the production of PET the world health organisation has confirmed bottles and the european food safety authority. Sb_2O_3 greatly increases flame retardant effectiveness when used as a synergist in combination

with halogenated flame retardants in plastics, paints, adhesives, sealants, rubber, and textile back coatings.Sb_2O_3 nanoparticles have been successfully synthesized under a controlled atmosphere using. ray radiation–oxidation route method or chemical method and recently via hybrid induction and laser heating (HILH).In addition Sb_2O_3, nanorods have been synthesized using microemulsion, while Sb_2O_3 fibrils and tubules have been prepared using vapour–solid mechanism. Antimony Trioxide (Sb_2O_3) has a crystal structure typically described as rhombohedral, but it can also be viewed as a distorted cubic structure. The space group of AntimonyTrioxide is R-3c. The unit cell of antimony trioxide is rhombohedral, with lattice parameters a = b = c and angles alpha = beta = gamma ≠ 90 degrees. The rhombohedral angle is approximately 60.3 degrees. The conventional unit cell of antimony trioxide contains six formula units or 18 atoms.The rhombohedral unit cell of AntimonyTrioxide has six antimony atoms and nine oxygen atoms [43].The antimony atoms are located at the corners of the rhombohedron, while the oxygen atoms are located at the center of each face of the rhombohedron. Each antimony atom is surrounded by six oxygen atoms, forming an octahedral coordination geometry as show in figure (1.3).

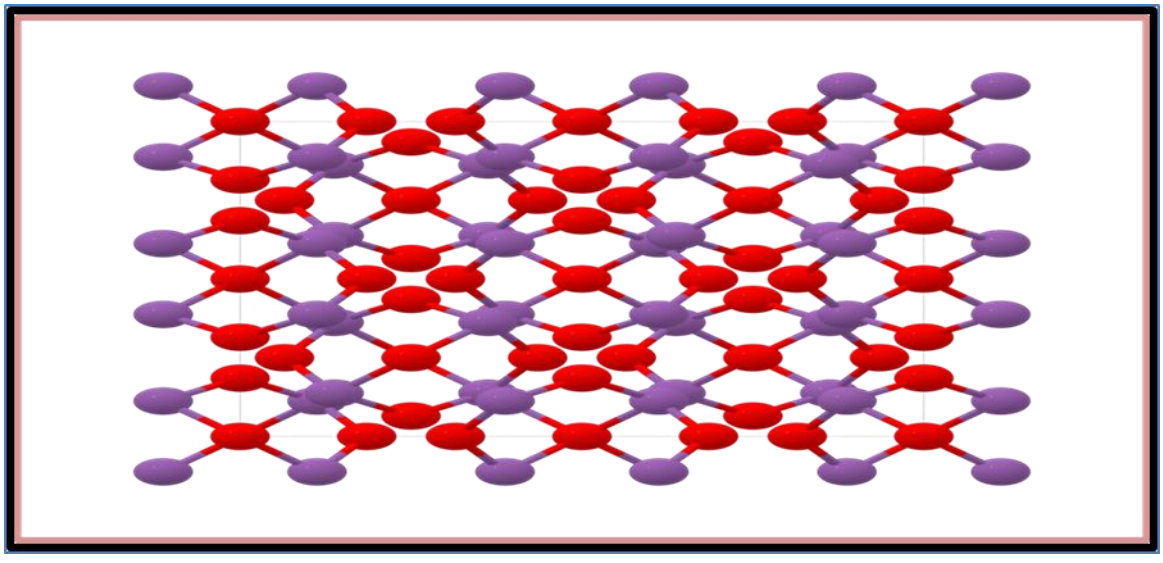

Figure (1.3) The lattice structure of Sb_2O_3 [44]**.**

Table (1.3) Characteristics of the Antimony Trioxide nanoparticles [45].

Properties	**Sb_2O_3**
Molar mass	291.518 g/mol
Appearance	white solid
Density	5.2 g/cm^3, α-form
	5.67 g/cm^3, β-form
Melting point	656 °C (1,213 °F; 929 K)
Solubility in water	370 ± 37 µg/L between 20.8°C and 22.9°C
Solubility	soluble in acid
Magnetic susceptibility (χ)	-69.4·10^{-6} cm^3/mol
Refractive index (nD)	2.087, α-form
	2.35, β-form
Energy gap	1.2 ev

1.8.2 Indium Trioxide (In_2O_3)

Indium trioxide nanocrystals are individual n-type semiconductors that have drawn attention among other semiconductor photocatalysts because of their excellent electrical and physical properties. In addition to their high exciton binding energy, Indium Trioxide exhibits a direct and broadband gap (3.7 eV). In addition to their excellent stability and room temperature luminescence, they also have strong oxidizing power and good UV emission properties [46] . These characteristics make them highly appealing and promising materials for a variety of devices, including ultraviolet photo detectors, photovoltaic devices, and other electronic devices photocatalysts, laser diodes, sensors, and solar cells . Additionally, because In_2O_3 nano-objects are made of biocompatible, low-toxic materials, they may be employed in a

variety of biological applications .In addition to their great stability and room temperature luminescence, they also have strong oxidizing power and good UV emission properties [47] .These characteristics make them highly appealing and promising materials for various devices, including ultraviolet photodetectors, photovoltaic devices, other electronic devices, photocatalysts, laser diodes, sensors, and solar cells. The crystal structure of Indium Trioxide (In_2O_3) is cubic, specifically in the bixbyite structure. The unit cell of Indium Trioxide is cube-shaped, with eight indium atoms located at the corners and six oxygen atoms at the faces of the cube [48]. Each indium atom is surrounded by six oxygen atoms, forming an octahedral coordination geometry.The lattice parameter, or the length of one edge of the cube, is approximately 10.12 Angstroms. The space group of Indium Trioxide is Ia-3, and the symmetry operations within the unit cell include a three-fold rotation axis and inversion centers located at the center of each face of the cube [49],as shown in figure (1.4).

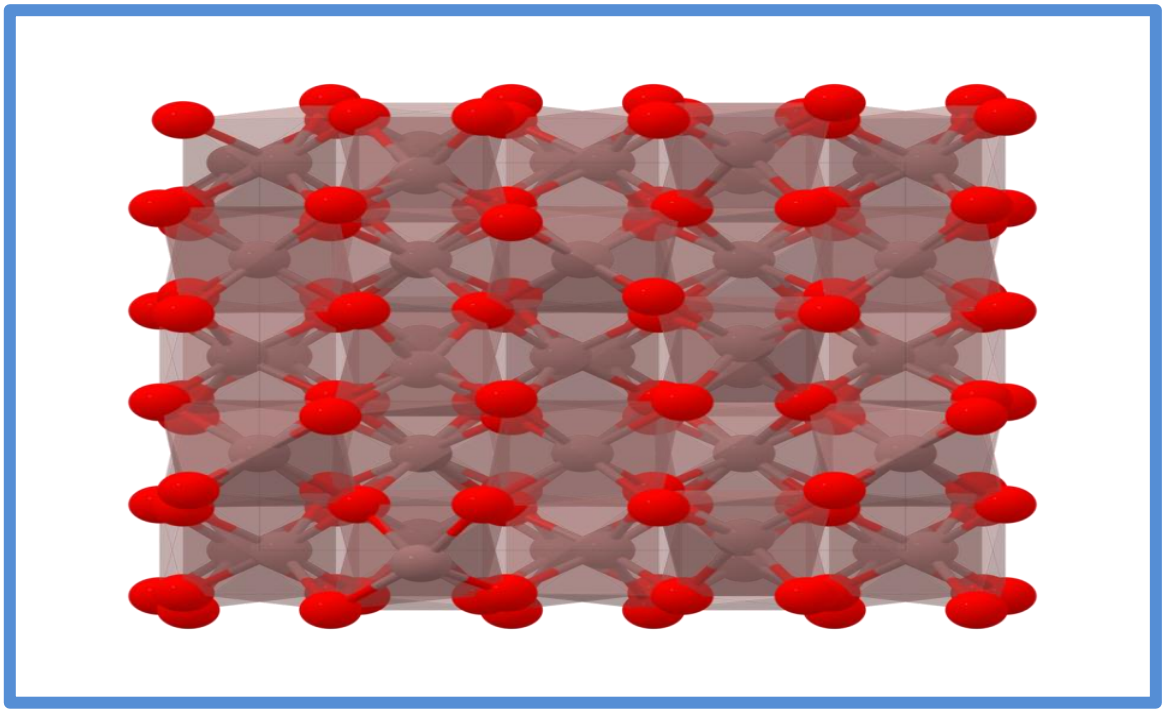

Figure (1.4) The lattice structure of In_2O_3 [50].

Table (1.4) Characteristics of the Indium Trioxide nanoparticles [51]**.**

properties	In_2O_3
Molar mass	277.64 g/mol
Appearance	Yellowish green odorless crystals
Density	7.179 g/cm^3
Melting point	1,910 C° (3,470 °F; 2,180 K)
Solubility in water	insoluble
Band gap	~3.7 eV
Magnetic susceptibility (χ)	−56.0·10−6 cm^3/mol

1.8.3 Graphene oxide GO

Graphene oxide (GO) is a promising and valuable material for graphene-based applications such as electronics, optics, chemistry, energy storage, and biology. GO was a simple and inexpensive step in reducing single and multilayer graphene and bulk structural features at the start of graphene history. However, further research revealed significant structural imperfections in graphene oxide-derived materials due to defects in initial graphite and non - completion of the decrease process. Graphene oxide (GO) was regarded as the result of chemical exfoliation and oxidizing of layered crystalline graphite (natural or artificial) [52].Amazingly, at definite conditions of oxidizing graphite, carbon atoms conserve the integrity 2D structure of layers with oxygen-containing functional groups attached to both sides of the carbon plane and the edges. However, recent results demonstrated that the same structure

could also be obtained using the alternative (bottom-up) method by hydrothermal treatment of glucose or even by chemical vapour deposition (CVD) technique. Therefore today, it is worth giving a more general definition based on its structure: single atom carbon layer with both surfaces modified by oxygen-containing functional groups.Like any 2D carbon, GO can have a single-layer or multilayer structure.Carbon layers in multilayer GO are separated by functional groups bonded to each layer of carbon atoms [53].

1.9 Literatures Review

D . Goyal *et al.*[54]**, in (2014),** the structural and optical properties of ZnO/PMMA nanocomposites thin films have been studied. ZnO nanoparticles were synthesized by solvothermal method and then annealed. ZnO/PMMA nanocomposites thin films have been prepared by solution casting method. The nanomaterials were characterized to find the composition and morphology using XRD, TEM, FTIR and UV-Visible spectroscopy techniques. XRD characterization of the ZnO powder showed the formation of wurtzite type ZnO crystals and the crystallinity of ZnO was more pronounced after annealing. FTIR study of these polymer-inorganic composites shows presence of hydroxyl groups, symmetrical bending vibration of C=O, C—H stretching and characteristic peak of ZnO. It is also observed that ZnO/PMMA polymer film shows strong absorption in ultra violet range. It is also observed that properties of nanocomposites films can be changed by using nanoparticles of different sizes. The TEM image of ZnO/PMMA nanocomposite reveals the presence and good dispersion of nanoparticles in polymer matrix.

X. Hou *et al.*[55]**, in (2015),** studied a new polyethylene glycol/graphene oxide composite material bonded on the surface of a stainless-steel wire. The polyethylene glycol/graphene oxide was characterized by Fourier transform infrared spectroscopy and elemental analysis, which verified that polyethylene glycol was successfully grafted onto the surface of graphene oxide. The

proposed method exhibited an excellent extraction capacity and high thermal stability. Furthermore, the as-prepared fibre was used to determine the model compounds in the water and soil samples and satisfactory results was obtained.

S.Agarwal *et al.* [56] **, in (2016)**, prepared the ZnO nanoparticles that are uniformly dispersed in a Polycarbonate/Polymethylmethacrylate (PC/PMMA) blend nanocomposites simple chemical method has been utilized. The size of the nanoparticles has been confirmed to be approximately 11 nm using Transmission Electron Microscopy (TEM). X-ray Diffraction (XRD) has been employed to verify the formation of the PC/PMMA blend nanocomposites. Optical constants, such as band gap, extinction coefficient, refractive index, and the real & imaginary parts of the dielectric constant, have been determined from the absorption spectra, which were obtained using a UV-Visible spectrophotometer. The results demonstrate that the band gap reduces as the ZnO weight percentage increases in the blend nanocomposites. Moreover, an increase in the refractive index has been observed with the increasing content of ZnO. These types of blend nanocomposites have practical applications in UV-shielding and waveguide technologies.

M.K.Mohammed *et al.*[57]**,in (2017),** studied the optical properties for of (PVA-PEG-Sb_2O_3). The results showed that the transmittance decreases with increasing of concentration of Sb_2O_3. The absorbance, absorption coefficient, extinction coefficient, refractive index, and parts of dielectric constant of (PVA-PEG-Sb_2O_3) composites increase with the increasing of Sb_2O_3 concentrations. The energy gap of (PVA-PEG-Sb_2O_3) composites decreases with the increase of the Sb_2O_3 concentrations.

L. S. Tang *et.al*, in (2017) ,studied Polyethylene glycol (PEG)/graphene oxide aerogel (GA) composite phase change materials (PCMs) that were

prepared using introducing PEG into GAs from graphene oxide (GO) with different oxidation degrees via vacuum impregnation. Structural analyses confirmed that the oxygenated functional groups increased, and the hydroxyl groups were transformed into carboxyl and epoxy groups with increasing oxidation levels. Morphology analysis showed that the breakage of the graphene sheet became more severe with the oxidation level increasing. When GAs prepared with GOs of higher oxidation levels were used, the composite PCMs showed excellent shape stability during phase change and thermal repeatability. Efficient photo-to-thermal energy conversion and storage were realized in the composite PCMs.

G. Santhosh, *et al.*[58], in(2017), studied producing nanocomposites of Polycarbonate (PC) with halloysite nanotubes (HNTs) as reinforcement using the solution intercalation method. They examined the impact of varying HNT content on the resulting films' structural and dielectric properties. The goal was to determine the influence of the nano-fillers on the electrical behaviour of the PC. The addition of HNTs resulted in a significant improvement in the film's electrical conductivity, particularly when the HNT content exceeded 4 wt%. Moreover, incorporating HNTs significantly increased the dielectric permittivity of the composite films, while also lowering dielectric loss. As a result, these nanocomposites could be suiTable for use in electrical devices, electrical packaging, and capacitors. The study also investigated the structural aspects of the nanocomposites using techniques such as X-ray diffraction, Fourier transform infrared spectroscopy, and scanning electron microscopy to evaluate the dispersion of nanofillers in the PC matrix.

F. J. Hamood *et al.*[59], in(2018) conducted a study on the AC electrical properties of a composite material containing PVA, PEG, and Sb_2O_3, across different frequencies. Their findings indicated that as frequency increases, both the dielectric constant (ε) and dielectric loss (δ) decrease. Conversely, the addition of AntimonyTrioxide (Sb_2O_3) to the composite material resulted in an

increase in both ε and δ. In terms of electrical conductivity (ζ), an increase in frequency resulted in an increase in ζ, while an increase in Sb_2O_3 content led to a decrease in ζ in the (PVA-PEG-Sb_2O_3) composites.

G. Evingür, *et al.*[60] **, in(2018),** studied the " Optical energy band gap of PAAm-GO composites'. UV-Vis Spectroscopy characterized the PAAm-Graphene oxide (GO) composites". The optical band gap of PAAm-GO composites has been monitored and tested as a function of GO material. The Tauc model and the 7Absorption Spectrum Fitting (ASF) technique, which shows the band tail width for composites, explained the operation of the gap in the optical band. It is crucial to note that the optical bandgap of the composite is substantially bigger for low GO (below 8µ l of GO) and high GO (above 8µ l of GO) material regions, providing a critical value at 8µ l of GO content, Because, as we know from the µ calculation, the strength of the composite is much greater for the low GO (below 8µl of GO) and high GO (above 8µl of GO) material regions of the composite, the decrease in the bandgap (Eg) for low GO material, 0-8µ l, can be explained as a result of an increase in the degree of disorder in the structure of the composite.

Y. Liu, *et al.* [61]**, in (2018)**, the authors investigated the production of self-assembled nanocomposites consisting of PVA/PAA/GO-COOH@AgNPs using electrospinning as an eco-friendly and efficient technique. The resulting nanofibers exhibited enhanced stability and acted as a good support for AgNP loading, effectively preventing agglomeration. The GO nanosheet contained highly negatively charged carboxyl groups, enabling targetless diffusion and dyes enrichment through electrostatic solid interactions with the adsorption sites on the GO surface.The PVA/PAA/GO-COOH@AgNPs nanocomposite membranes showed significant catalytic activity for the degradation of MB at room temperature, even after eight cycles. This study presents a novel method for designing and producing composite materials containing Ag nanoparticles for efficient catalytic applications in the treatment of wastewater.

Abdulhadi Kadhim *et al.*[47] **,in (2018),** studied 'Optical and Structural Properties of (In_2O_3:ZnO:Au) Nanocomposite Thin Films Prepared by Spray Pyrolysis Method'.The (In_2O_3:ZnO: Au) nanocomposite thin film was successfully synthesized by the spray pyrolysis method. X-ray pattern for samples indicates the formations of the crystalline structure of (In_2O_3:ZnO: Au) nanocomposite thin film is cubic spinal structure phase of In_2O_3 and Au, and Hexagonal Structure phase of ZnO. When the gold content increases in concentration the lattice parameter increases. The transmittance and the optical energy gap of (In_2O_3:ZnO:Au) nanocomposite thin film with different concentrations are decreased with increasing gold nanoparticle content. The absorption coefficient, extinction coefficient, refractive index, and real and imaginary dielectric constant of (In_2O_3:ZnO: Au) nanocomposite thin film with different concentrations increase with increasing gold nanoparticles content. The optical band gap reduces with the increase in gold concentration. The high extinction coefficient and the high magnitude of optical conductivity promote the presence of a very high samples photo response.

AM. Patki *et al.*[62]**,in (2019),** fabricated polycarbonate/h-BN composites were using the solution method followed by hot pressing at 230 °C and 45 MPa. The experimental density of the composites was found close to the theoretical density indicating pores-free samples. XRD did not show a change in the morphology of the PC. SEM revealed uniform dispersion and distribution of the h-BN particles in the matrix. FTIR and SEM indicated better interaction between the h-BN particles and the matrix. The dielectric constant of pure PC is 2.9 (at 1 MHz) which was increased marginally to about 3.9 for 44.4 vol% composites. Interestingly, the dispersion in the dielectric constant of the composites with increasing frequency was reduced significantly and the dissipation factor, of the filled composite was reduced to below 0.007.

O. Büşra *et al.* [63]**, in (2019)** studied 'Effect of Temperature and Graphene Oxide on the Swelling of PAAm-GO Composite Gels' The findings of this work

suggest that the fluorescence approach can be utilized to trace the kinetics of the PAAm-swelling GO composite in water at various temperatures and GO content. This technique was utilized to calculate the swelling time constants and cooperative diffusion coefficients, for composite gels made with PAAm and various GO contents. Cooperative diffusion coefficients were calculated using Li Tanaka's model supplemented with Stern Volmer's Equations. It is important to note that the GO component may work as a multifunctional cross-linker, forming more PAAm- GO composite junctions and increasing crosslink density, lowering swelling power.

Ü. Alveret *et al.* [64] **, in (2019)**, studied incorporated α-Fe2O3-ZnO mixed particles into the poly methyl methacrylate (PMMA) matrix using a solvent casting process. To create a powder mixture, they utilized the mechanical milling process. They synthesized α-Fe2O3 through a precipitation method and mixed it with ZnO nanoparticles in equal amounts. The resulting mixture was milled for one hour using a planetary-type ball milling machine. The powders were examined for morphological and structural properties using scanning electron microscopy (SEM) and X-ray diffraction (XRD). In addition, the optical and dielectric properties of composite materials were analyzed using UV-Vis spectrophotometry and a vector network analyzer (VNA) for different levels of reinforcement .The researchers observed that the optical transmittance decreased as the reinforcement amount increased. They also examined the dielectric properties of produced pellet composites with a thickness of 4 mm between 70 and 110 GHz. The results showed that the real and complex permittivity and dielectric loss values of PMMA/α-Fe_2O_3 were higher than those of neat PMMA, PMMA/ZnO, and PMMA/α-Fe2O3-ZnO.

N. Guo *et al.*[65] **,in (2020) ,**studied "Preparation of Fe_2O_3 nanoparticles doped with In_2O_3 and photocatalytic degradation property for rhodamine B"The objective of this study was to create a photocatalyst utilizing Fe_2O_3 nanoparticles with In_2O_3 doping, which could be utilized to decompose

rhodamine B. The efficacy of the photocatalyst in breaking down rhodamine B was analyzed under varying conditions, such as the amount of In_2O_3 doping, dosage of the photocatalyst, H_2O_2 concentration, and pH level. The highest degradation rate of 94% was achieved under optimal conditions. Furthermore, the mechanism by which rhodamine B was degraded was explored by analyzing the intermediate products obtained from HPLC and LC-MS.These results illustrated that Fe_2O_3 nanoparticles doped with In_2O_3 had great potential as a photocatalyst to remove rhodamine B in the environment and offered ways for photocatalytic degradation of organic toxicants.

K. M. Abu Hurayra *et al.*[26] **, in (2021)**, investigated the GO-based PVA nanocomposites: tailoring of optical and structural properties of PVA with a low percentage of GO nanofillers. They found that The incorporation of GO reduced the optical band gap of the nanocomposite both for the direct and indirect transition.

A . Omar *et al.*[66] **, in (2022)** , studied 'Enhancing the Optical Properties of Chitosan, Carboxymethyl Cellulose, Sodium Alginate Modified with Nano Metal Oxide and Graphene Oxide'. The solution casting method was utilized to synthesize nanocomposite films of chitosan (Cs)/CuO, Cs /graphene oxide (GO), carboxymethyl cellulose (CMC)/TiO2, CMC/GO, sodium alginate (Na Alg)/TiO2, and Na-Alg/GO owing to their various applications. The influence of CuO, TiO2 and GO concentration on the optical properties of Cs, CMC and Na-Alg films was studied by UV-Vis Spectroscopy. The absorbance of Cs, CMC and Na-Alg increased with increasing the filler content, thus reflecting the dependence of Cs, CMC, and Na-Alg properties on the nanofiller content, and confirming the interactions between individual polymers and CuO, TiO_2, and GO nanoparticles. The obtained absorbance values were then used to calculate the absorption coefficient and, hence, the optical band gap values. The characteristic absorption bands of CuO and TiO_2 underwent a redshift by

increasing the filler content. The results showed that the optical band gap of Cs, CMC, and Na-Alg decreased with filler content.

G Ramalingam *et al.*[67], **in (2022)** ,stuided the review of graphene-based semiconductors for photocatalytic degradation of pollutants in wastewater. An extensive overview and detailed investigations on the photocatalytic activity of graphene-based nanocomposites in the field of wastewater treatment have been carried out and are presented. it is found that the incorporation of graphene in transition metal oxides, metal ions, polymer, and mxene can greatly boost the photocatalytic efficiency against the elimination of organic azo dyes in wastewater by increasing the adsorption capacity of organi pollutants.

1.10 The Aims of The Study

1. Preparation new types of (PMMA-PC/In_2O_3-GO) and (PMMA-PC/Sb_2O_3-GO) nanocomposites.
2. Studying the structural, optical and A.C electrical properties of (PMMA-PC/In_2O_3-GO) and (PMMA-PC/Sb_2O_3-GO)nanocomposites.
3. Studying the applications of the (PMMA-PC/In_2O_3-GO) and (PMMA-PC/Sb_2O_3-GO) nanocomposites as photocatalytic and antibacterial activity.

2.1 Introduction

This chapter contains a general explanation of the theoretical portion of this study, as well as relationships, physical principles, scientific clarifications, and laws used to interpret the study's findings.

2.2 Optical Properties

The study of polymer optical properties expands our understanding of the type of polymer internal structure, the nature of the bonds, and the potential scope of polymer application. Knowing a polymer's absorption and transmittance spectrums aids in identifying many optical properties over a wide range of wavelengths [67]. Conducting an examination of the ultraviolet spectrum range enables us to know the type of bonds, orbital, and energy beams. The visible spectrum study provides sufficient information about a matter's behavior for optical applications [68].

2.2.1 Absorbance (A)

Absorbance can be defined as the ratio between absorbed light intensity (I_A) by material and the incident intensity of light (I_o) [70] :

$$A= I_A/I_o \qquad (2\text{-}1)$$

2.2.2 Transmittance (T)

Transmittance is the transmission mode's equivalent to reflectance. That is a transmittance is a dimensionless quantity described by the ratio of the radian flux I_t transmitted to the incident radiant flux I_o [71]:

$$T = I_t / I_o \qquad (2\text{-}2)$$

2.2.3 Fundamental Absorption Edge

The fundamental absorption edge is the rapid increase in absorptance when the absorbed energy radiation is almost equal to the band energy gap; thus, the fundamental absorption edge represents the less energy difference between the up point in the valance band and the bottom point in the conduction band .

There are three types of absorption regions[72].

A. High Absorption Region: The nature of electron transport in this zone is direct.The absorption coefficient does have a magnitude greater than or equal to $10^4 cm^{-1}$

B. The xponential Region: represents the transition from extended levels in the valence band to concentrated levels in the conduction band. Additionally, from localize levels in the top conductive band to extended levels in the bottom conduction band. The absorption coefficient has a magnitude of $(1<\alpha<10^4)$ cm^{-1}.

C. Low absorption region :the absorption coefficient α in this region is very low, around ($1cm^{-1}$). As shown in Figure (2.1), the transition occurs in this region as a result of state density inside space motion caused by structural faults (C).

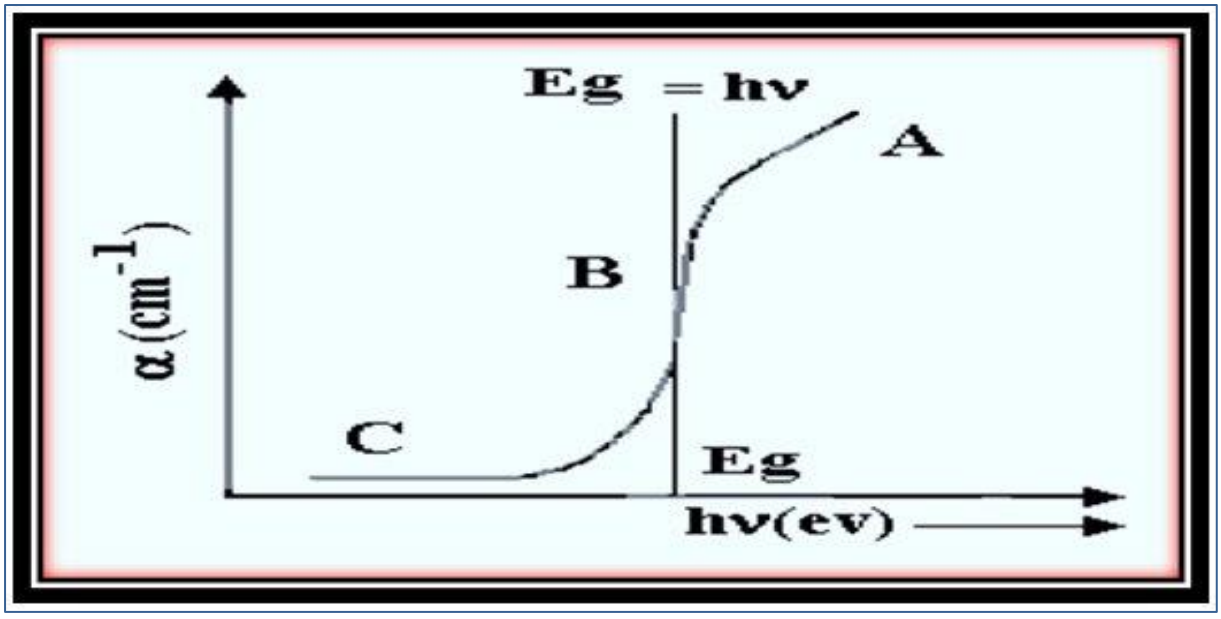

Figure(2.1) Areas of absorption edge. A- High absorption region. B-Exponential region C- Low absorption region [73]**.**

2.2.4 Electronic Transitions

There are two kinds of electronic transitions.

2.2.4.1 Direct transitions

When the conduction band and valance band bottoms out at the same point in space ($\Delta k = 0$). The absorption will appear at ($h\upsilon = Eg$) in this case. This type occurs when there is no discernible change in momentum. There are two types of direct transitions: those that occur between the top and bottom points of the valance and conduction bands in sequence, known as allowed direct transitions, and those that occur between neighboring points for the top and bottom points, known as forbidden direct transitions[74]. As illustrated in Figure (2.2).

2.2.4.2 Indirect transitions

In these transitions, the bottom of (C.B.) is not above the top of (V.B.). The electron distances from (V.B.) to (C.B.) are not perpendicular, where the value of the wave vector (k) of the electron before and after the transition is not equal ($\Delta k \neq 0$). For the preservation of energy and momentum law, this transition type occurs with the support of a particle known as a "Phonon." There are two types of indirect transitions when the transformation is between the peak of the valance band(V.B.) and the lesser point of the conduction band(C.D.), which is located in various zones of a space (k) so that (allowed indirect transition) as shown in figure (2.2), while when transitions occur between near points in the top of (V.B.) and near points in the bottom of (C.B.) these called (Forbidden indirect transitions). as shown in figure (2.2). The quantum mechanical transition probability from (V.B) to (C.B) is used to determine the absorption coefficient. The density of occupancy states at (V.B) from which electrons are excited and the density of left empty states in the (C.B). Thus (α) is dependent on the joint density of states at (V.B) and (C.B), and we must integrate this joint density of states appropriately[75]. Near the

band edges, the density of states can be approximated by a parabolic band, and the absorption coefficient(α) is obtained as a function of photon energy as :

The optical energy gap for direct transitions determind by [74] :

$$\alpha h\upsilon = B\left(h\,\upsilon - E_g\right)^m \qquad \text{(2-3a)}$$

Where: E_g energy gap between direct transition.

B: Constant depended on the type of material.

m: exponential constant, its value depended on type of transition.

m =1/2 for the allowed direct transition.

m =3/2 for the forbidden direct transition

For indirect transition equation(2-3a) become

$$\alpha h\upsilon = B\left(h\,\upsilon - E_g \pm E_{Ph}\right)^{\mathrm{m}} \qquad \text{(2-3b)}$$

Where E_{ph} energy of the photon

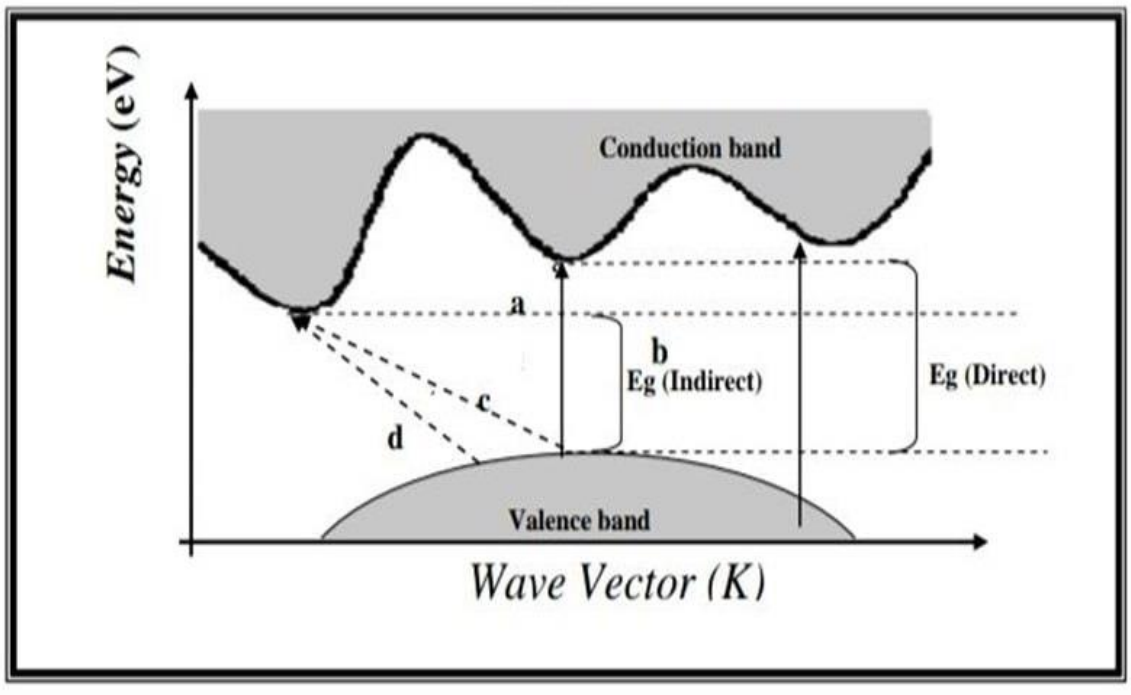

Figure (2.2) Direct and indirect transitions caused by band filling [76].

2.2.5 Optical Constants

2.2.5.1 Absorption Coefficient (α)

The absorption coefficient is a ratio decrement in incident ray energy flux relative to the distance unit in the direction of incident wave diffusion. The absorption coefficient (α) is affected by incident photon energy (hυ) and semiconductor characteristics (n or p). The following equation gives photon energy [77] :

$$E = h\upsilon \qquad (2\text{-}4)$$

When the incident energy of the photon is less than the forbidden gap in energy, the photon is transmitted, and transmittance is defined as follows [78]:

$$T = (1-R)^2 . \exp(-\alpha d) \qquad (2\text{-}5)$$

If the intensity of the incident ray (I_o) incident on a material of thickness (d) and the intensity of the transmittance ray (I_T) are equal, the integration procedure will yield the following results [79] :

$$dI = -\alpha I\, dx \qquad (2\text{-}6)$$

If intensity of incident ray (I_o) which incident on a material of thickness (x), and the intensity of the transmittance ray (I_T), then the integration procedure will obtain [80]:

$$\int_{I_o}^{I_T} \frac{dI}{I} = \int_{o}^{x} -\alpha dx \qquad (2\text{-}7)$$

$$T = \exp(-\alpha x) \qquad (2\text{-}8)$$

$$\frac{1}{T} = \exp(\alpha x)$$

$$2.303 \log(1/T) = \alpha x$$

$$A = \log (1 / T)$$

$$2.303\ A = \alpha x$$

$$\alpha = (2.303\ A) / x \quad (2\text{-}9)$$

2.2.5.2 The Refractive Index and Extinction Coefficient

Refractive index of the material is the ratio of the velocity of light in a vacuum to the velocity of the light in the sample [79] :

$$n = c/v \quad (2\text{-}10)$$

Where c: is the velocity of the light in vacuum and v: is the velocity of the light in the sample [80] :

$$n^* = n - ik \quad (2\text{-}11)$$

n* : is the complex refractive index, n : is a real part of the refractive index and k : is an imaginary part of the refractive index (extinction coefficient).

The relation between absorption coefficient and the extinction coefficient (k) is [81]:

$$k = \frac{\alpha \lambda}{4\pi} \quad (2\text{-}12)$$

λ: wavelength of photon.

The real part of the refractive index (n) can be determined by [82]:

$$n = \frac{1+\sqrt{R}}{1-\sqrt{R}} \quad (2\text{-}13)$$

Where R is the reflectance to estimate the nature of absorption.

2.2.5.4 Optical Dielectric Constant

The optical dielectric constant represents the ability of a matter for polarization. The matter can respond to different frequencies in a complex manner, at optical frequencies represented by light waves the electronic polarity is dominating above other remaining types of polarization. The real and imaginary dielectric constant can be calculated by the following equation [83] :

$$\varepsilon=\varepsilon_1 -i\varepsilon_2 \quad (2\text{-}14)$$

Where (ε) is the complex dielectric constant, (ε_1, ε_2) are the real and imaginary parts of the dielectric constant, respectively.The dielectric constant can be calculated by calculating the refractive index. The relation between the complex dielectric constant and the complex refractive index (n*) is expressed in the following equation [84]:

$$\varepsilon=n^{*2} \quad (2\text{-}15)$$

From the equations (2-11),(2-14) and (2-15), it can be concluded that

$$(n-ik)^2 =\varepsilon_1-i\varepsilon_2 \quad (2\text{-}16)$$

From the equation (2-14), the real and imaginary complex dielectric constant can be expressed by the following equation :

$$\varepsilon_1=n^2-k^2 \quad (2\text{-}17)$$

$$\varepsilon_2=2nk \quad (2\text{-}18)$$

2.2.5.5 4. Optical Conductivity (σ_{opt})

The optical conductivity (σ_{opt}) depends directly on the refractive index (*n*) and extinction coefficient (k) by the following relation [83]:

$$\sigma_{opt} = 2nk\omega\varepsilon_o \quad (2\text{-}19)$$

Where ω is the angular frequency, ε_o is the permittivity in the free space.

By substituting (2-12) in (2-18) with simplified, the optical conductivity can be expressed by the following equation [85]:

$$\sigma_{opt} = \frac{\alpha\, n\, c}{4\pi} \quad (2\text{-}20)$$

2.3 Electrical Dielectric Properties

When the electron distributions around constituent atoms or molecules are polarized by an external electric field, insulating materials can be used to save electrical energy in the form of charge separation. A material's complex permittivity is given by [86]:

$$\varepsilon^{*} = \varepsilon_a - j\,\varepsilon_b \qquad (2\text{-}21)$$

Where ε_a and ε_b are the real and imaginary parts of the complex permittivity and $j = \sqrt{-1}$

The real part of the permittivity can be expressed by [87] :

$$\varepsilon_a = \varepsilon_0 \varepsilon^{-} \qquad (2\text{-}22)$$

The magnitudes of ε_a and ε_b depend on the angular frequency (ω) of the applied electric field. The magnitude of ε_a (or the dielectric constant) refers to the material's ability to store energy from the applied electric field The capacitance of a capacitor consists of two parallel plates given by relationship [88] :

$$C_p = \frac{\varepsilon' \varepsilon_\circ A}{t} \qquad (2\text{-}23)$$

Where t is the thickness of the sample, $\varepsilon_\circ$ is a vacuum permittivity and έ is dielectric constant. The dielectric constant is defined as the ratio between the capacitance of the capacitor containing an insulator material between its conducting plates to the capacity of the same size with a vacuum between the plates [89]. The dielectric constant is given by[90]:

$$\varepsilon' = \frac{C_p}{C_\circ} \qquad (2\text{-}24)$$

Where C_p is parallel capacitance and C_o is a vacuum capacitor. Due to the different polarization of matter under the influence of an electric field, some of the applied electric field energy is dissipated by charge migration (i.e. conduction) or converted into heat energy (for example, molecular vibration) [91]. Ceramic capacitors based on highly polarizable inorganic materials have been used to meet the need for pulse power applications. Dielectric loss (ε'') can be expressed by [92]:

$$\varepsilon'' = \varepsilon D \quad (2\text{-}25)$$

Where: D is the Displacement factor. The dispersion factor measures the electrical energy lost in the sample from the applied electric field, which turns into thermal energy in the sample. The dissipated power in the dielectric is represented by the presence of alternating potential as a function of alternating conductivity is given by [89]:

$$\sigma_{A.C} = \omega \varepsilon'' \varepsilon_0 \quad (2\text{-}26)$$

2.4 Applications of Nanocomposites

2.4.1 Photocatalysis

The catalysis process depends on a substance that increases the rate of transformation of the reactants without affecting this substance or depleting it. This substance is known as the catalyst. It increases the rate of a reaction by decreasing its activation energy. Thus, the photocatalytic process is a reaction in which light is used as an activator for the substance that will increase the rate of the chemical reaction without having a role in the reaction itself [93]. To clarify the idea more, we take an example from nature. For example, chlorophyll in plants is a natural photocatalyst. The difference between chlorophyll and the industrial catalyst is that the chlorophyll absorbs sunlight to convert water and carbon dioxide into oxygen and glucose, but the industrial catalyst gives a very strong oxidizing compound that breaks the bonds of toxic organic substances

and bacteria when exposed to sunlight or normal light and turns them into carbon dioxide and water[94], as shown in the figure(2.3).

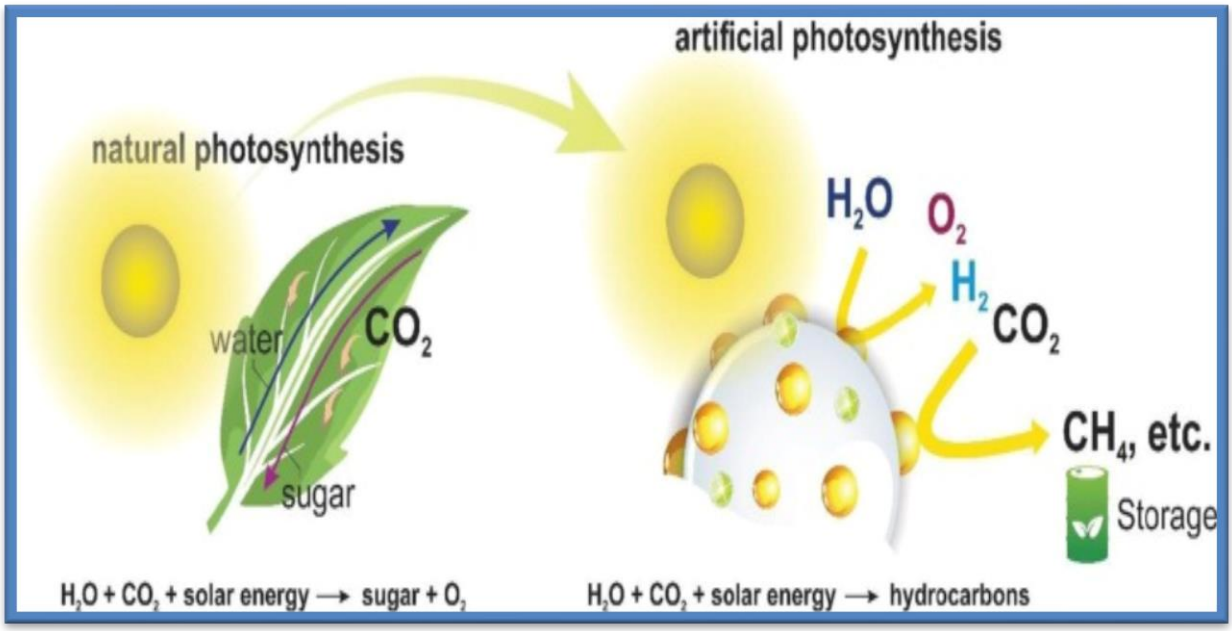

Figure (2.3) Photocatalytic process compared to Photosynthesis of plants [95]**.**

This principle can also be used in water treatment and purification, as well as the decomposition of toxic nitrogen oxides in the air, air purification in homes and workplaces and other useful applications. Semiconductors were chosen as the photocatalyst because semiconductor materials possess a small energy gap between the valence band and the conduction band.In order for the photocatalysis process to take place, the semiconductor material absorbs energy from sunlight, for example, or from a source of ultraviolet radiation, at least equal to the energy gap, so electrons move from the valence band to the conduction band, so there are an electron in the conduction band and a positive gap in the valence band. The positive gap is a strong oxidizer that can oxidize molecules [96].The adding of polymeric materials to nanomaterials causes dispersion and prevents sedimentation, resulting in a reduction in electron-hole recombination and a raise in the photocatalytic efficiency of the nanoparticles. When the nanocomposite absorbs ultraviolet radiation from the sun's rays or any light source operating in the ultraviolet range, the energy of the ultraviolet

radiation is sufficient to liberate a negative electron and a positive hole.The valence band electron in the semiconductor becomes excited when it absorbs ultraviolet radiation, and the e-electron moves to the conduction band, leaving behind a positive hole in the h^+ valence band. In this case, the nanocomposite becomes excited. The h^+ positive hole in a semiconductor, converts a water molecule into hydrogen and hydroxyl. The electron interacts with the oxygen molecule and gives a strong oxidizing anion. This process continues as long as there is light available. The organic molecule will attack these radicals, which will then be oxidized to form H_2O, CO_2, and HCl. Photodegradation processes include the following [97] :

1. Excitons are formed as a result of photon absorption by photocatalyst nanocomposites.

nanocomposites + hν $\longrightarrow$ $h^+ + e^-$ (2-27)

In the conduction band, electrons (e^-) are generated, while holes (h^+) are generated in the valence band.

Superoxide anion formation ($O_2^{\bullet}$)

2. Formation of superoxide anion ($O_2^{\bullet -}$) (2-28)

$O_2 + e^- \longrightarrow O_2^{\bullet -}$

3. Formation of hydroxyl radicals ($OH^{\bullet}$)

$H_2O + h^+ \longrightarrow H^+ + OH^{\bullet}$ (2-29)

4. Neutralization of superoxide anion by protons and formation of Hyper oxide radical ($HO_2^{\bullet}$).

$O_2^{\bullet -} + H^+ \longrightarrow HO_2^{\bullet}$ (2-30)

5. Formation of hydrogen peroxide (H_2O_2) and dismutation of oxygen.

$2HO^{\bullet}_2 \longrightarrow H_2O_2 + O_2$ (2-31)

$H_2O_2 + e^- \longrightarrow OH^- + OH^{\bullet}$ (2-32)

6. Formation of degradation products.

R (Organic pollutant) + H_2O_2 + $OH^{\bullet}$ + $O_2^{\bullet -}$ ⟶ CO_2 + H_2O (2-33)

The mechanism of photocatalysis is shown in figure(2.4).

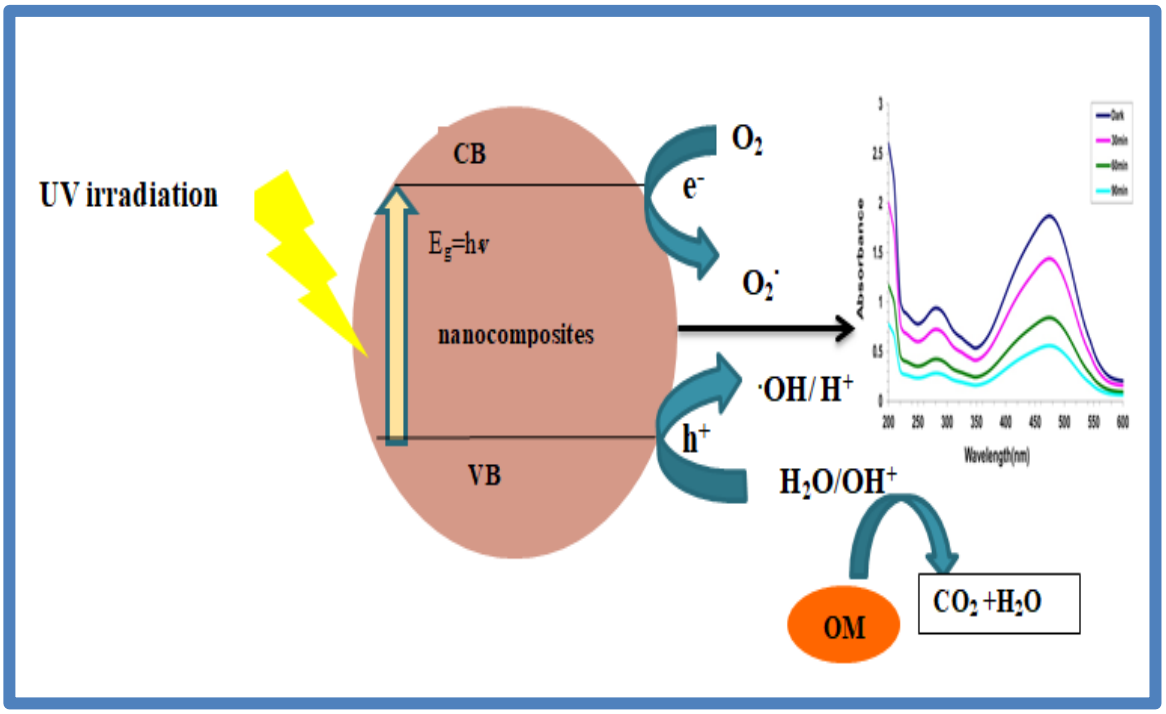

Figure(2.4) Schematic diagram of photodegradation mechanism [98].

The photocatalytic efficiency of the nanocomposite catalyst was tested by measuring the photocatalyzed discolouration rate of MO in an aqueous solution. So the experiment for photodegradation of MO solution under the near-UV light source was first set up. Then, 10 ml of the suspension was degraded by MO solutions at different times in order (0min,30min, 60min,90min), and it was subjected to centrifugation at 3500 rpm for 20 min to remove powder/nanoparticles. Finally, the concentration of residual MO (i.e., supernatant liquid) and their absorbance were measured by the UV visible Spectrometer at 465 nm. The degradation dye percentage (DP) can be calculated by the following equation [99]:

$$D_P = (X_0 - X_1) / X_0 \times 100 \quad (2\text{-}34)$$

X_0 and X_1 are absorption before and after UV irradiation, respectively. The reaction kinetics of MO dye decay using (PMMA-PC/In_2O_3-GO) and (PMMA-PC/Sb_2O_3GO) photocatalysts were investigated using the Langmuir-Hinshelwood designed kinetics model [97]:

$$Ln (A/A_0) = k t \quad (2\text{-}35)$$

Where A_0 and A are MO dye's starting and temporal concentrations.

2.4.2 Antibacterial Effect Systems

Antimicrobial drug resistance has increased in recent years due to antibiotic overuse. Because researchers design and improve nanocomposites as a potential antimicrobial method, this microorganism resistance is less likely to spread to nanomaterials. Metal oxide-based materials have attracted the attention of researchers looking to develop new hybrid systems with enhanced antimicrobial properties. The thermally or chemically modified metal oxide can also be electrically functionalized, allowing its physicochemical properties to be beneficial or create different composites. Furthermore, research on mixed antimicrobial agents like metal, metal oxide, and base materials like polymers is ongoing [100]. Antibacterial nanocomposites comprise a polymer matrix and an active antibacterial additive with antibacterial properties even at low concentrations.Nanoparticles of indium trioxide and antimony trioxide, for example. In_2O_3 nanoparticles are gaining popularity due to various properties such as semiconductivity,high adsorption capacity, stability, catalytic performance, and antibacterial properties. As a result, it is used as a food additive, and Sb_2O_3 nanoparticles are widely used as an active ingredient in dermatological applications such as ointments, lotions, and creams. It has been reported that graphene nanocomposites possess antibacterial, antiviral, and antifungal properties. The antibacterial activity is believed to arise from various mechanisms by which graphene nanocomposites can affect cells, including

inducing oxidative stress, disrupting cell membranes through sharp edges, and significantly altering the mechanical strength and surface roughness of the core structure. In_2O_3, Sb_2O_3 and GO nanoparticles are thought to have two antimicrobial mechanisms:

1. Indium Trioxide, antimony trioxide, and graphene oxide nanoparticles generate hydrogen peroxide, which, when penetrating the cell membrane, leads to injury and inhibits cell growth [101].
2. The main factor for antibacterial activity is a convergence between In_2O_3, Sb_2O_3 and GO nanoparticles and bacterial cells. Therefore, there are several necessities of antibacterial filler are the following:

The following are the basic requirements for antibacterial filler:

1. It is nontoxic to humans, animals, and the environment.
2. The application is simple to use.
3. The long-term effectiveness and storage stability.

The antibacterial activity of (PMMA-PC/In_2O_3-GO) and (PMMA-PC/Sb_2O_3-GO) nanocomposites can be summarized as the following steps of the prepared samples:

1. Both (PMMA-PC/In_2O_3-GO) and (PMMA-PC/Sb_2O_3-GO)nanocomposites can generate (e^-h) pairs.
2. UV-visible absorption spectra of (PMMA-PC/In_2O_3-GO) and (PMMA PC/Sb_2O_3-GO)nanocomposites revealed an optical band gap value, indicating the presence of intermediate energy levels between the valence and conduction bands.
3. Another mechanism for killing bacteria is the release of indium and antimony ions in the bacterial medium[102].

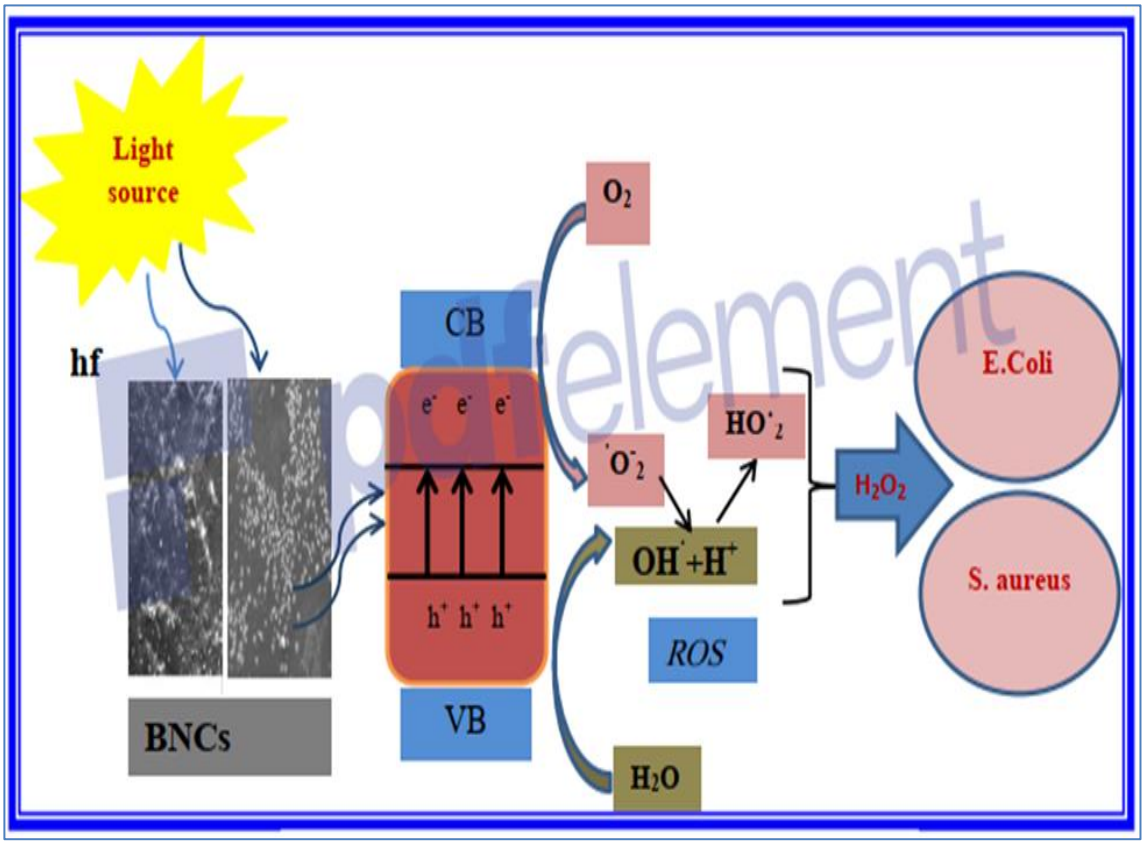

Figure (2.5) Steps of inhibition bacterial [103]**.**

3.1 Introduction

This chapter contains sample preparation for (PMMA-PC/In_2O_3-GO) and (PMMA-PC/Sb_2O_3-GO) nanocomposites, as well as sample testing and measurement steps such as: optical Microscopic, Scanning Electron Microscope (SEM), Fourier transformation infrared radiation (FTIR), A.C electrical measurements, optical measurements, photocatalysis and antibacterial activity.

3.2 The Materials Used in This Work

3.2.1 Polymers

In this work, two different types of polymers are used:

1. **Polymethylmethacrylate (PMMA):** The polymer was used in granular form and was procured with high purity (99.99%) from Scientific Polymer Products Inc (Origin. Canada) (5000 M.W).
2. **Polycarbonate(PC):** the polymer is used as powder . Manufacture: Teijin Human Chemistry - Japan company.

3.2.2 Additive Nanomaterials

This study employs three types of nanoparticles:

1. **Indium trioxide nanoparticles (In_2O_3):** It was obtained as a powder from US Research Nanomaterials, Inc., USA, with a grain size of 20-30 nm with high purity (99.99%)**.**
2. **Antimony trioxide nanoparticles (Sb_2O_3):** It was obtained as powder from US Research Nanomaterials, Inc., USA company with grain size 20-30 nm.
3. **Graphene oxide nanoparticles (GO**): It was obtained as a powder from US Research Nanomaterials, with a grain size of 15-20 nm with high purity (99.99%).

3.3 Preparation of (PMMA-PC/In_2O_3GO) and (PMMA-PC/Sb_2O_3-GO) Nanocomposite.

The pure (PMMA-PC) blend and nanocomposites of (PMMA-PC/In_2O_3-GO) and (PMMA-PC/Sb_2O_3-GO) nanocomposite, prepared by dissolving (0.8g) of PMMA and (0.2g) of PC in 30 ml of chloroform with a concentration is 80 wt.%PMMA and 20 wt.% PC by using a magnetic stirrer to mix the polymers for (20-25)minutes to obtain a more homogeneous solution at room temperature.The In_2O_3, Sb_2O_3 and GO nanoparticles were added to the polymer blends with concentrations (1.4, 2.8, 4.2, and 5.6) wt.%. as shown in Tables (3.1) and (3.2). The nanocomposite samples were prepared using the casting method, after which the solution was transferred to a clean petri dish with a diameter (10 cm). Then, the samples were left for two days at room temperature to dry. The thickness of prepared samples was measured using a digital micrometre, and the thickness range was (140) μm. The stages of the experimental work and procedure are illustrated in figure (3.1).

Table (3.1) Weight percentages for (PMMA-PC) blend, (PMMA-PC/In_2O_3-GO).

PMMA wt.	PC wt.	In_2O_3 wt.	GO wt.	Con .of NPs(wt.%)	Weight of Sample(gm)
0.8	0.2	0	0	0	1
0.7888	0.1972	0.0098	0.0042	1.4	
0.7776	0.1944	0.0196	0.0084	2.8	
0.7664	0.1916	0.0294	0.0126	4.2	
0.7552	0.1888	0.0392	0.0168	5.6	

Table (3.2) Weight percentages for (PMMA-PC) blend, (PMMA-PC/Sb_2O_3-GO) nanocomposites.

PMMA wt.	PC wt.	Sb_2O_3 wt.	GO wt.	Con .of NPs(wt.%)	Weight of Sample(gm)
0.8	0.2	0	0	0	1
0.7888	0.1972	0.0098	0.0042	1.4	
0.7776	0.1944	0.0196	0.0084	2.8	
0.7664	0. 1916	0.0294	0.0126	4.2	
0.7552	0.1888	0.0392	0.0168	5.6	

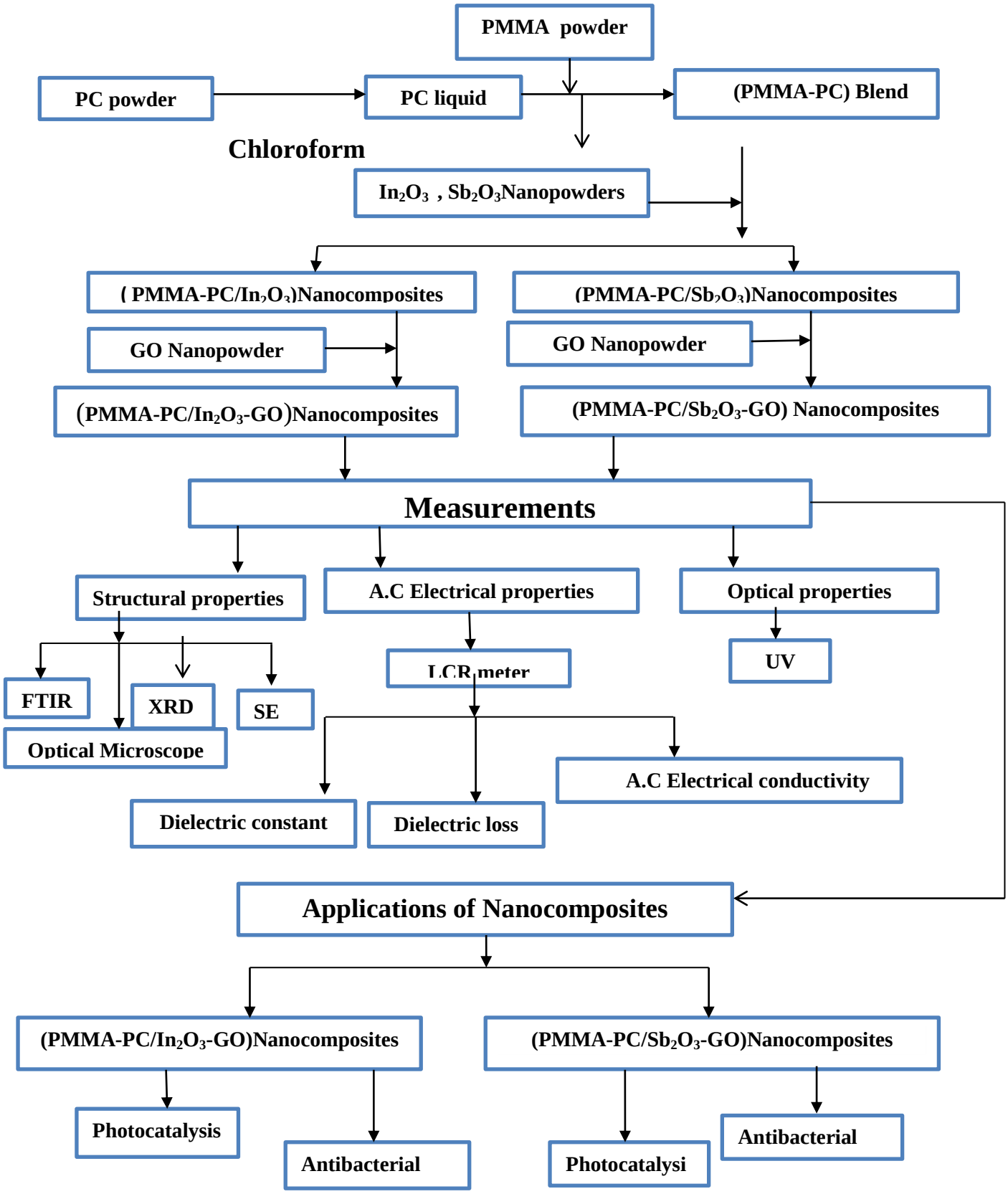

Figure (3.1) Scheme of experimental work.

3.4 Structural Properties for (PMMA-PC/In_2O_3-GO) and (PMMA-PC/Sb_2O_3-GO)Nanocomposites

3.4.1 Optical Microscopic Analysis

The optical microscope (supplied from Olympus name (ToupView) type (Nikon- 73346) was used to test the samples of (PMMA-PC/In_2O_3-GO),(PMMA-PC/Sb_2O_3-GO)nanocomposites at the University of Babylon / College of Education for Pure Sciences. with an enlargement (x10) as shown in Figure (3.2).

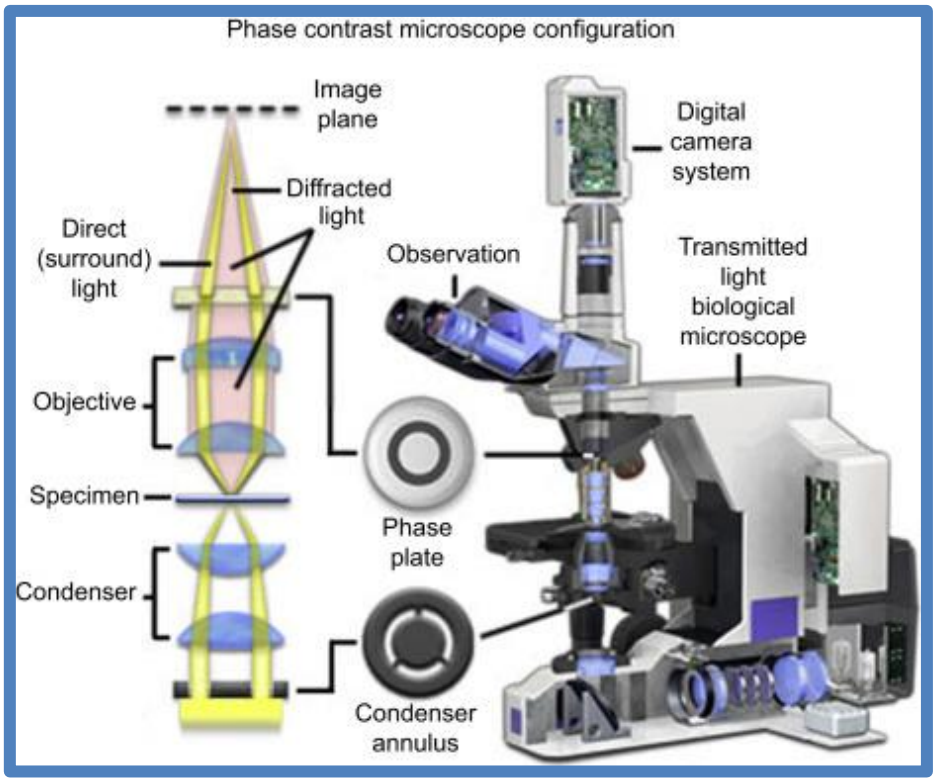

Figure (3.2): Optical Microscope.

3.4.2 Scanning Electron Microscope (SEM).

The surface morphology of (PMMA-PC/In_2O_3-GO) and (PMMA-PC/Sb_2O_3-GO)nanocomposites for different concentrations was examined by using scanning electron microscope (SEM) (Bruker Nano GmbH, company,

German origin, type vertex5600 LV SEM). The schematic diagram for scanning electron microscopy is shown in figure (3.3).

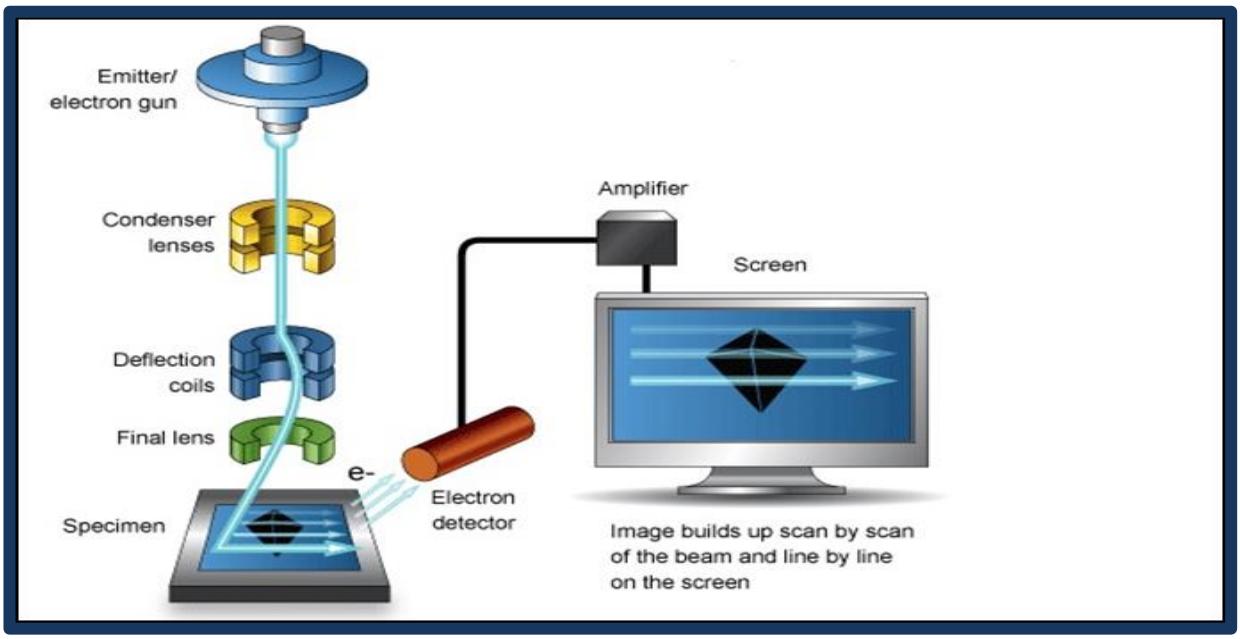

Figure (3.3) Schematic diagram for scanning electron microscopy.

3.4.3 X-Ray Diffraction (XRD)

All crystal structures of the polymeric preparations were characterized using an XRD (6000) diffraction device .Manufacturing and Country/ Tescan, France - Model/Xpert. An XRD 6000 X-ray diffraction instrument was used to examine the X-ray diffraction mode of the compound. X-ray diffraction (XRD) data were collected from (2θ) from (5º - 60º). It has the following characteristics, wavelength: 0.154 amperes, voltage: 40.0 (kilovolts), current: 30.0 (mA), high power: 3 (kilovolts), target: copper, measurement temperature: 25 °C and the type of X-ray generation tube (copper, Bα) shown in figure (3.4).

.

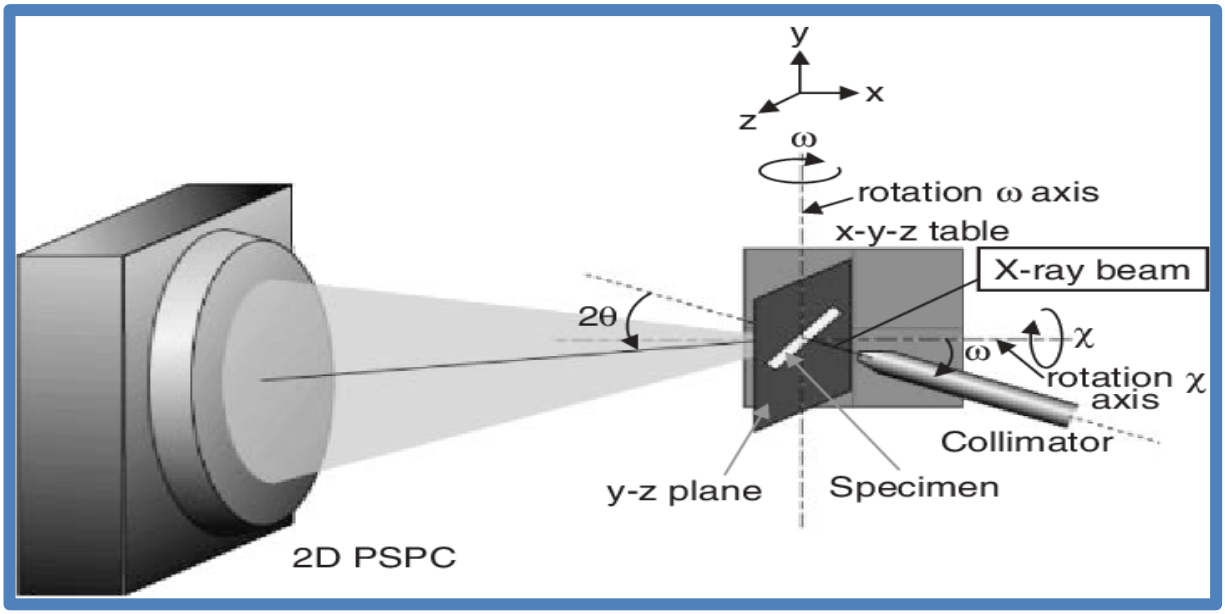

Figure (3.4): X-Ray Diffraction System

3.4.4 FTIR Spectrometer

One of the instruments based on infrared spectroscopy is the Fourier transform infrared ray spectrometer (FTIR). It is the most recent and preferred type of dispersive spectrometer. Its high precision, accuracy, speed, enhanced sensitivity, ease of operation, and sample nondestructiveness are all reasons for its success. Infrared spectroscopic technology is based on the atomic vibrations of a molecule, which only absorbs specific frequencies and energies of infrared radiation. Because different molecules have different infrared spectrums, FTIR can detect and classify them. Figure (3.5) depicts a block diagram of the FTIR working process. The FTIR spectrometer employs an interferometer to measure the energy transmitted to the sample. The infrared radiation emitted by the black body reaches the interferometer, where signal spectral encoding occurs. The interferogram signal is transmitted through or bounces off the sample surface, where specific energy wavelengths are absorbed. After passing through the detector, the beam is routed to a processing computer for Fourier transformation of energy signals. The FTIR spectra of (PMMA-PC)blend,(PMMA-PC/In_2O_3-GO) and (PMMA-PC/Sb_2O_3-GO)nanocomposites were recorded (Bruker

company, German origin, type vertex -70). was implemented in the University of Babylon /College of Education for Pure Sciences/Department of Physics. This study considered the wave number range (500–4000) cm^{-1}.

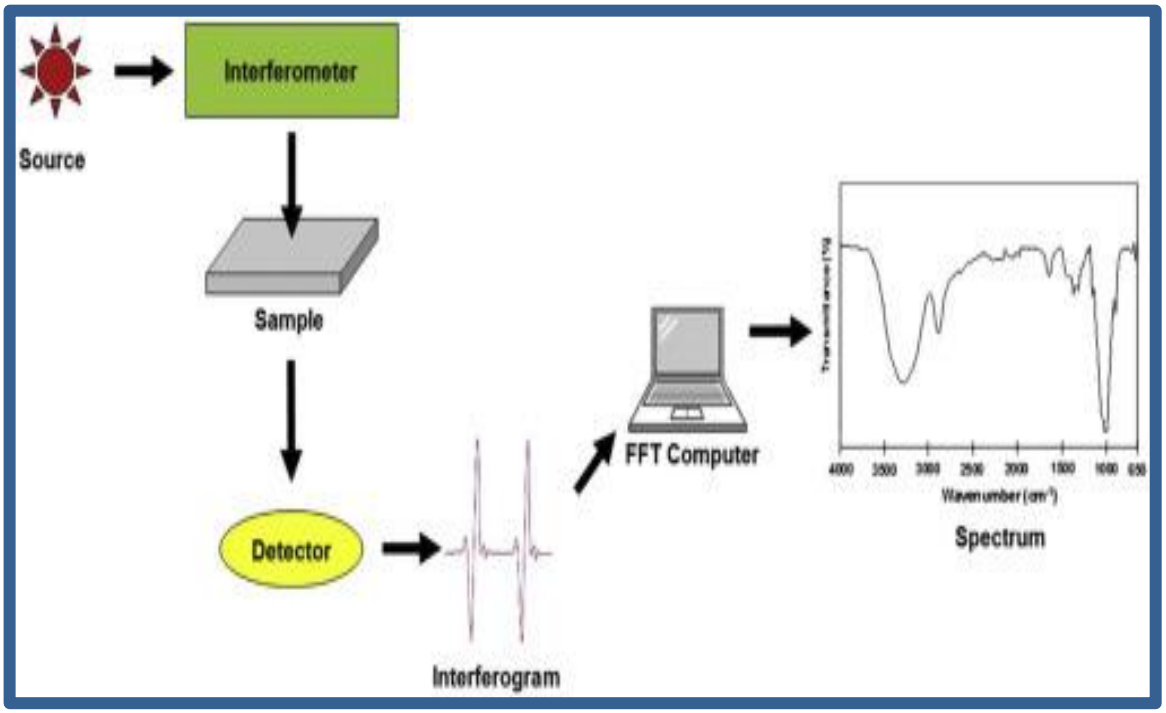

Figure (3.5) FTIR processing [15]

3.5 Optical Properties Measurements for Nanocomposites

The optical properties of (PMMA-PC) blend (PMMA-PC/In_2O_3-GO) and (PMMA-PC/Sb_2O_3-GO) nanocomposites were measured with a double beam spectrophotometer (Shimadzu, UV-18000A) at (260-860) nm. The figure illustrates that it is located at the University of Babylon/College of Education for Pure Sciences/Department of Physics (3.6).

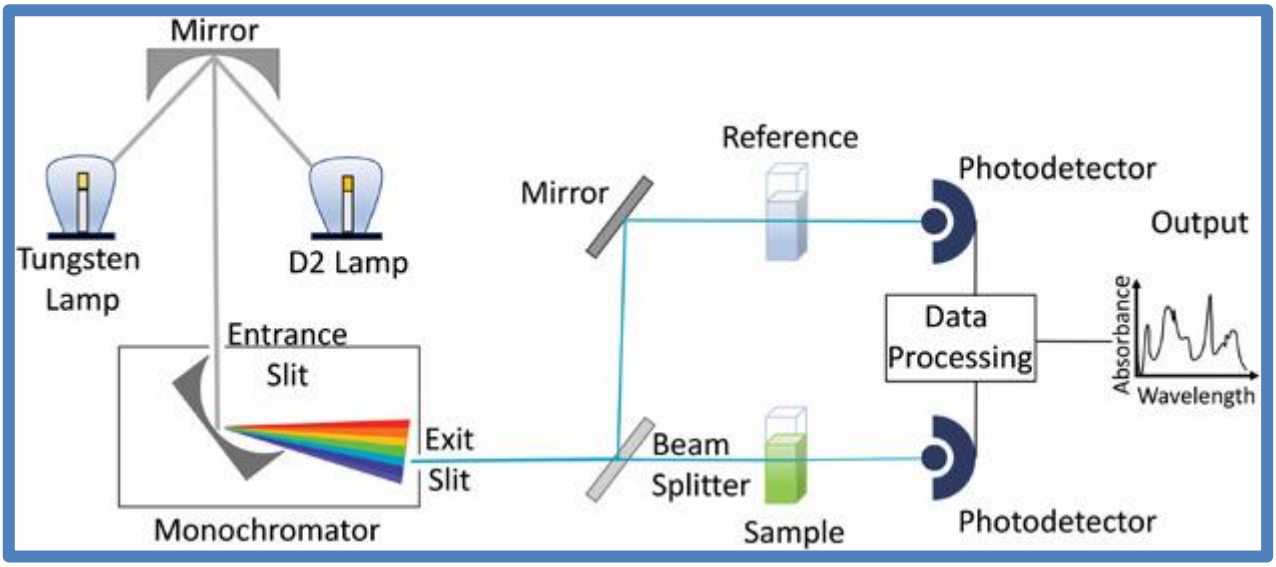

Figure (3.6) UV Photographic spectrophotometer.

3.6 Measurements of A.C Electrical Properties

Figure (3.7) illustrates the A.C. electrical measurement system used in the study. The dissipated factor and capacity were recorded for all samples at room temperature across a frequency range of (100-5x10^6) Hz. This data determined the dielectric constant, dielectric loss, and conductivity. The Department of Physics at the University of Babylon, College of Education for Pure Sciences, utilized the LCR Hi TESTER, specifically the HIOKI 3532-50 model, to measure the A.C. Electrical Conductivity

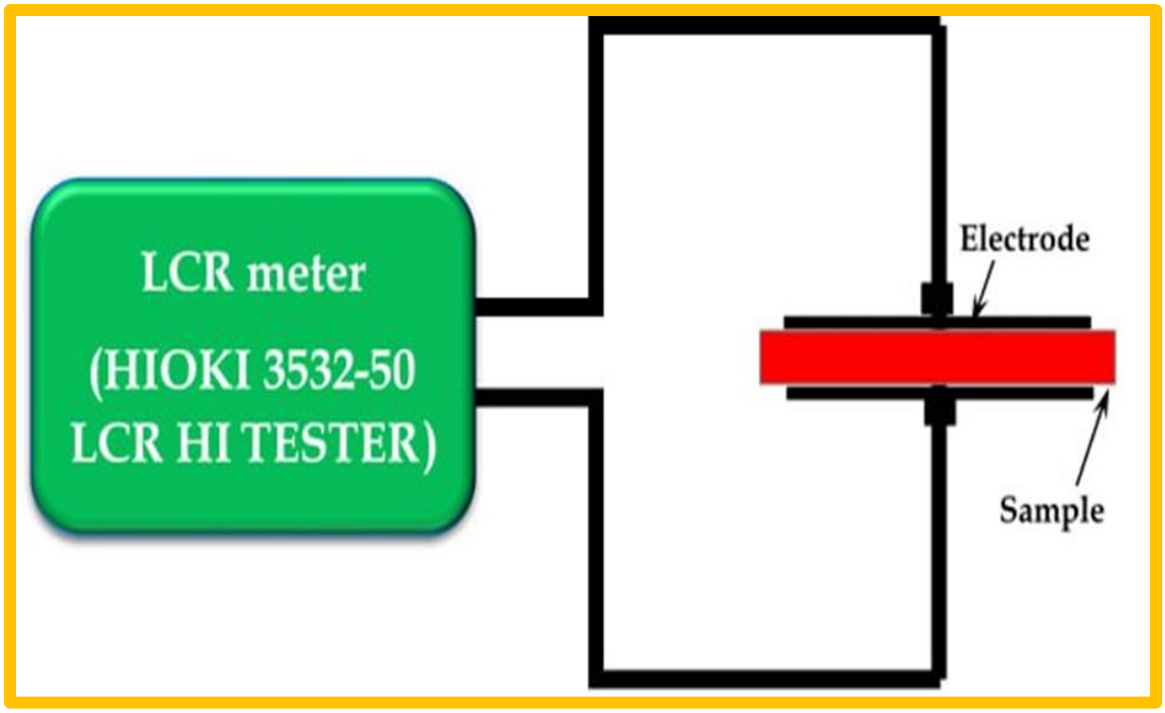

Figure (3.7) Schematic diagram for A.C. electrical properties measurement.

3.7 Photocatalytic Activity Application Measurements

To investigate the photocatalytic activity of various nanocomposites, including pure (PMMA-PC) blend, (PMMA-PC/In_2O_3-GO) and (PMMA-PC/Sb_2O_3-GO) nanocomposites, a 100ml aqueous solution of Methylene orange (MO) dye with a concentration of 20 parts per million (ppm) was placed in a pyrex glass container. Each of the prepared samples was introduced into the solution while stirring magnetically. The mixture was then exposed to ultraviolet light with a power of 135W in a homogenous mixture-illuminated ultraviolet light exposure cabinet equipped with a magnetic stirrer. The solution was stirred in the dark for 90 minutes to achieve adsorption/desorption equilibrium. Then, at intervals of 15 minutes for 1.5 hours, 10 ml samples of the Methylene orange solution were taken and centrifuged at 3000 rpm. The absorbance of the samples was measured using a double-beam spectrophotometer (Shimadzu, UV-18000A) in the wavelength range of 200-600 nm, with maximum absorption occurring at approximately 660 nm, as shown in figure (3.8).

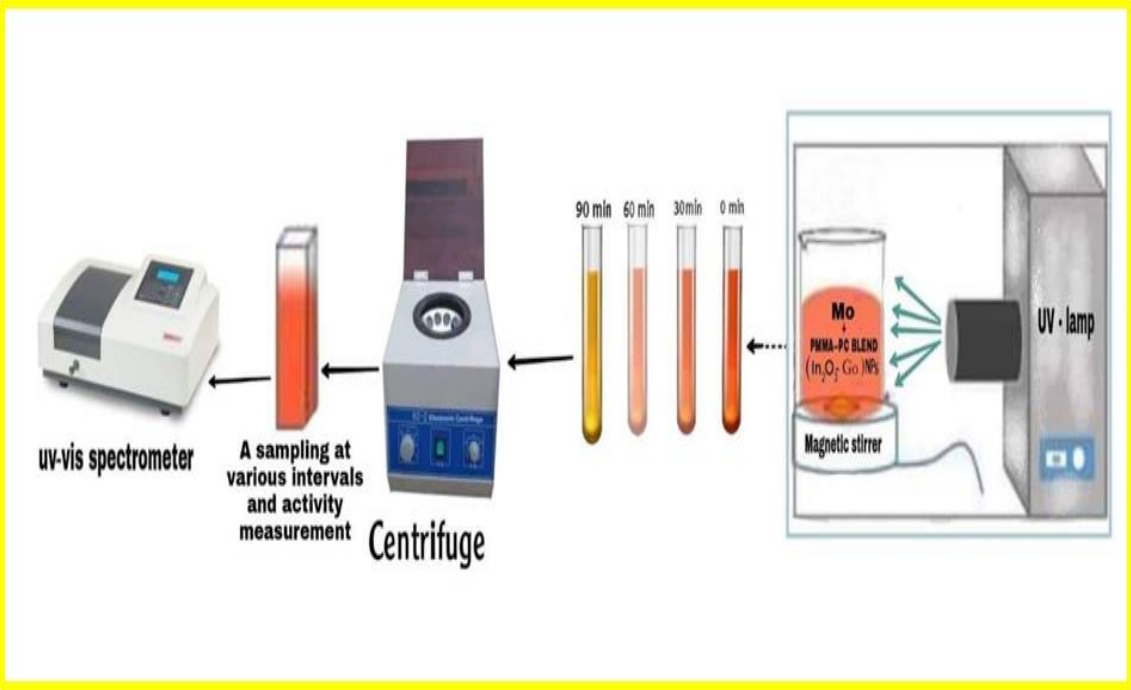

Figure (3.8) Experimental set-up.A scheme showing nanocomposites mixed with methyl orange (MO) dye

3.8 Antibacterial Activity Effect Measurements of (PMMA-PC/In_2O_3-GO) and (PMMA-PC/Sb_2O_3-GO)Nanocomposites.

A disc diffusion method evaluated the effectiveness of (PMMA-PC/In_2O_3-GO) and (PMMA-PC/Sb_2O_3-GO)nanocomposites against bacterial growth. The nanocomposites' antibacterial activities were tested against gram-positive (*Staphylococcus aureus*) and gram-negative (*Escherichia coli*) bacteria. The bacteria were cultured in Muller-Hinton Medium, and the nanocomposite solutions were added to the media and incubated at 37°C for 24 hours. The diameter of the inhibition zone was measured as an indicator of the nanocomposites' ability to prevent bacterial growth.

4.1 Introduction

This chapter presents the findings of various measurements, including structural, A.C electrical, and optical characterizations of (PMMA-PC/In_2O_3-GO) and (PMMA-PC/Sb_2O_3-GO) nanocomposites. The impact of adding indium trioxide , antimony trioxide and graphene oxide nanoparticles to the (PMMA-PC) blend on its structural, A.C electrical, and optical properties are also discussed. The chapter also delves into the potential applications of these nanocomposites in antibacterial and photocatalytic activity.

4.2 The Structural Properties of (PMMA-PC/In_2O_3-GO) and (PMMA-PC/Sb_2O_3-GO) Nanocomposites

4.2.1 Optical Microscope

The examination of how nanoparticles are dispersed in a polymer mixture is known as the microscopy of nanocomposites. In figures (4.1) and (4.2), the arrangements of indium dioxide, antimony dioxide, and graphene dioxide nanoparticles in a (PMMA-PC) polymer blend are displayed at a magnification power of (40x). The microscope images indicate that the nanoparticles aggregate as clusters at lower concentrations [104]. However, as In_2O_3, GO and Sb_2O_3 nanoparticles' concentration increases form a network of paths within the (PMMA-PC) polymer blend[105].

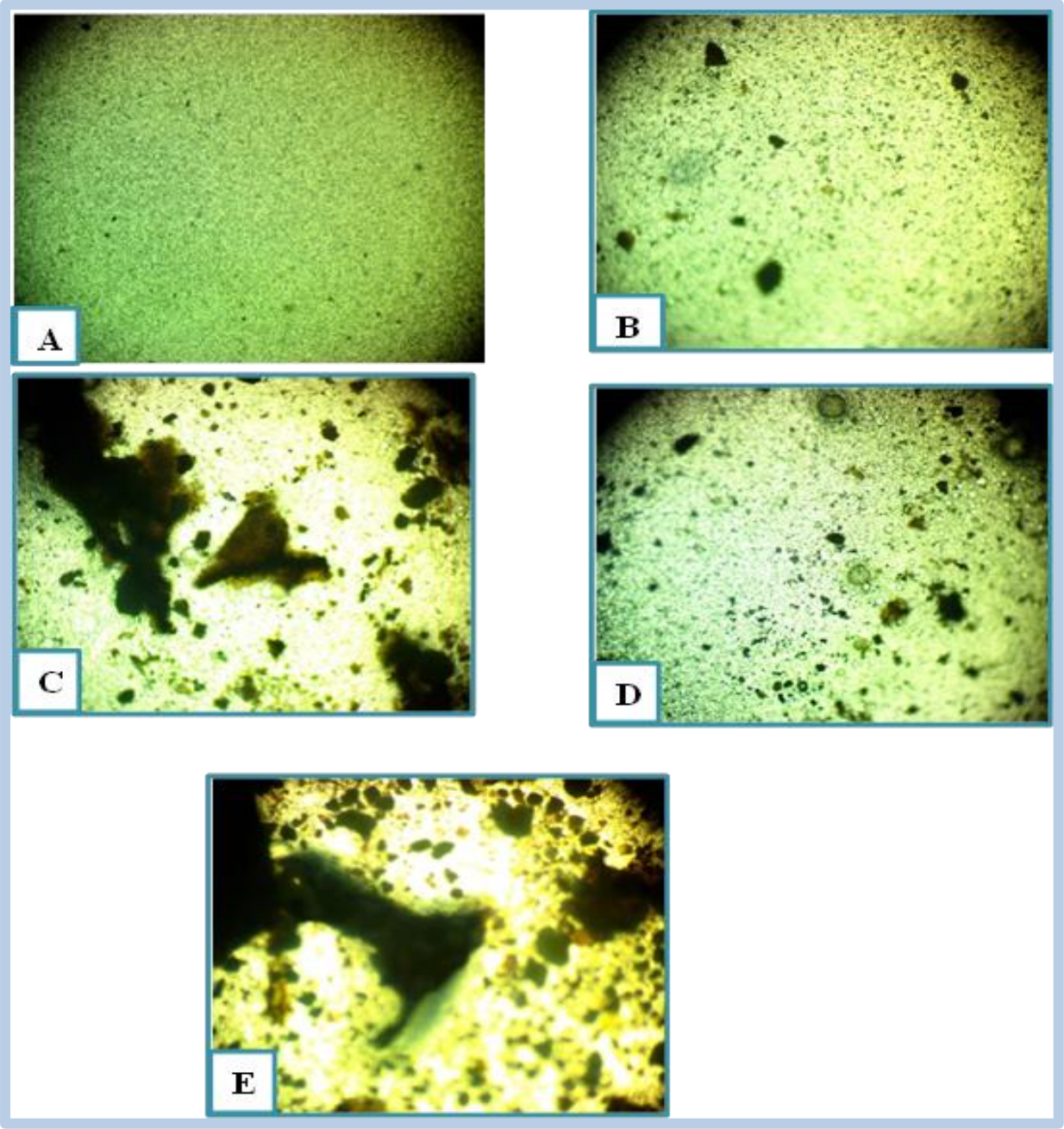

Figure(4.1) photomicrographs for (PMMA-PC/In_2O_3-GO) nanocomposites (A)for (PMMA-PC) blend (B) for 1.4wt% In_2O_3-GO nanoparticles,(C) for 2.8wt% In_2O_3-GO nanoparticles,(D) for 4.2wt% In_2O_3-GO nanoparticles, (E) for 5.6wt% In_2O_3-GO nanoparticles

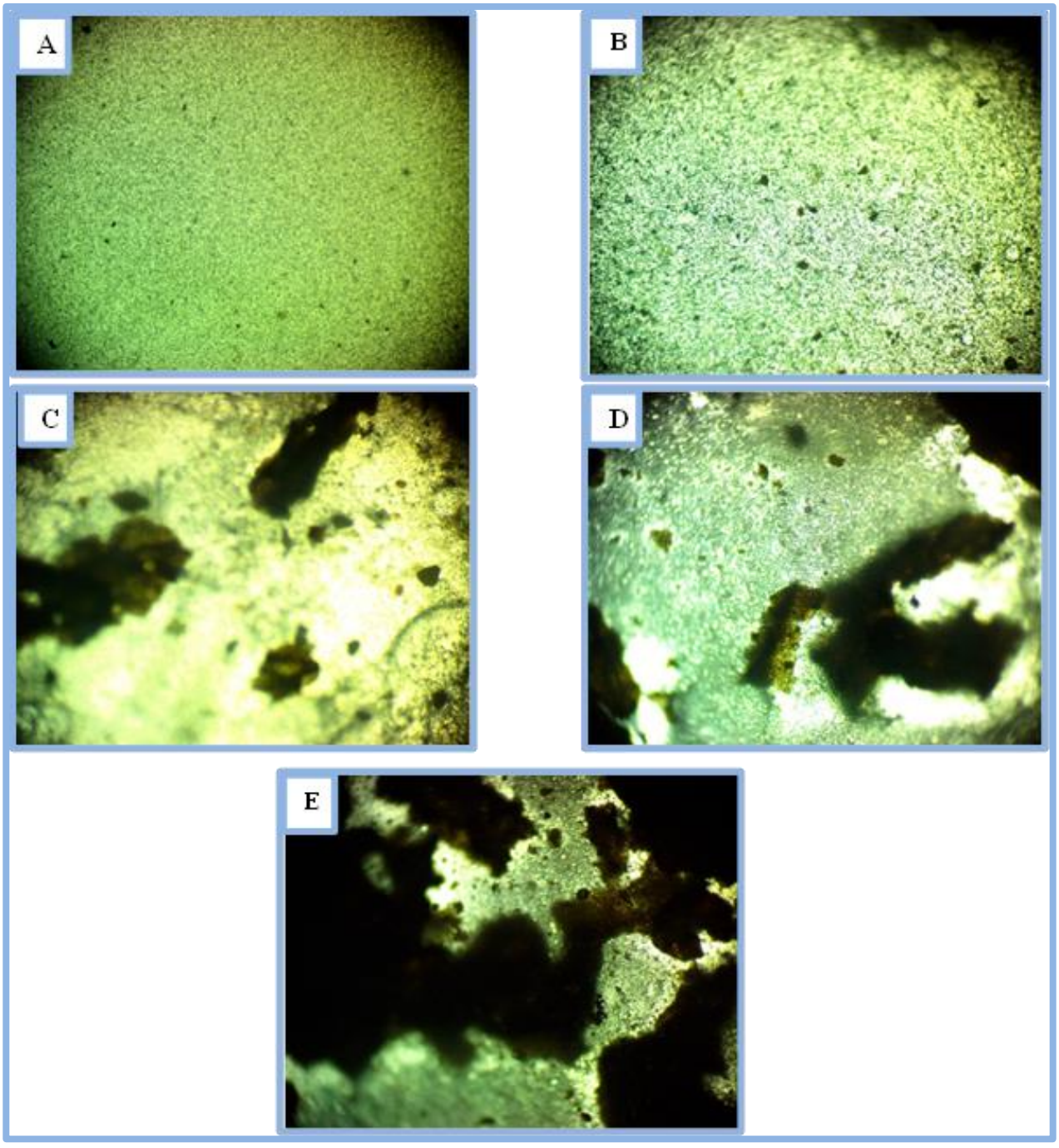

Figure(4.2) photomicrographs for (PMMA-PC/Sb_2O_3-GO) nanocomposites (A)for (PMMA-PC) blend (B) for 1.4wt% Sb_2O_3-GO nanoparticles,(C) for 2.8wt% Sb_2O_3-GO nanoparticles, (D) for 4.2wt% Sb_2O_3-GO nanoparticles, (E) for 5.6wt% Sb_2O_3-GO nanoparticles.

4.2.2 Scanning Electron Microscope (SEM)

The surface morphology of (PMMA-PC/In_2O_3-GO) and (PMMA-PC/Sb_2O_3-GO) nanocomposites with varying concentrations of (In_2O_3 Sb_2O_3 and GO) NPs is illustrated in Figures (4.3) and (4.4) through SEM images. The figure displays the surface morphology of the nanocomposite. At low concentrations of (In_2O_3 Sb_2O_3 and GO) NPs, the SEM image reveals randomly distributed aggregates or particles on the surface, attributed to the presence of 1.4% of (In_2O_3 ,Sb_2O_3 and GO) NPs that are aggregated in clusters [106]. As the concentration of nanoparticles increases, the number and size of white dots on the surface also increase, indicating the formation of larger clusters that extend to form network paths of aggregates throughout the PMMA/PC blend. The surface morphology of the films exhibits a uniform density of grain boundaries. The results indicate that nanoparticles tend to form well-dispersed aggregates in the (PMMA-PC) blend films, which could indicate a homogeneous growth process [107]. The change is due to the strong interfacial interaction of the functional groups on the surface of (In_2O_3 Sb_2O_3 and GO) NPs nanoparticles with the blend polymer. This results in a significant change in the nanocomposite morphology and mechanical response [108].

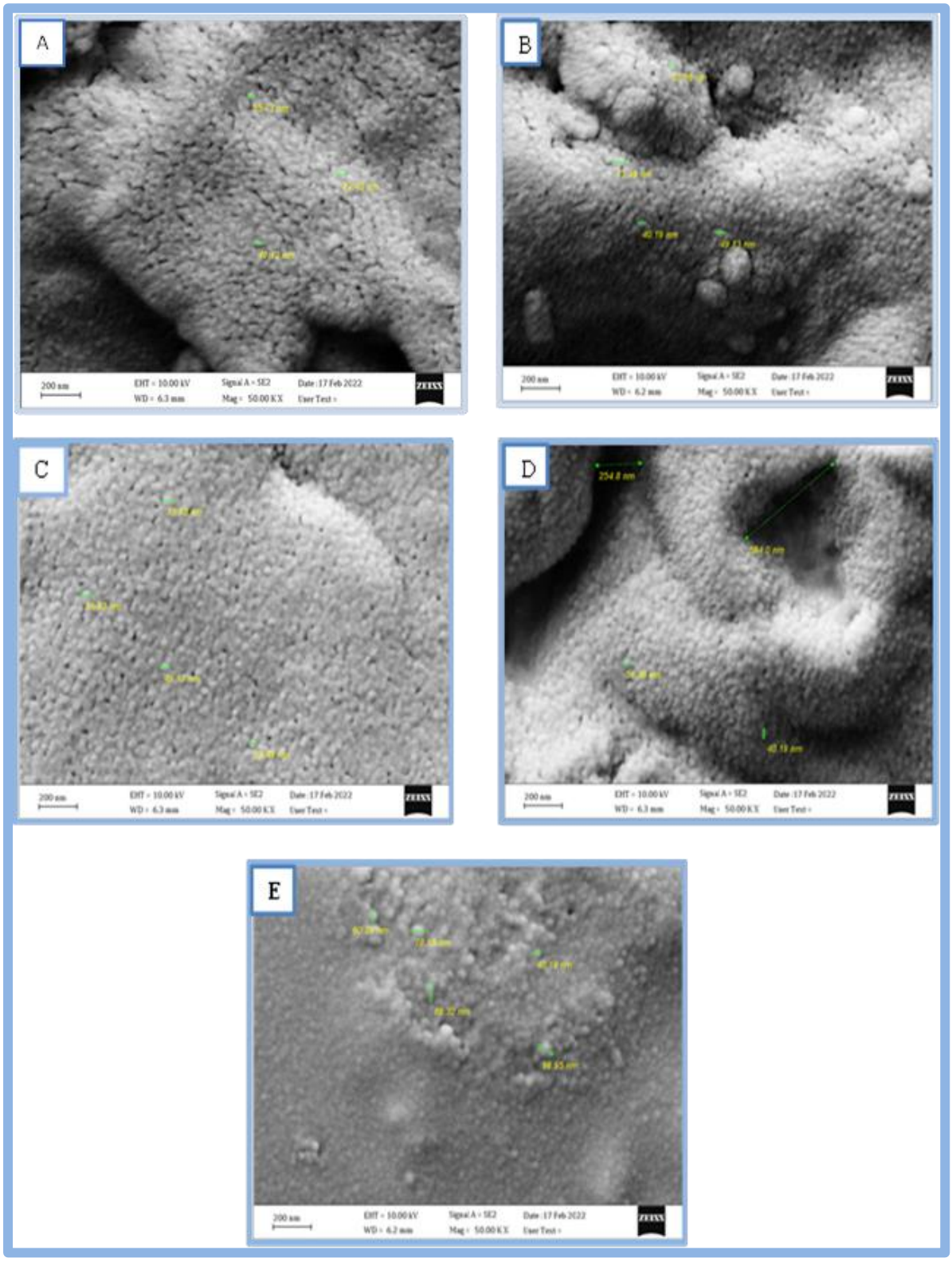

Figure (4.3) SEM images for (PMMA-PC/In_2O_3-GO) Nanocomposites: (A) for (PMMA-PC) blend (B) for 1.4 wt.% In_2O_3-GO NPs (C) for 2.8 wt.% In_2O_3-GO NPs (D) for 4.2wt.% In_2O_3-GO NPs (E) for 5.6 wt.% In_2O_3-GO NPs.

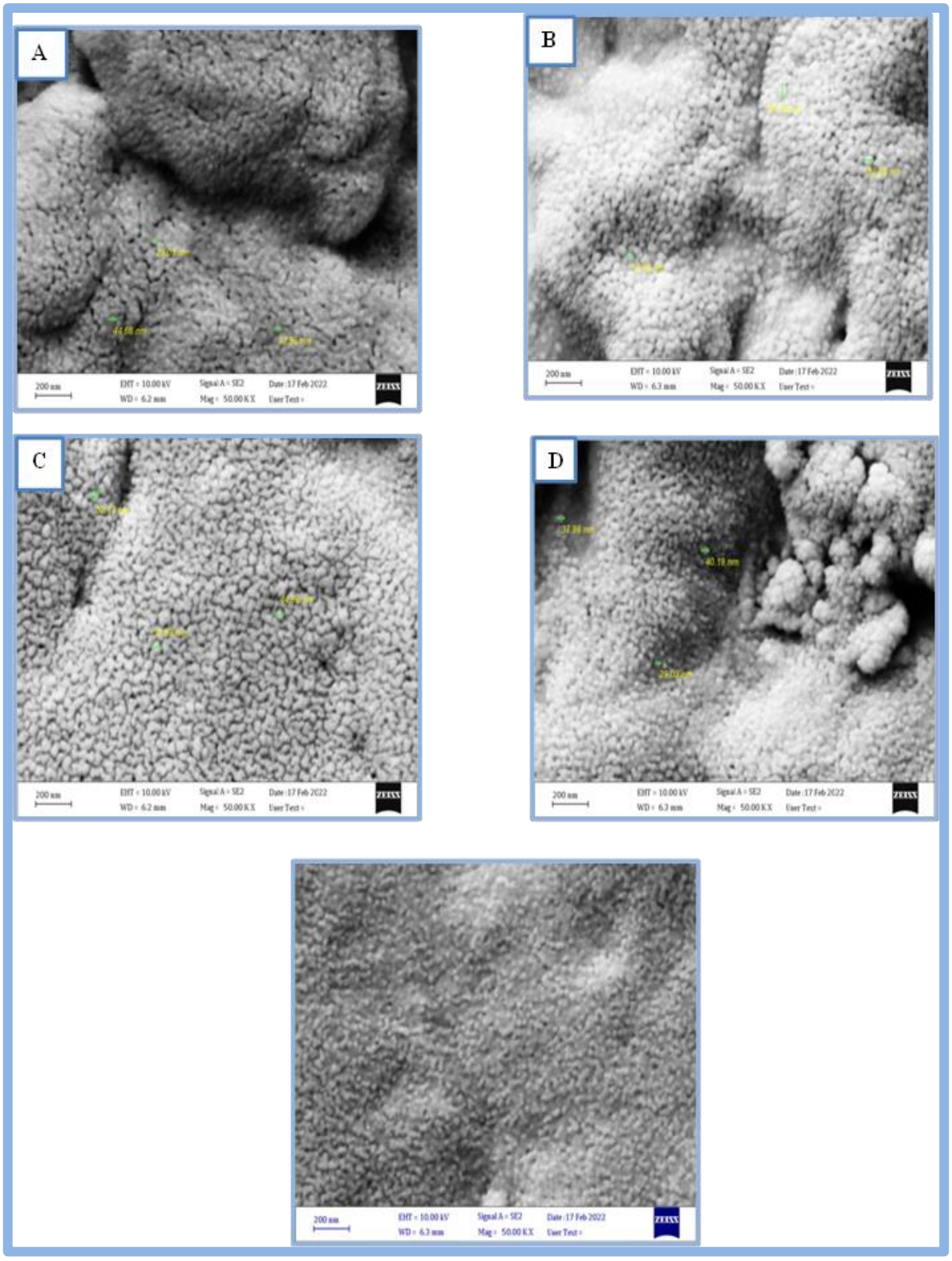

Figure (4.4) SEM images for (PMMA-PC/Sb_2O_3-GO) Nanocomposites: (A) for pure (B) for 1.4 wt.% Sb_2O_3-GO NPs (C) for 2.8 wt.% Sb_2O_3-GO NPs (D) for 4.2wt.% Sb_2O_3-GO NPs (E) for 5.6 wt.% Sb_2O_3-GO NPs.

4.2.3 X-Ray Diffraction Measurement

Figure (4.5) shows the XRD patterns of the prepared pure Sb_2O_3, In_2O_3 and GO nanoparticles, The figure shows three peaks near 13.70°, 26° and 30.8° which are matched to (111), (222) and (400) reflections of (Sb_2O_3) respectively. The XRD spectrum indicated that the sample was in the FCC structure of Sb_2O_3 nanoparticles with the lattice parameter: a = 11.138 A˚, which matched the literature report (PCPDF Nos: 72-1334 and 75-1565) [109]. The figure also shows the obtained three peaks corresponding to (100), (400), and (440) directions of the cubic In_2O_3 crystal structure which is corresponding to the positions 2θ = 29.9 °, 34.1 °, and 47.8° respectively. Also, the XRD measurements revealed that the intensity of peak (100) orientation is predominant which is in agreement with the JCPDS (card No. 06-0416) standard data file of indium trioxide (In_2O_3) [110]. The observed X-ray diffraction peaks match, which indicates the presence of the cubic bixbite crystal structure of In_2O_3. This crystal structure belongs to the Ia-3 space group. The XRD pattern of graphene oxide shows a peak at 2θ = 10.1° (d-spacing of 8.9 Å), the (100) diffraction peak at 2θ = 43.0° according to a d-spacing of 2.13 Å, confirming the successful GO synthesis[111].

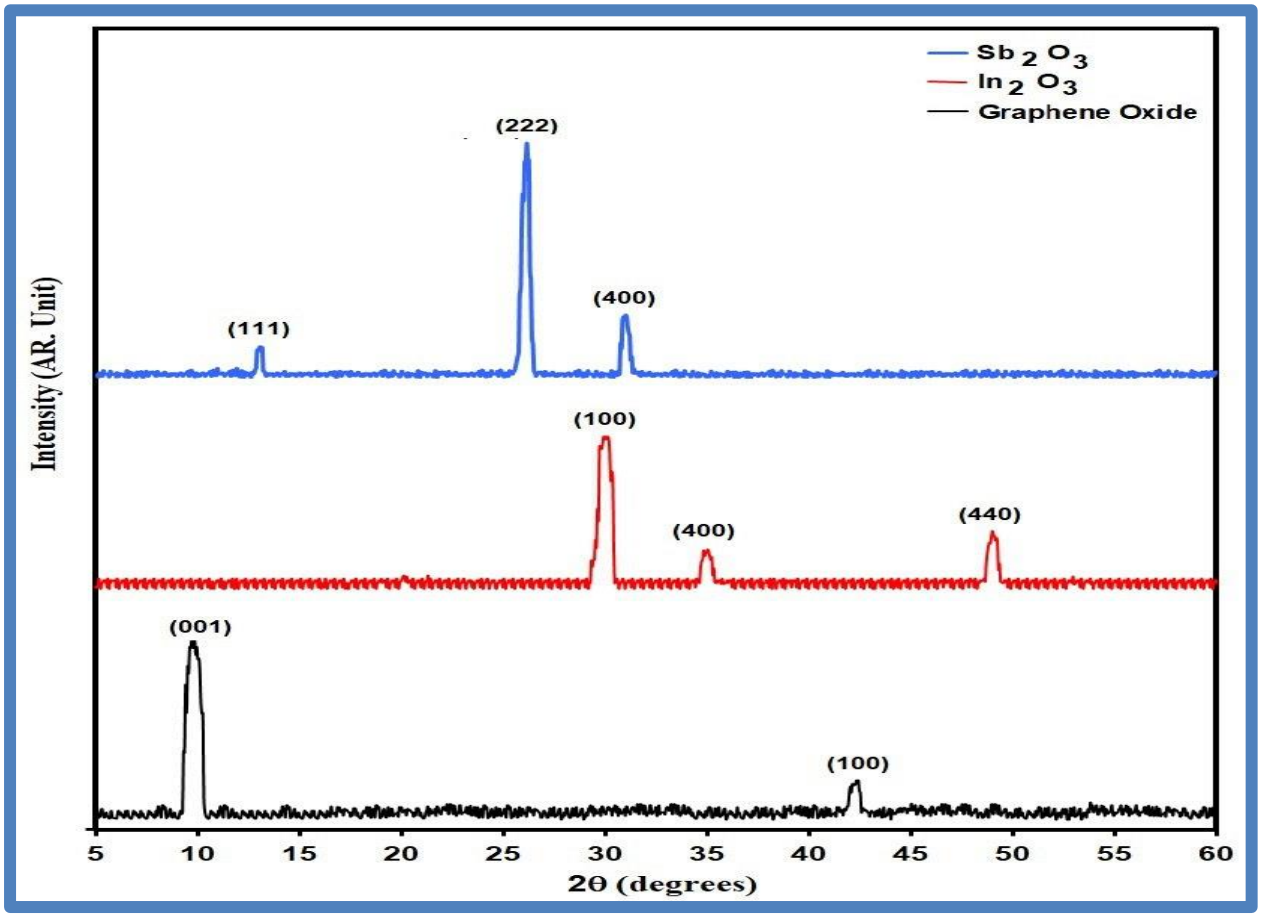

Figure (4.5) XRD pattern of the (In_2O_3, $Sb_2O_3$and GO) nanoparticals.

4.2.4 Fourier Transform Infrared Radiation of nanocomposites.

Figures (4.6) and (4.7) illustrate the FTIR spectra of various nanocomposites, including (PMMA, PC) blend, (PMMA-PC/In_2O_3-GO) and (PMMA-PC/Sb_2O_3-GO) nanocomposites with varying concentrations of (In_2O_3, $Sb_2O_3$and GO) in the wave number range of (600-4000) cm^{-1}.The interactions between atoms in the system have been analyzed using FTIR spectroscopy [112]. Such interactions can cause changes in the vibrational modes of the molecules in the polymer blend. The presence of peaks around 2878 cm^{-1} of PC and at 1655 cm^{-1} of PMMA in the (PMMA-PC) blend suggests that the blend components are miscible. The rise observed around 2878 cm^{-1} is characteristic of asymmetry CH stretching of the CH_2 group. The bands at 1341 cm^{-1} and 1278 cm^{-1} correspond to CH_2 asymmetric bending and CH_2 symmetric twisting

The peak around 1655 cm^{-1} represents the C=O stretching of the PMMA group. The peak at 1465 cm^{-1} was assigned to the CH_2 scissoring mode of the PC. The strong band observed at 1097 cm^{-1} for all nanocomposite samples was attributed to the OH bending mode. The stretching vibration of C-O at 960 cm^{-1} is due to PC with CH_2 rocking asymmetric vibration. The band at 841 cm^{-1} is due to the CH_2 rocking mode of PMMA and some C-O stretching in PC [113]. The transmittance in the figures decreases with increasing concentrations (In_2O_3, Sb_2O_3 and GO) nanoparticles, indicating an increase in nanocomposite density[114]. The analysis revealed no new absorption peaks, indicating no interactions between the (PC-PMMA) polymer matrix and (In_2O_3, Sb_2O_3 and GO) nanoparticles [115]. Also, it can be noticed that there is a decrease in transmittance with increasing the proportion of (In_2O_3, Sb_2O_3 and GO) nanoparticles. The increased density of the films means an increase of atoms and ions in the light path and an increase in the absorbance at UV inverse the IR, as shown in figures (4.6and 4.7). The results showed that the change in film thickness had a slight effect [116].

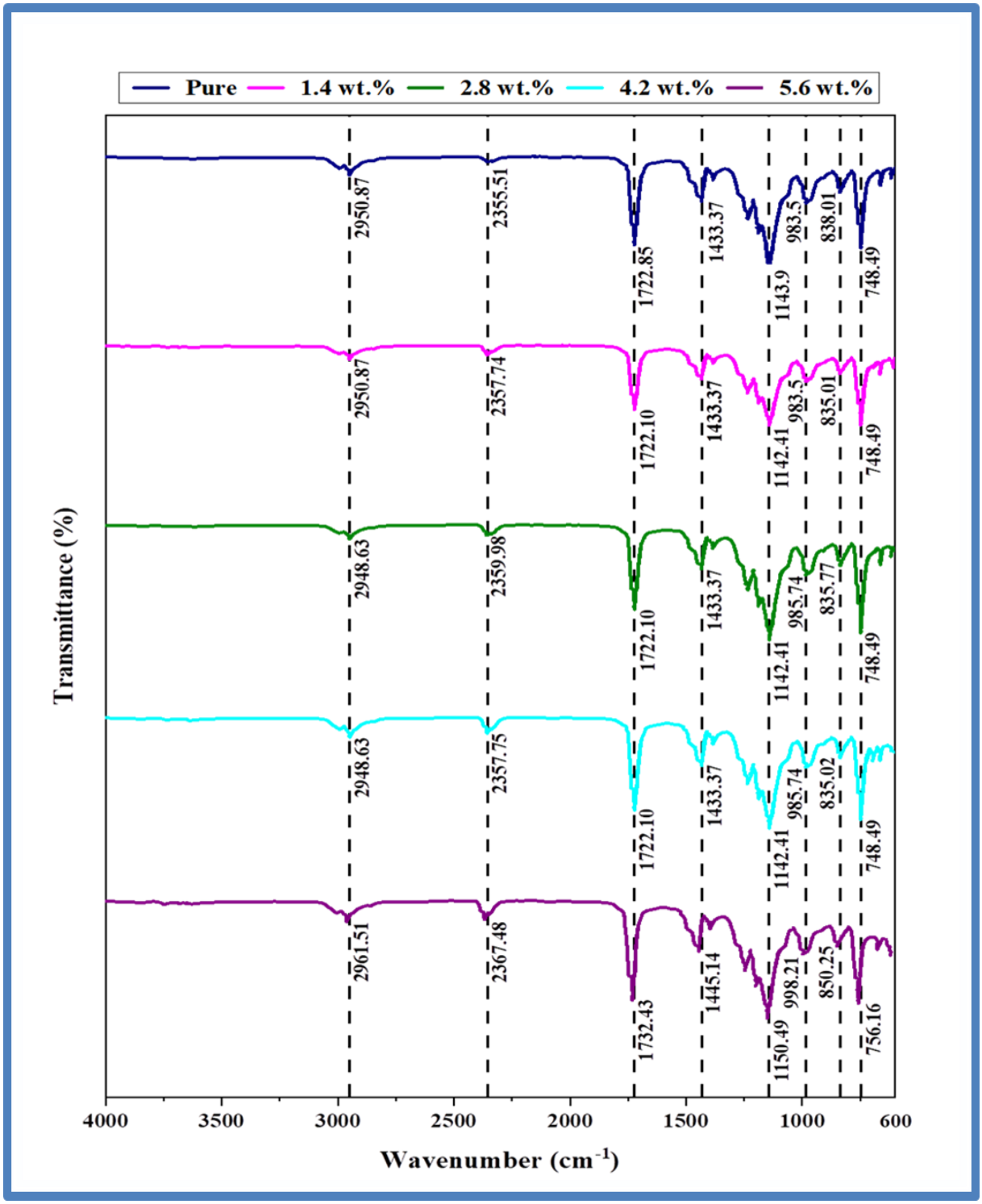

Figure(4.6) FTIR spectra for (PMMA-PC/In_2O_3-GO) Nanocomposite

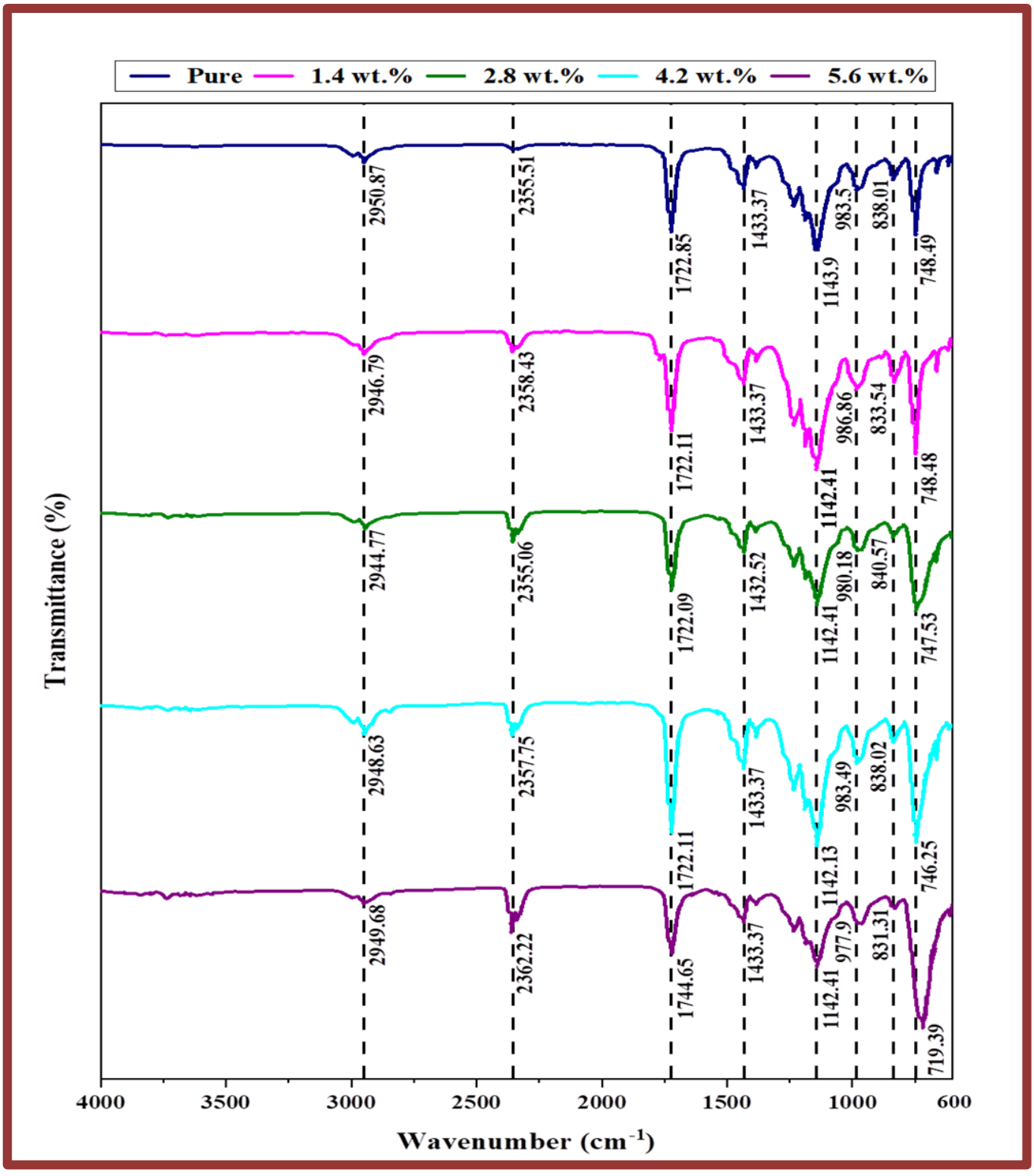

Figure(4.7) FTIR spectra for (PC-PMMA/Sb_2O_3-GO) Nanocomposite.

4.3 The Optical Properties of (PMMA-PC/In_2O_3-GO) and (PMMA-PC/Sb_2O_3-GO) Nanocomposites

The purpose of studying the properties of the (PMMA-PC/In_2O_3-GO) and (PMMA-PC/Sb_2O_3-GO) nanocomposites is to investigate the effect of adding Sb_2O_3, In_2O_3 and GO nanoparticles on the optical properties of polymers. The researchers aim to characterize the optical properties of the nanocomposites by measuring the spectrum of absorbance for the films at room temperature and calculating various optical constants, such as absorption coefficient, extinction coefficient, and energy gaps. By identifying the types of electronic transitions, the researchers can gain insight into the behaviour of the nanocomposites at the molecular level [117]. The absorption and extinction coefficients are essential parameters describing the absorption and scattering of light by the nanocomposites. These properties depend on the size and concentration of the nanoparticles and the polymer blend. By measuring these properties, the researchers can gain insight into nanocomposites' light absorption and scattering mechanisms. The energy gap is another important parameter that characterizes the optical properties of materials. The energy gap is related to the material's band structure and determines the types of electronic transitions that can occur [118]. By calculating the energy gap, the researchers can gain insight into the electronic properties of the nanocomposites and how they are affected by the addition of nanoparticles. Overall, the study of the optical properties of the (PMMA-PC/In_2O_3-GO) and (PMMA-PC/Sb_2O_3-GO)nanocomposites is essential for understanding the behaviour of these materials and their potential applications in optoelectronic devices[119].

4.3.1 The Absorbance of (PMMA-PC/In_2O_3-GO) and PMMA-PC/Sb_2O_3-GO) nanocomposites

Figures (4.8) and (4.9) depict the changes in absorbance (A) of (PMMA-PC/In_2O_3-GO) and (PMMA-PC/Sb_2O_3-GO)nanocomposites with the wavelength (λ) of the incident light. As indicated by the figures, the absorbance of all prepared samples of nanocomposites increases with an increase in the concentration of (In_2O_3, Sb_2O_3 and GO) nanoparticles, owing to the augmented number of charge carriers with increasing nanoparticle concentration. At a concentration of 5.6% (In_2O_3, Sb_2O_3 and GO) nanoparticles, the absorbance of the nanocomposites increased by about 51% and 49% respectively, at λ=560nm. This behavior is beneficial for optoelectronics, photocatalysis, and solar cells. Generally, the absorbance decreases as the wavelength increases for all prepared nanocomposites. This implies that the incident photon cannot excite the electron and move it from a lower to a higher energy level, as the energy of the incident photon is less than the value of the energy gap of the nanocomposites. In the UV region, all samples of nanocomposites have high absorbance values, owing to the excitations of donor-level electrons to the conduction band at these energies. The high absorbance in the UV region is attributed to the energy of photons sufficient to interact with atoms[120]. The absorption spectrum of (the PMMA-PC) blend is limited in the UV region, but it is enhanced upon adding (In_2O_3, Sb_2O_3 and GO) nanoparticles due to the high energy gap of the blend. The curves of (PMMA-PC/In_2O_3-GO) and (PMMA-PC/Sb_2O_3-GO)nanocomposites with high (In_2O_3, Sb_2O_3, GO) concentrations show a clear peak in the UV region and less absorption in the visible region. The peak of high absorption is observed at around 260 nm, owing to the absorption of (In_2O_3, Sb_2O_3 ,and GO) nanoparticles due to an increase in the number of charge carriers. At the visible and near-infrared regions, the absorbance for all

nanocomposites samples decreases with an increase in wavelength, as the energy of incident photons is insufficient to interact with atoms, leading to photon transmission [121]. The (PMMA-PC/In_2O_3-GO) and (PMMA-PC/Sb_2O_3-GO)nanocomposites with 5.6% concentration of (In_2O_3, Sb_2O_3 and GO) NPs have the highest absorbance owing to the high diffusivity of (In_2O_3, Sb_2O_3 ,and GO) nanoparticles in the (PMMA-PC) blend [122].

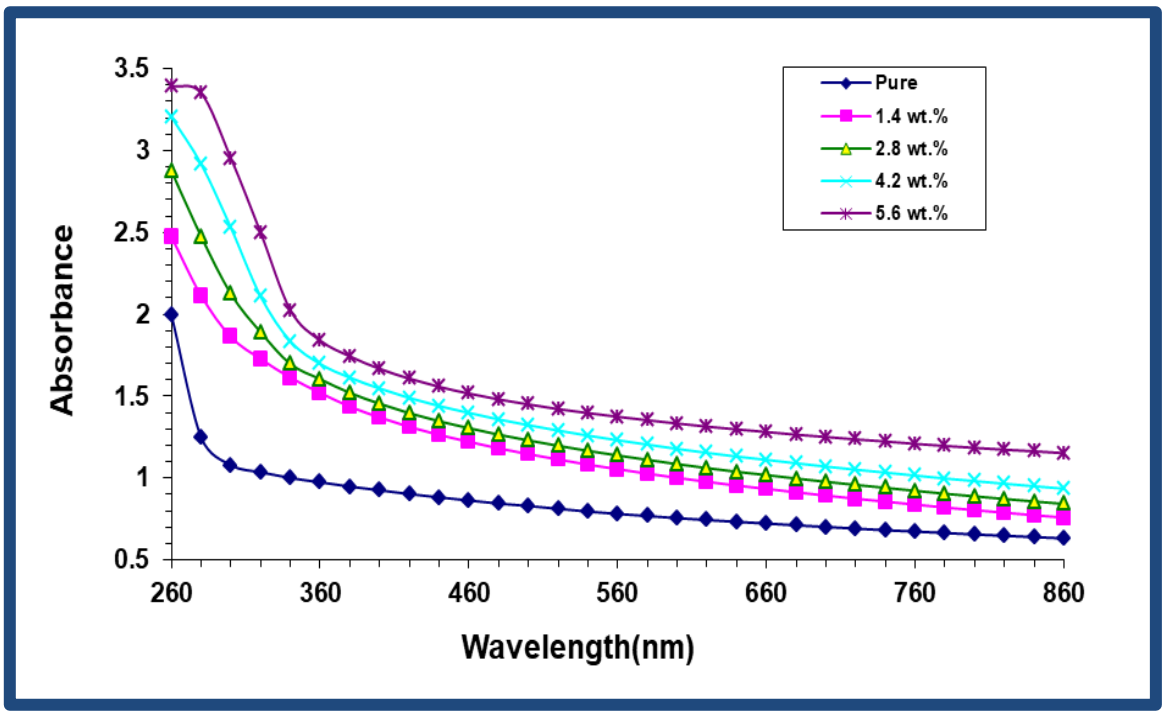

Figure (4.8) The absorbance spectra as a function of wavelength of (PMMA-PC-In_2O_3-GO) nanocomposites .

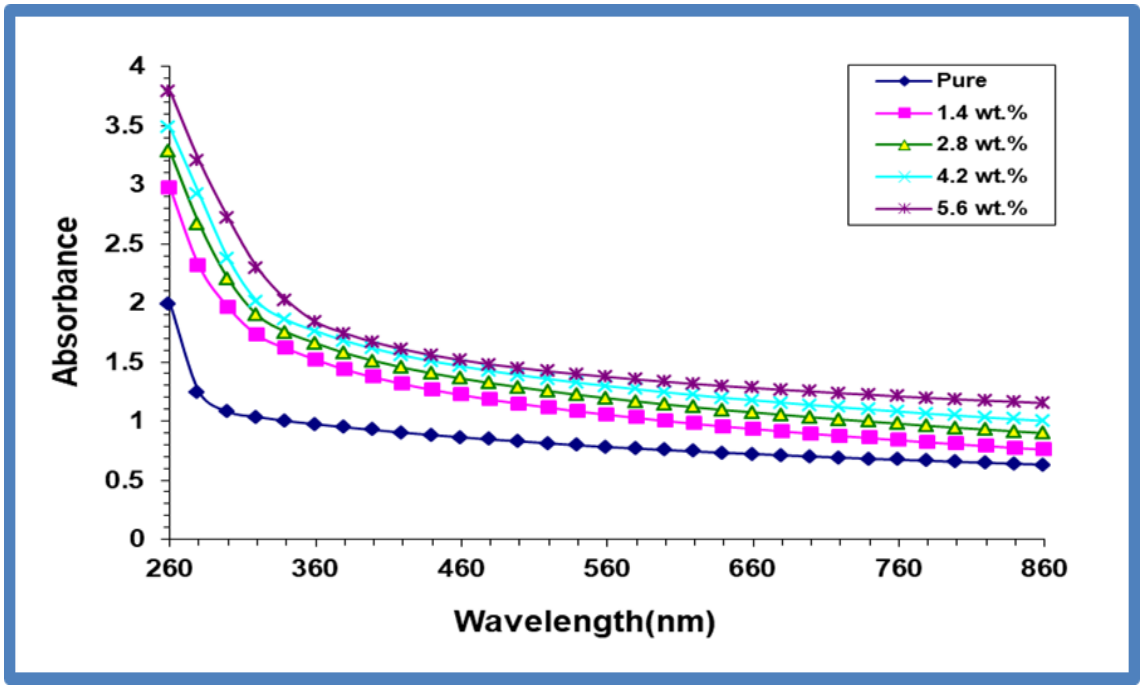

Figure (4.9) The absorbance spectra as a function of wavelength of (PMMA-PC/Sb_2O_3-GO) Nanocomposites.

4.3.2 Transmittance of (PMMA-PC/In_2O_3-GO) and (PMMA-PC/Sb_2O_3-GO) Nanocomposites.

Figures (4.10) and (4.11) illustrate the changes in transmittance (T) with the wavelength (λ) of incident light for (PMMA-PC/In_2O_3-GO) and (PMMA-PC/Sb_2O_3-GO) nanocomposites, respectively. It indicates an ion transfer mechanism between (PMMA–PC) blend and (In_2O_3, Sb_2O_3 and GO) NPs. The transmittance of undoped (PMMA-PC)in the visible region is about 91.6%. Such a value indicates an excellent excitation leads to a sharp electron transition from the valence band to the conduction band. Interestingly, introducing (In_2O_3, Sb_2O_3 and GO) NPs into(PMMA-PC) blend leads to a gradual and nonlinear decrease in transmittance in the visible region [123]. Our results indicate with increasing the concentration of ($In_2O_3Sb_2O_3$ andGO) NPs wt % the transmittance of (PMMA-PC/In_2O_3-GO) and (PMMA-PC/Sb_2O_3-GO) nanocomposite a decrease to 69% and 61 % at 560 nm, respectively. The loss

of transparency is attributed to scattering by NPs within the polymeric matrix. This occurs when the particle size is smaller than the wavelength, or it could happen as a result of electron transitions between the (PMMA-PC) blend and (In_2O_3-GO)NPs.In the UV region, the transmittance of the polymer blend and nanocomposites exhibits more decrement than in the visible region, and the addition of (In_2O_3, Sb_2O_3 and GO) nanoparticles significantly reduces transmittance in the UV region, which decreases with increasing concentration of (In_2O_3, Sb_2O_3 and GO) nanoparticles in the nanocomposite [124]. The values of absorbance and transmittance for the prepared nanocomposites at λ=560 nm are listed in Tables (4.1) and (4.2), respectively.

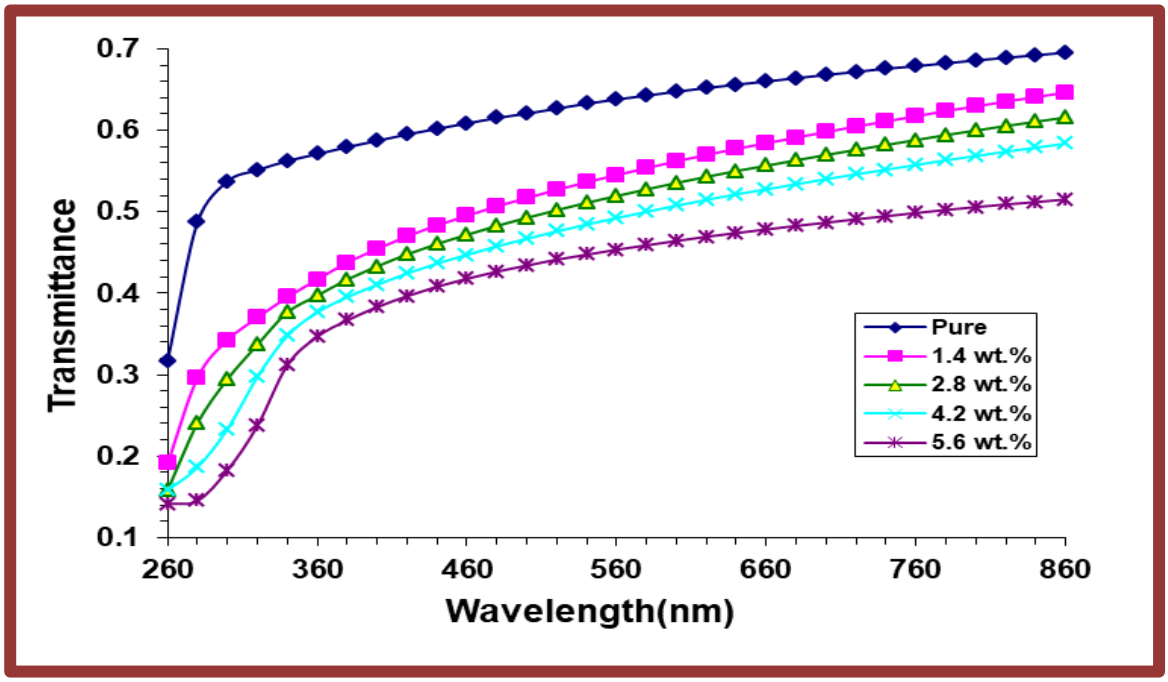

Figure (4.10) The transmittance versus wavelength of (PMMA-PC-In_2O_3-GO) composites at room temperature.

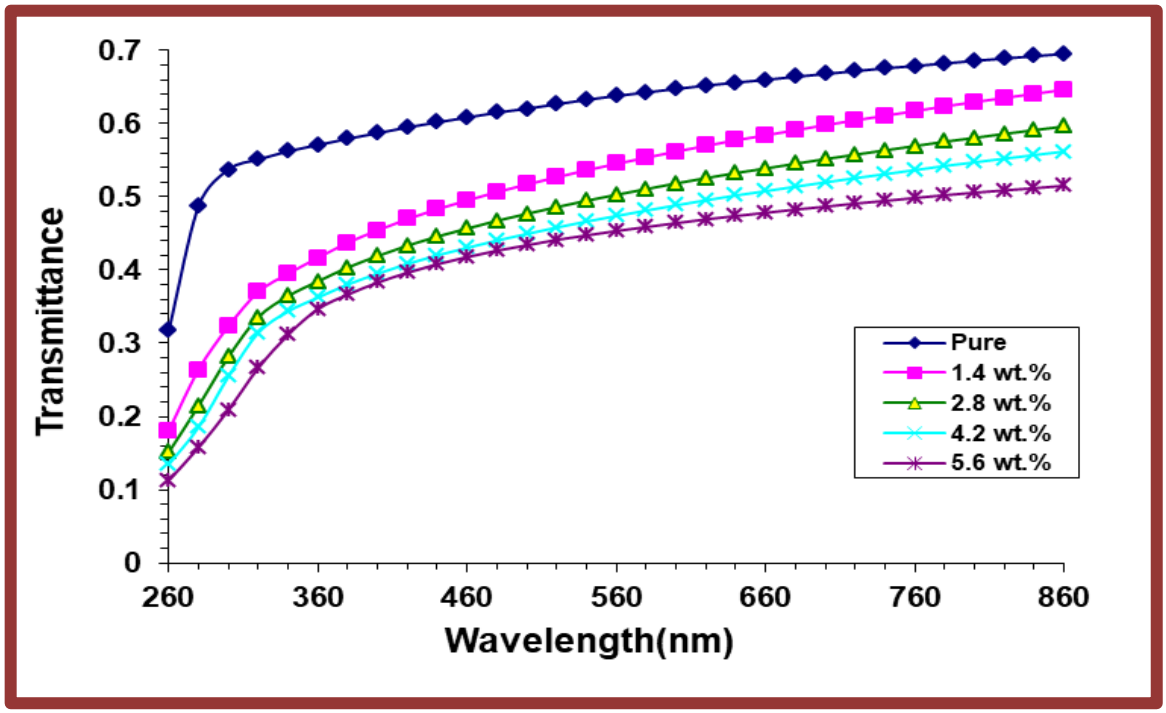

Figure (4.11) The transmittance versus wavelength of (PMMA-PC/Sb_2O_3-GO) composites at room temperature.

Table (4.1) Values of absorbance and transmittance for (PMMA-PC/In_2O_3-GO) Nanocomposites at λ = 560 nm.

Samples	Concentrations of In_2O_3-GO NPs wt.%	Absorbance	Transmittance
(PMMA-PC) Blend	0	0.652	0.637
(PMMA-PC/In_2O_3-GO) Nanocomposites	1.4	1.054	0.545
(PMMA-PC/In_2O_3-GO) Nanocomposites	2.8	1.138	0.517
(PMMA-PC/In_2O_3-GO) Nanocomposites	4.2	1.231	0.492
(PMMA-PC/In_2O_3-GO) Nanocomposites	5.6	2.121	0.353

Table (4.2) Values of absorbance and transmittance for (PMMA-PC/Sb_2O_3-GO) Nanocomposites at λ = 560 nm.

Samples	Concentrations of Sb_2O_3-GO NPs wt.%	Absorbance	Transmittance
(PMMA/PC) blend	0	0.781	0.637
(PMMA-PC/Sb_2O_3-GO) Nanocomposites	1.4	1.054	0.545
(PMMA-PC/Sb_2O_3-GO) Nanocomposites	2.8	1.096	0.532
(PMMA-PC/Sb_2O_3-GO) Nanocomposites	4.2	1.254	0.485
(PMMA-PC/Sb_2O_3-GO) Nanocomposites	5.6	2.054	0.321

4.3.3 The Absorption Coefficient of (PMMA-PC/In_2O_3-GO) and (PMMA-PC/Sb_2O_3-GO) Nanocomposites.

Figures (4-12) and (4.13) as show the absorption coefficient α as a function of wavelength for (PMMA-PC/In_2O_3-GO) and (PMMA-PC/Sb_2O_3-GO)nanocomposites.The absorption coefficient α is calculated by using equation (2.9). The absorption coefficient is lowest at high wavelength and low energy, indicating that there is no chance of an electron transfer since the incident photon's energy is insufficient to pass the electron from the valence band to the conduction band. Absorption is more excellent at higher energies, implying a greater potential for electron transitions. As a result, the energy of the incident photon is sufficient to transfer the electron from the valence band to the conduction band [125]. When the absorption coefficient is high ($>10^4$) cm^{-1} at high energies, the incident photon's energy is greater than the forbidden energy gap, indicating that the absorption coefficient aids in determining the

nature of the electron transition. Direct electron transitions are supposed to occur, with electrons and photons maintaining their energy and moment When the absorption coefficient is low (10^4 cm^{-1}) at low energies, it is expected that an indirect transition of electrons occurs, and the electronic momentum is maintained with the help of the phonon . Among other results is that the coefficient of absorption for the (PMMA-PC/In2O3-GO) and (PMMA-PC/Sb2O3-GO)nanocomposites is less than 10^4 cm^{-1} at all concentrations [126]. The values of absorbance coefficient for the prepared nanocomposites at λ=560 nm are listed in Tables (4.3) and (4.4), respectively.

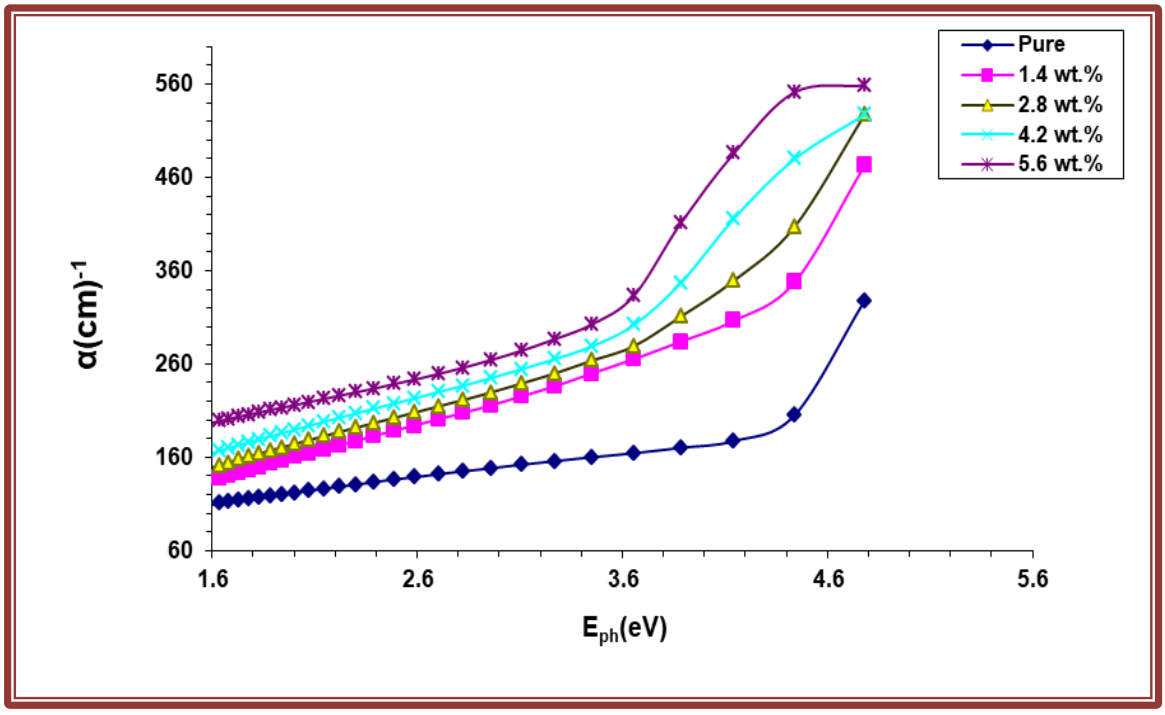

Figure (4.12): The absorption coefficient spectra as a function of wavelength of (PMMA-PC-In_2O_3-GO) nonocomposites at room temperature.

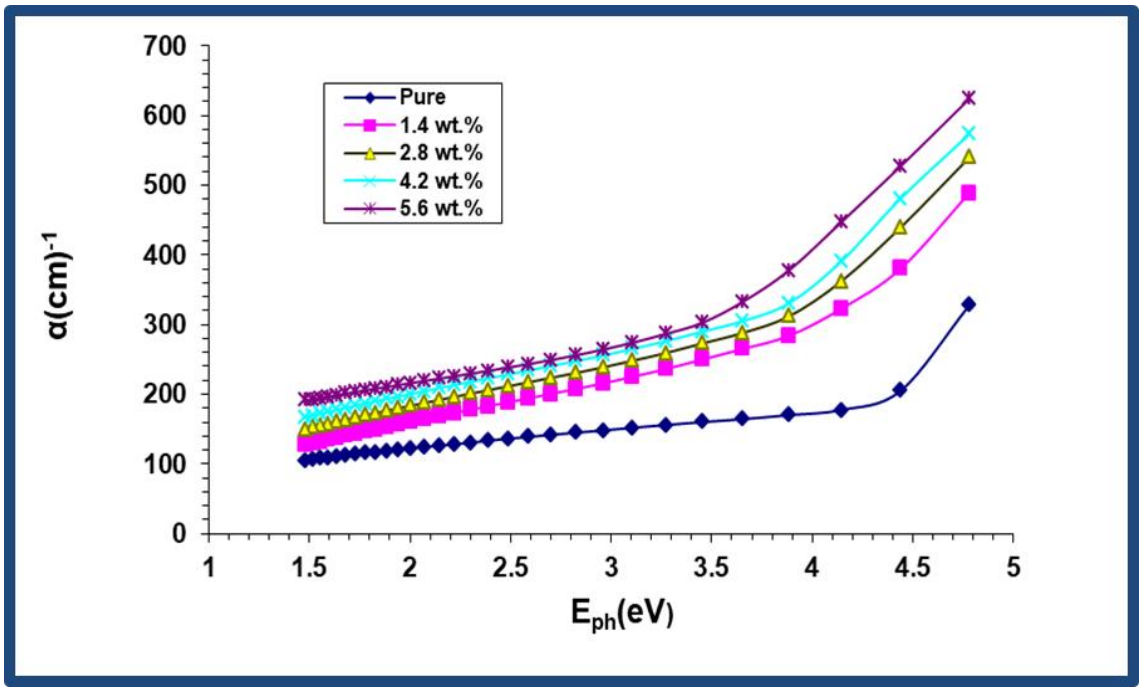

Figure (4.13) The absorption coefficient spectra as a function of wavelength of (PMMA-PC-Sb_2O_3-GO) nanocomposites at room temperature.

Table (4.3) The absorption coefficient of (PMMA-PC/In_2O_3-GO)nanocomposites at λ = 560 nm.

Samples	Concentrations of In_2O_3-GO NPs wt.%	Values for absorption coefficient (cm^{-1})
(PMMA-PC) blend	0	128.5
(PMMA-PC/In_2O_3-GO) Nanocomposites	1.4	162.3
(PMMA-PC/In_2O_3-GO) Nanocomposites	2.8	187.29
(PMMA-PC/In_2O_3-GO) Nanocomposites	4.2	202.3
(PMMA-PC/In_2O_3-GO) Nanocomposites	5.6	331.4

Table (4.4) The absorption coefficient of (PMMA-PC/Sb_2O_3-GO)nanocomposites at λ = 560 nm.

Samples	Concentrations of Sb_2O_3-GO NPs wt.%	Values for absorption coefficient (cm^{-1})
(PMMA-PC) blend	0	128.4
(PMMA-PC/Sb_2O_3-GO) Nanocomposites	1.4	173.3
(PMMA-PC/Sb_2O_3-GO) Nanocomposites	2.8	180.2
(PMMA-PC/Sb_2O_3-GO) Nanocomposites	4.2	206.3
(PMMA-PC/Sb_2O_3-GO) Nanocomposites	5.6	227.9

4.3.4 Energy Gap of (PMMA-PC/In_2O_3-GO) and (PMMA-PC/Sb_2O_3-GO) Nanocomposites.

The equation (2.3) is utilized to determine the optical energy gap values (Eg_{opt}) of nanocomposites. This is done by plotting $(\alpha h\nu)^{1/2}$ as a function of (E_{ph}) for all prepared nanocomposites, and finding the intersection with the x-axis to obtain the energy gap value. Figures (4.14) and (4.15) show the energy gaps for allowed indirect transitions of (PMMA-PC/In_2O_3-GO) and (PMMA-PC/Sb_2O_3-GO) nanocomposites, respectively, while figures (4.16) and (4.17) show the energy gaps for forbidden indirect transitions of (PMMA-PC/In_2O_3-GO) and (PMMA-PC/Sb_2O_3-GO) nanocomposites respectively [127]. The values obtained are presented in Tables (4.5)and (4.6). It is observed that the values of both allowed and forbidden indirect energy gaps for all prepared nanocomposites decrease with increasing concentrations of (In_2O_3, Sb_2O_3,GO

)nanoparticles [127]. At a concentration of 5.6% and λ=560, the energy gap of (PMMA-PC/In_2O_3-GO) and (PMMA-PC/Sb_2O_3-GO) nanocomposites decreased by approximately 51% and 48% for allowed indirect transitions, and about 77% and 80% for forbidden indirect transitions respectively. This behaviour makes the nanocomposites suitable for lightweight and low-cost electronics and optical devices. The gradual reduction in the energy gap values with increasing concentrations of nanoparticles may be due to the formation of localized levels in the energy gap. In this case, electron transitions occur in two stages: from the valence band to the localized levels in the energy gap and then from the localized levels to the conduction band [128].

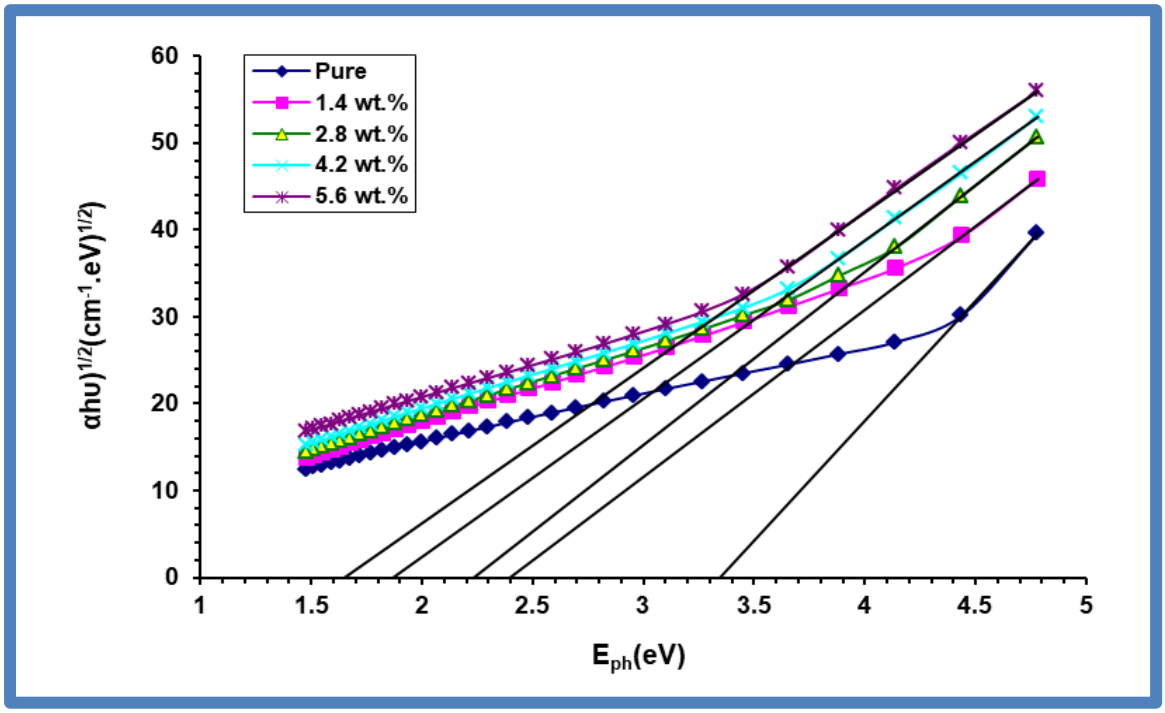

Figure (4.14) Variation of $(\alpha h\upsilon)^{1/2}$ for (PMMA-PC-In_2O_3-GO) nanocomposites with photon energy .

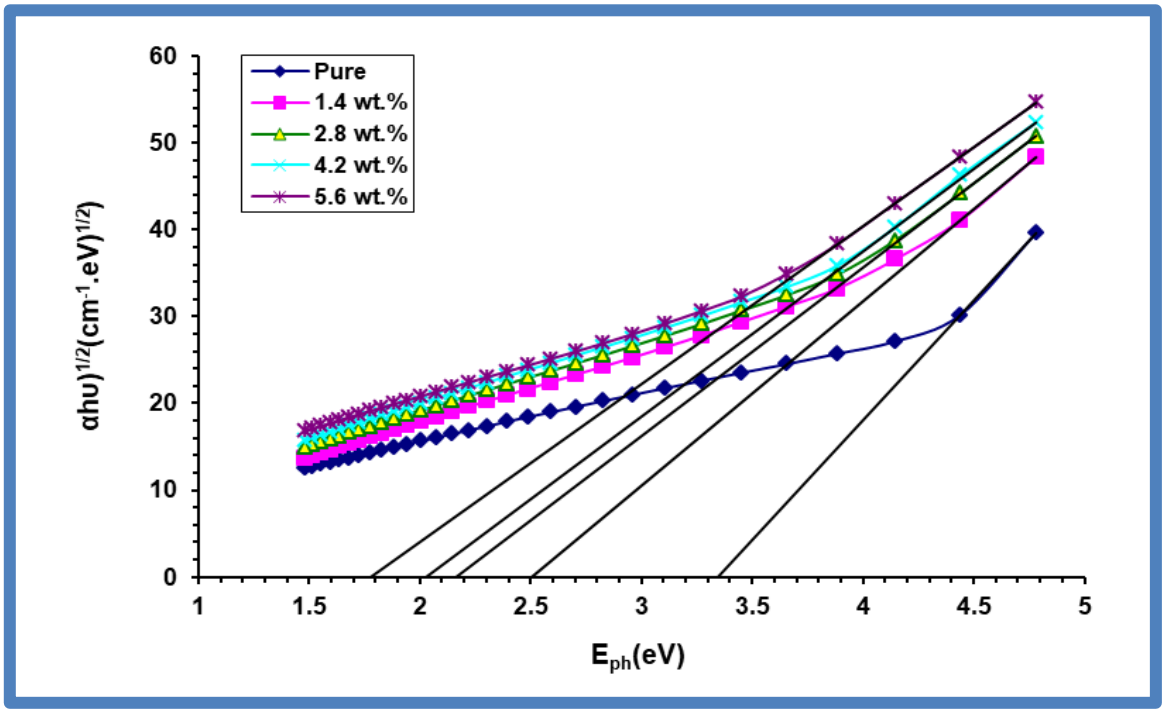

Figure (4.15) A plot of $(\alpha h\nu)^{1/2}$ versus photon energy (hν) of (PMMA-PC/Sb_2O_3-GO) nanocomposites at room temperature.

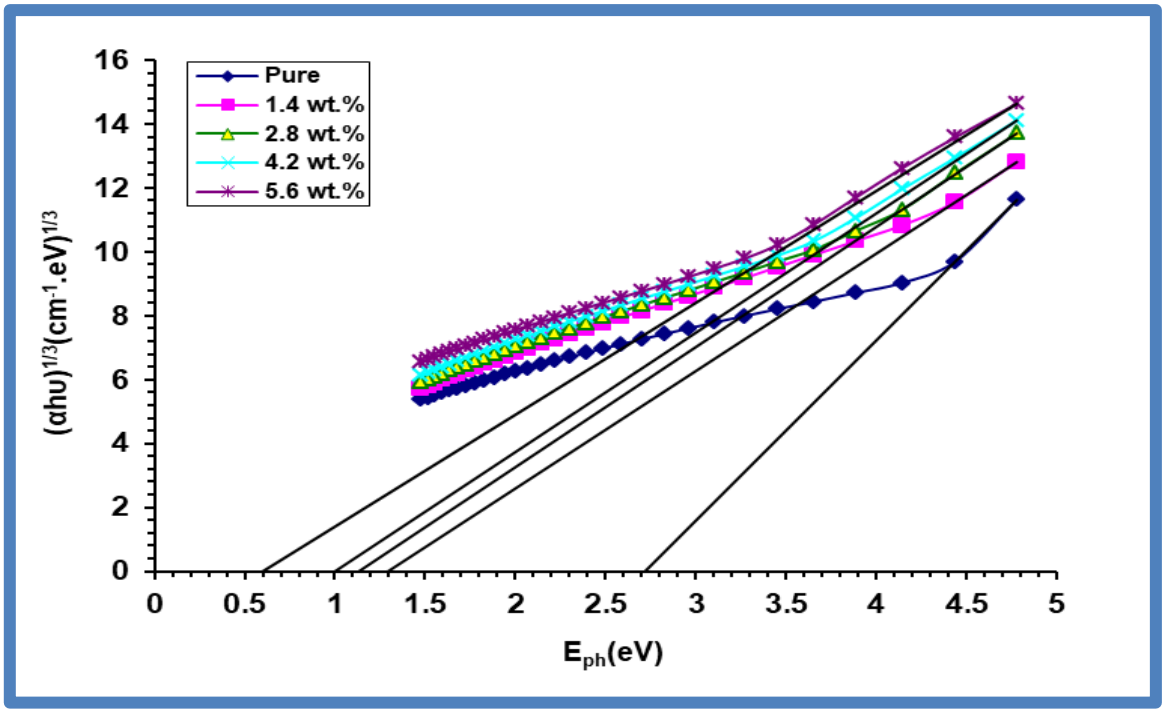

Figure (4.16) Variation of $(\alpha h\upsilon)^{1/3}$ for (PMMA-PC/In_2O_3-GO) nanocomposites with photon energy

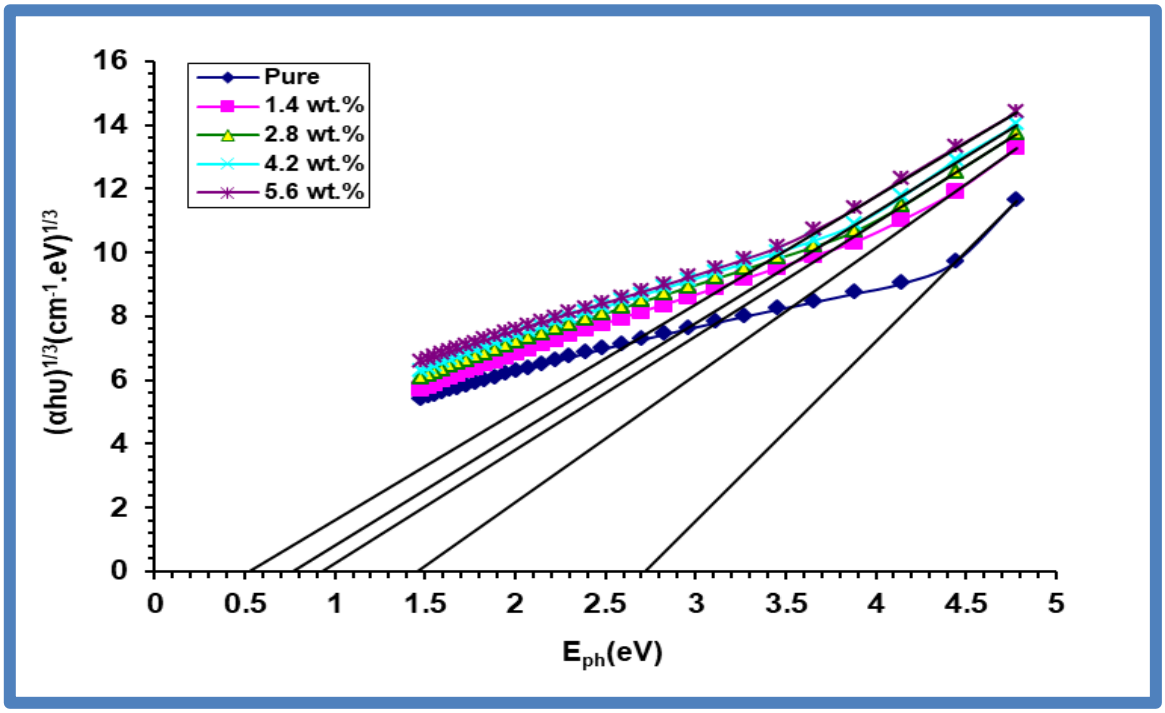

Figure (4.17) Variation of $(\alpha h\upsilon)^{1/3}$ for (PMMA-PC/Sb_2O_3-GO) nanocomposites with photon energy.

Table (4.5) Energy gap values at different (In_2O_3-GO) wt.%.

Sample	E_g (e V)/(Allowed)	E_g (e V)(Forbidden)
(PMMA-PC) blend	3.345	2.719
(PMMA-PC/In_2O_3-GO)	2.397	1.294
(PMMA-PC/In_2O_3-GO)	2.234	1.132
(PMMA-PC/In_2O_3-GO)	1.8690	1.100
(PMMA-PC/In_2O_3-GO)	1.650	0.6

Table (4.6) Energy gap values at different (Sb_2O_3-GO) wt.%.

Sample	E_g (e V)/(Allowed)	E_g (e V)(Forbidden)
(PMMA-PC) blend	3.345	2.719
(PMMA-PC/Sb_2O_3-GO) Nanocomposites	2.2505	1.456
(PMMA-PC/Sb_2O_3-GO) Nanocomposites	2.164	0.927
(PMMA-PC/Sb_2O_3-GO) Nanocomposites	2.028	0.765
(PMMA-PC/Sb_2O_3-GO) Nanocomposites	1.778	0.523

4.3.5 The Extinction Coefficient of (PMAA-PC/In_2O_3-GO) and (PMAA-PC/Sb_2O_3-GO) Nanocomposites.

The variance of the extinction coefficient for (PMMA-PC/In_2O_3-GO) and (PMMA-PC/Sb_2O_3-GO) nanocomposites is displayed in figures (4.18) and (4.19), respectively, as a function of wavelength (λ). These figures demonstrate that as the wavelength of incident light in the UV region increases, there is an increase in the extinction coefficient of (PMMA-PC/In_2O_3-GO) and (PMMA-PC/Sb_2O_3-GO) nanocomposites due to their high absorption in these regions [129]. Moreover, the extinction coefficient of the nanocomposites increases in the visible and near-infrared regions, which may be attributed to the nearly constant absorption coefficient of the nanocomposites in these regions. As a result, the extinction coefficient varies with the wavelength according to equation (2.12). The concentration of (In_2O_3, Sb_2O_3, GO) nanoparticles has a direct impact on the extinction coefficient of (PMMA-PC/In_2O_3-GO) and (PMMA-PC/Sb_2O_3-GO) nanocomposites, as it increases with higher

concentrations of (In_2O_3, Sb_2O_3 and GO) nanoparticles. This can be attributed to the increased absorption coefficient of the nanocomposites [130]. The ratio of the increase in extinction coefficient for (PMMA-PC/In_2O_3-GO) and (PMMA-PC/Sb_2O_3-GO)nanocomposites was 53% and 54%, respectively.

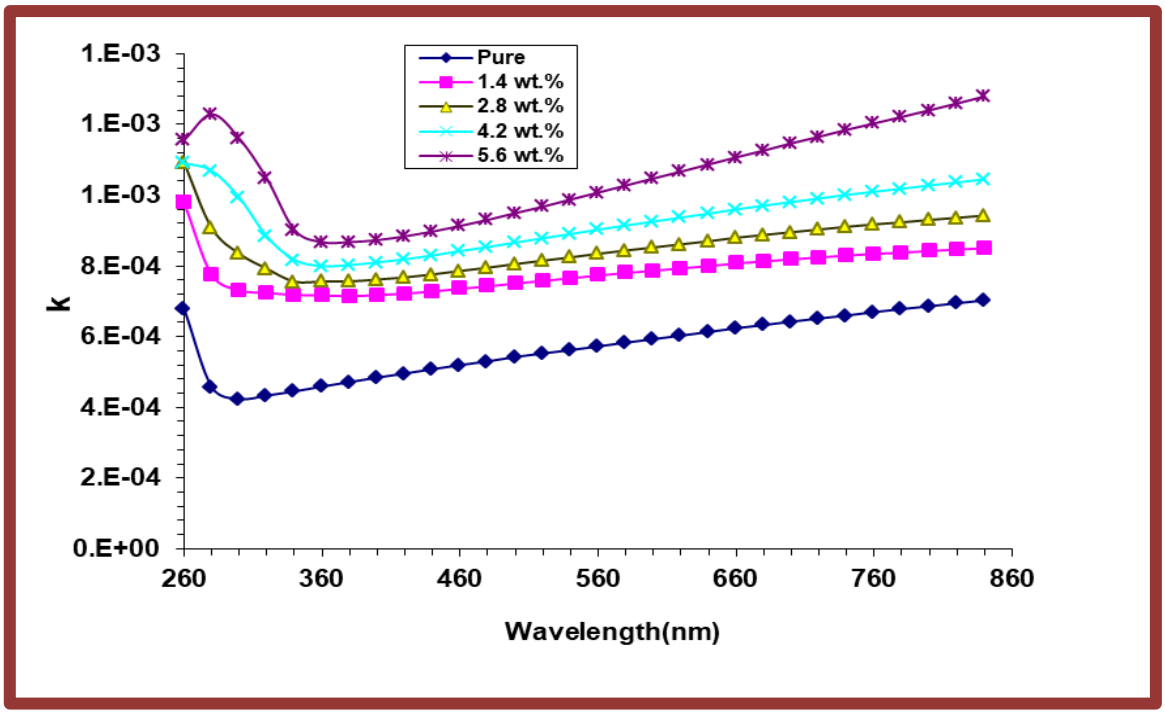

Figure (4.18) Variation of extinction coefficient for (PMMA-PC/In_2O_3-GO) nanocomposites with wavelength.

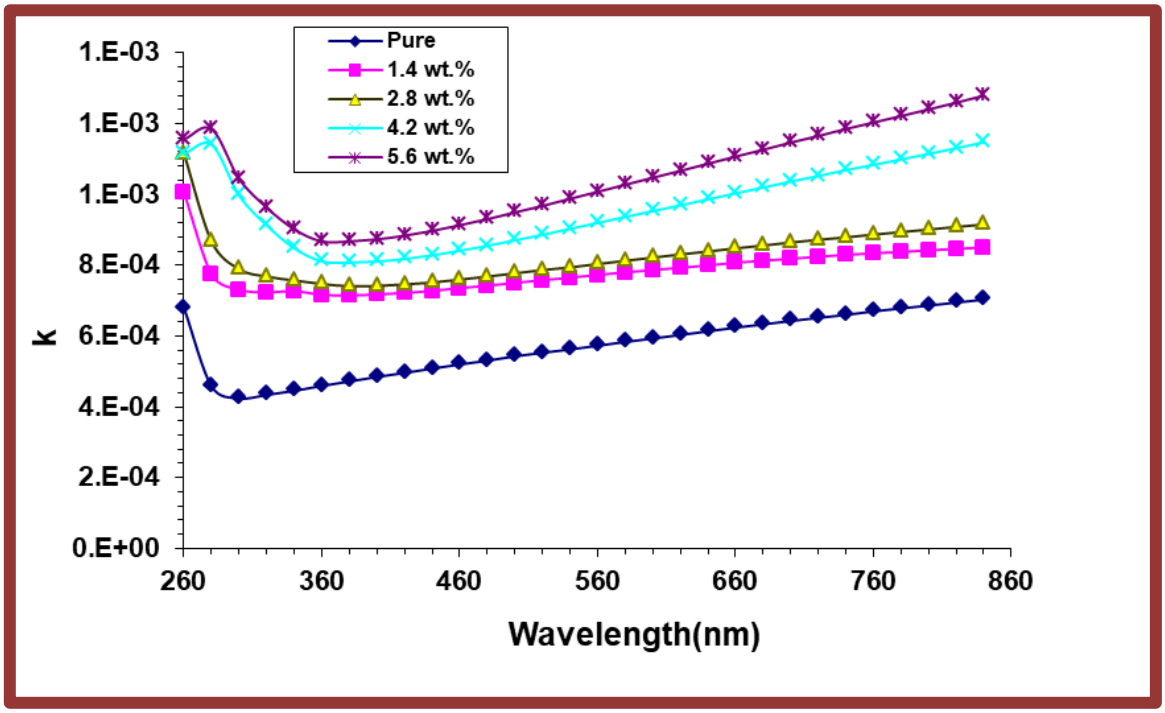

Figure (4.19) Variation of extinction coefficient for (PMMA-PC/Sb_2O_3-GO) Nanocomposites with wavelength.

4.3.6 The Refractive Index of (PMMA-PC/In_2O_3-GO) and (PMMA-PC/Sb_2O_3-GO) Nanocomposites.

Figures (4.20) and (4.21) shows the refractive index of (PMMA-PC/In_2O_3-GO) and (PMMA/PC-Sb_2O_3-GO) nanocomposites as a wavelength function. The graph illustrates how the refractive index of the nanocomposites varies with the wavelength of light.The results demonstrate that the refractive index increases with an increase in the weight percentages of the concentration of In_2O_3, Sb_2O_3 and GO nanoparticles.The ratio of refractive index for (PMMA-PC/In_2O_3-GO) and (PMMA-PC/Sb_2O_3-GO) nanocomposites was 25% and 22%, respectively. The observed increase in the refractive index can be attributed to the rise in the density of the nanocomposites. As the density of the nanocomposites increases, so does the refractive index. Furthermore, the graph shows that as the wavelength of light increases, the refractive index of the nanocomposites decreases [131]. This phenomenon can be explained by the fact

that the velocity of light decreases as the wavelength increases. As the velocity of light decreases, so does the refractive index. This relationship between wavelength and refractive index is well-established in optics and is known as the dispersion of refractive index [132].

The rise in the density of the nanocomposites is thought to be responsible for the observed increase in the refractive index. The addition of In_2O_3, Sb_2O_3 and GO nanoparticles to the polymer matrix increases the density of the nanocomposites. The increase in density causes a greater number of atoms and molecules to be present in the same volume, leading to a higher refractive index. The increase in refractive index can also be attributed to the high refractivity of the In_2O_3, Sb_2O_3 and GO nanoparticles [133]. When the incoming light interacts with a sample with a high refractivity in the ultraviolet range, the refractive index values tend to increase. The observed relationship between the refractive index and the concentration of In_2O_3, Sb_2O_3 and GO nanoparticles has important implications for the design and fabrication of novel nanocomposite materials with desirable optical properties. The ability to control the refractive index of nanocomposites through the addition of nanoparticles opens up the possibility of tailoring the optical properties of materials for specific applications. For example, by adjusting the concentration of In_2O_3, Sb_2O_3 and GO nanoparticles, it may be possible to develop nanocomposites with refractive indices that match those of other materials, which would enable the creation of materials with unique optical properties, such as invisibility cloaks[133] [134]. .In conclusion, Figures (4.20) and (4.21) presents important information regarding the refractive index of (PMMA-PC/In_2O_3-GO) and (PMMA-PC/Sb_2O_3-GO) nanocomposites.

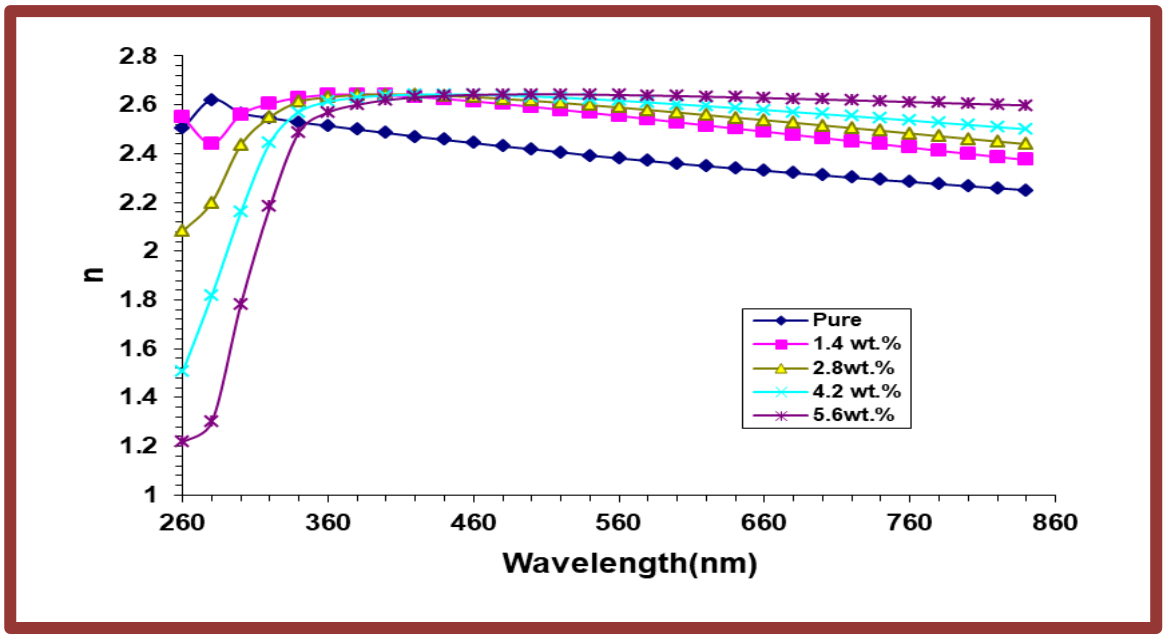

Figure (4.20) Variation of refractive index for (PMMA-PC/In_2O_3-GO) nanocomposites with wavelength.

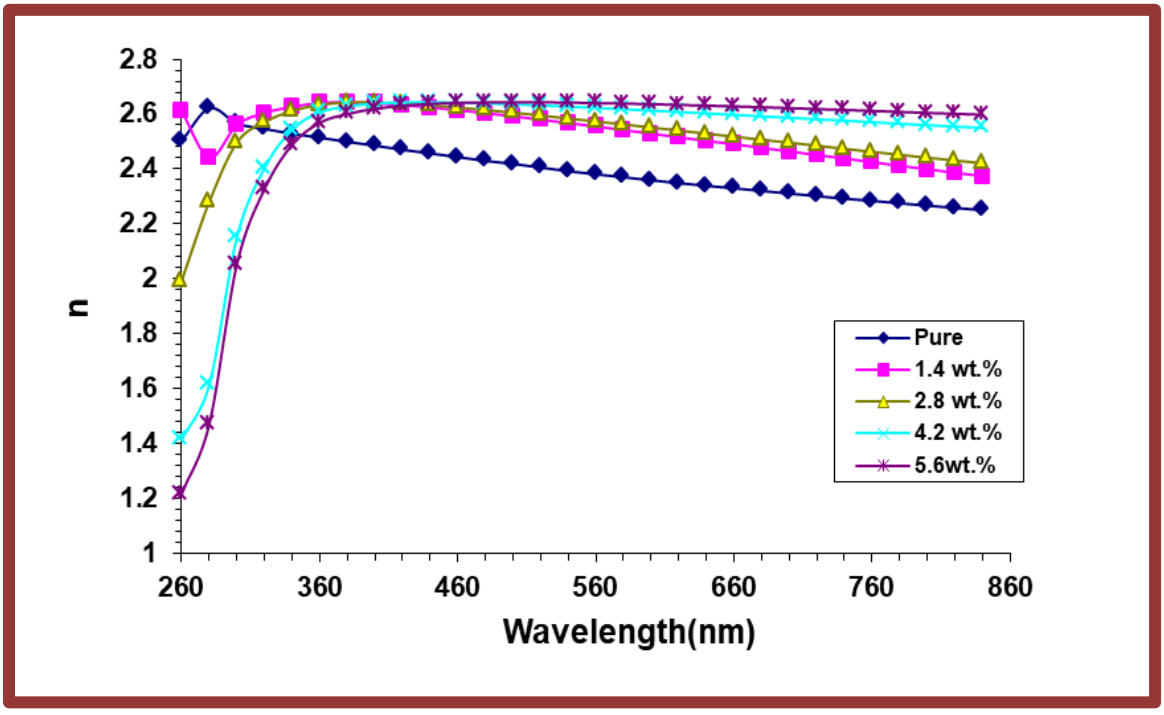

Figure (4.21) Variation of refractive index for (PMMA-PC/Sb_2O_3-GO) nanocomposites with wavelength.

4.3.7 The Real and Imaginary Parts of Dielectric Constant of (PMMA-PC/In_2O_3-GO) and (PMMA-PC/Sb_2O_3-GO) Nanocomposites

Figure (4.22) and (4.23) display the variation of the real part of dielectric constant (ε_1) with the wavelength for (PMMA-PC/In_2O_3-GO) and (PMMA-PC/Sb_2O_3-GO) nanocomposites, respectively. The behavior of the real part of the dielectric constant is similar to that of the refractive index (n), which means that the values of both parameters increase with increasing concentrations of In_2O_3,$Sb_2O_3$and GO nanoparticles [135]. This decrease can be attributed to the reduced scattering of the incident photon, which is caused by the increased density of the nanocomposites due to the presence of In_2O_3,$Sb_2O_3$and GO nanoparticles. The ratio of increase in the real part of the dielectric constant of the nanocomposites was found to be 33% and 29% for (PMMA-PC/In_2O_3-GO) and (PMMA-PC/Sb_2O_3-GO)nanocomposites, respectively. On the other hand, the imaginary part of the dielectric constant of the nanocomposites is essentially proportional to the extinction coefficient (k) values, which in turn is related to the absorption coefficient of the nanocomposites [136]. The effect of In_2O_3,$Sb_2O_3$and GO nanoparticles on the imaginary part of the dielectric constant (ε_1) is shown in figures (4.24) and (4.25) (PMMA-PC/In_2O_3-GO) and (PMMA-PC/Sb_2O_3-GO) nanocomposites, respectively. As shown in these figures, the imaginary part of the dielectric constant of the nanocomposites increases with increasing concentrations of In_2O_3,$Sb_2O_3$and GO nanoparticles. This increase can be attributed to the increased absorption coefficient of the nanocomposites, which in turn leads to an increase in the imaginary part of the dielectric constant. At a concentration of 5.6% of In_2O_3,$Sb_2O_3$and GO nanoparticles at a wavelength of 560, the imaginary part of the dielectric constant increased by about 57% and 50% for (PMMA-PC/In_2O_3-GO) and (PMMA-PC/Sb_2O_3-GO)nanocomposites, respectively.It is worth noting that the

values of optical constants, including refractive index, extinction coefficient, and dielectric constant, of the prepared nanocomposites at different wavelengths are shown in Tables (4.7) and (4.8). These Tables provide a comprehensive overview of the effect of the concentration of (In_2O_3, Sb_2O_3 and GO)nanoparticles on the optical properties of the nanocomposites. Moreover, the figures reveal that both the real and imaginary parts of the dielectric constant of the nanocomposites decrease with increasing wavelength of the incident photon [137]. This phenomenon can be explained by the fact that the real part of the dielectric constant is proportional to the refractive index, which increases with increasing wavelength in the ultraviolet range. On the other hand, the imaginary part of the dielectric constant depends on the extinction coefficient, which also increases with increasing wavelength. Therefore, the values of both parameters increase with increasing wavelength of the incident photon.In conclusion, the optical properties (PMMA-PC/In_2O_3-GO) and (PMMA-PC/Sb_2O_3-GO) nanocomposites were investigated by measuring the real and imaginary parts of the dielectric constant. The results indicate that the real part of the dielectric constant and refractive index decrease. The imaginary part of the dielectric constant and absorption coefficient increase with increasing concentrations of In_2O_3, $Sb_2O_3$and GO nanoparticles. Additionally, the values of both parameters increase with increasing wavelength of the incident photon. These findings provide valuable insights into designing and fabricating nanocomposites with tailored optical properties[138].

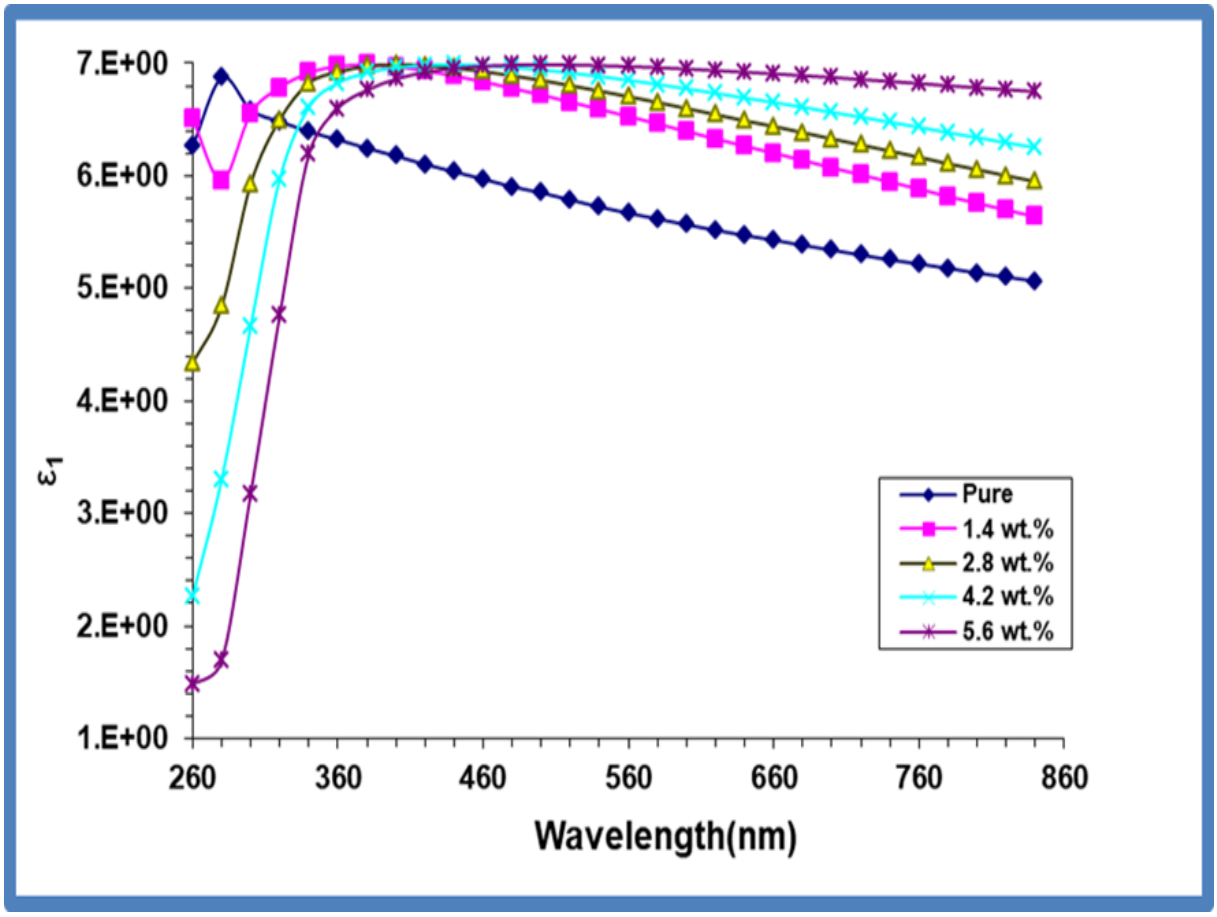

Figure (4.22) Variation of real part of dielectric constant for(PMMA-PC/In_2O_3-GO) nanocomposites with wavelength.

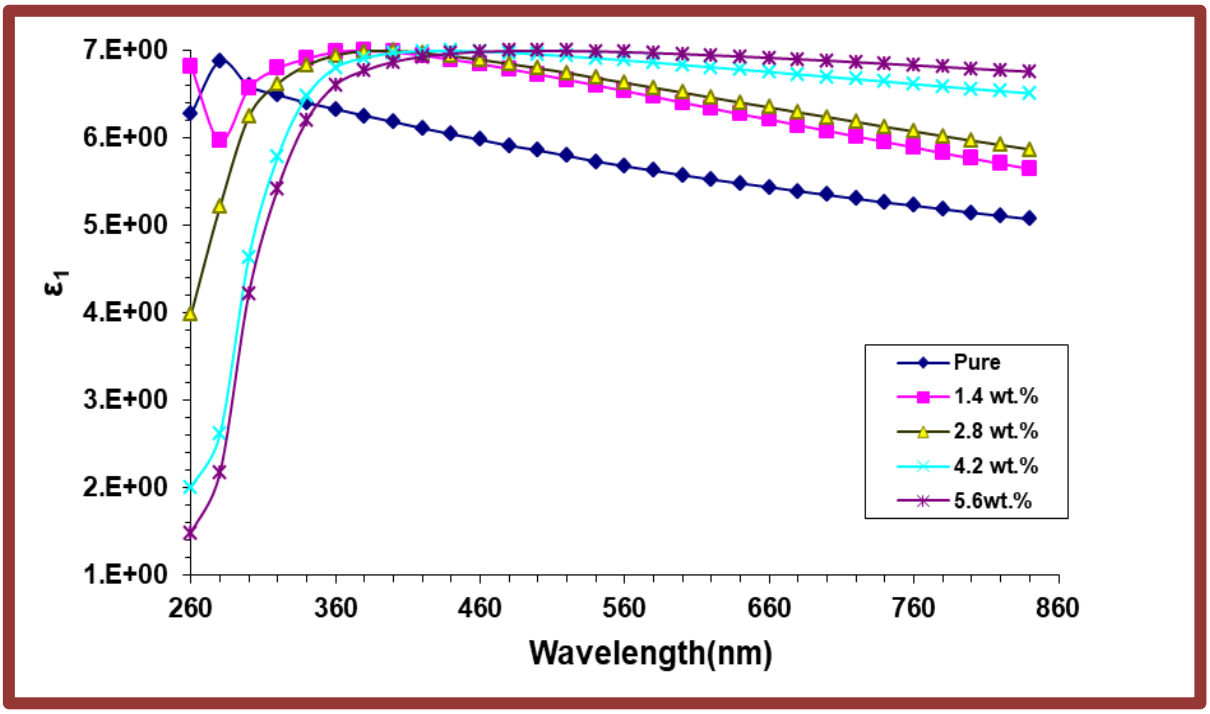

Figure (4.23) Variation of real part of dielectric constant for(PMMA-PC/Sb_2O_3-GO) Nanocomposites with wavelength.

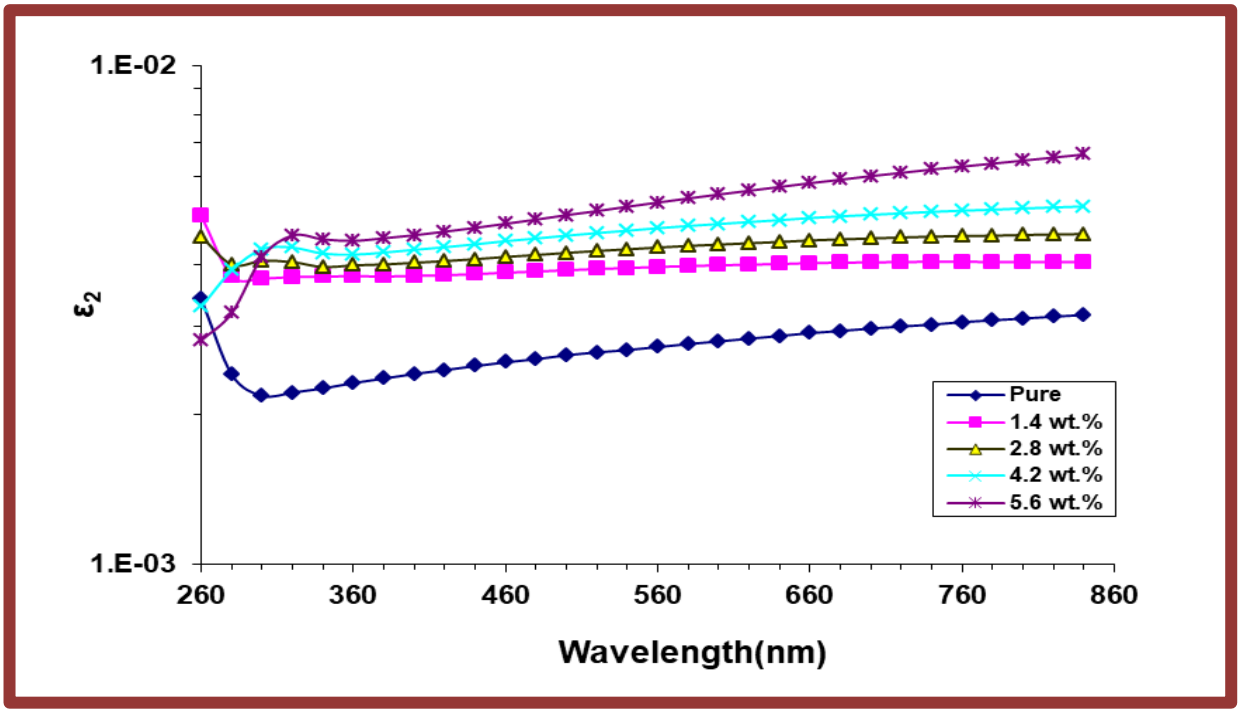

Figure (4.24) Variation of imaginary part of dielectric constant for (PMMA-PC-In_2O_3/GO)nanocomposites with wavelength.

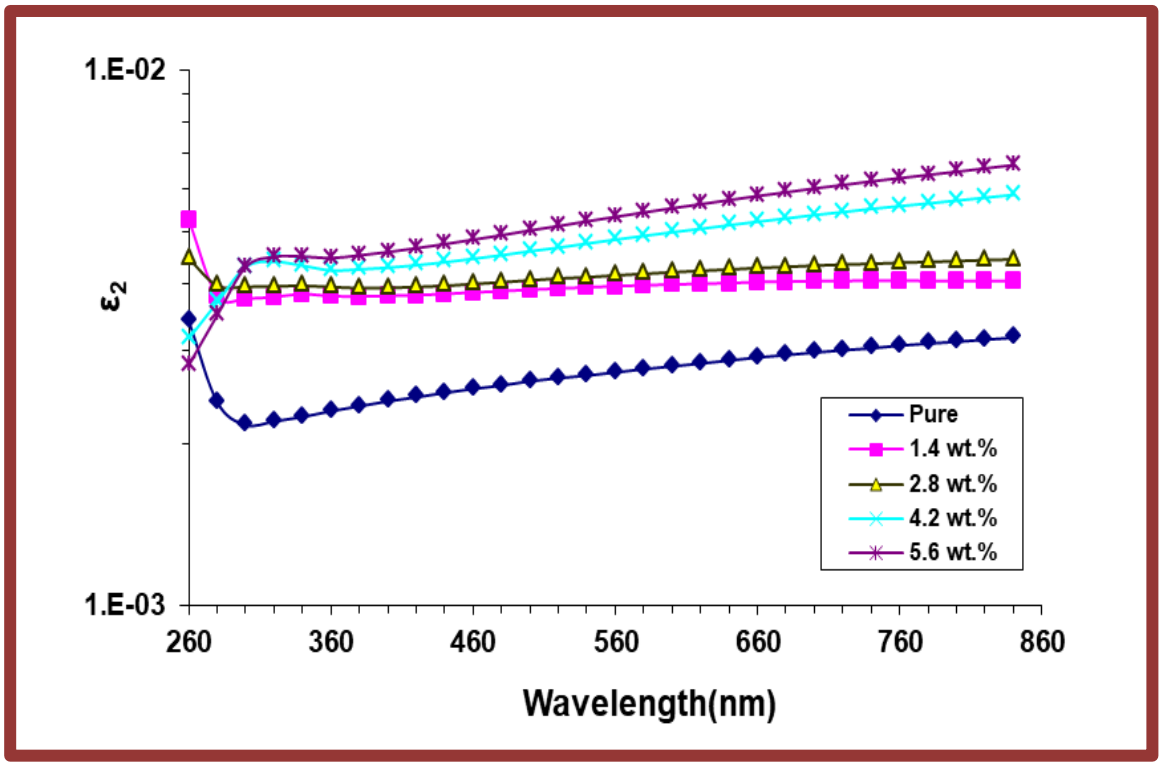

Figure (4.25) Variation of imaginary part of dielectric constant for (PMMA-PC/Sb_2O_3-GO) nanocomposites with wavelength.

Table (4.7) Values of optical constants for (PMMA-PC/In_2O_3-GO) nanocomposites at λ = 560 nm.

Samples	Concentrations of In_2O_3-GO NPs wt.%	n	k	ε_1	ε_2
(PMMA-PC) blend	0	2.21	0.00057	4.669	0.0027
(PMMA-PC/Sb_2O_3-GO) Nanocomposites	1.4	2.43	0.00077	6.529	0.0039
(PMMA-PC/Sb_2O_3-GO) Nanocomposites	2.8	2.57	0.00080	6.623	0.0041
(PMMA-PC/Sb_2O_3-GO) Nanocomposites	4.2	2.62	0.00092	6.879	0.0048
(PMMA-PC-Sb_2O_3-GO) Nanocomposites	5.6	2.84	0.00150	6.907	0.0064

Table (4.8) Values of optical constants (PMMA-PC/Sb_2O_3-GO) Nanocomposites at λ = 560.

Samples	Concentrations of Sb_2O_3-GO NPs wt.%	n	k	ε_1	ε_2
(PMMA-PC) blend	0	2.32	0.00065	5.122	0.0027
(PMMA-PC/Sb_2O_3-GO) Nanocomposites	1.4	2.55	0.00084	6.529	0.004
(PMMA-PC/Sb_2O_3-GO) Nanocomposites	2.8	2.58	0.00082	6.706	0.0043
(PMMA-PC-Sb_2O_3-GO) Nanocomposites	4.2	2.61	0.00097	6.851	0.0047
(PMMA-PC-Sb_2O_3-GO) Nanocomposites	5.6	2.94	0.0014	7.101	0.0056

4.3.8 The Optical Conductivity of (PMMA-PC/In_2O_3-GO) and (PMMA-PC/Sb_2O_3-GO) Nanocomposites.

The study of a material's optical response is primarily focused on its optical conductivity. The (PMMA-PC/In_2O_3-GO) and (PMMA-PC/Sb_2O_3-GO) were investigated for their optical conductivity as a function of wavelength, as shown in figures (4.26) and (4.27). The results indicate that the optical conductivity of both nanocomposites increases with an increasing concentration of In_2O_3, Sb_2O_3 and GO nanoparticles [139]. This is attributed to the formation of localized levels in the energy gap, which leads to an increase in the absorption coefficient and therefore the optical conductivity of the nanocomposite [140].At a wavelength of 560 nm , the optical conductivity of the nanocomposites increased by about 48% and 50%, respectively, when the

concentration of $In_2O_{3,}Sb_2O_3$and GO nanoparticles reached 5.6%. The optical conductivity of the nanocomposites decreases as the wavelength of the incident photon increases, as the optical conductivity strongly depends on the wavelength of the incident photon.The nanocomposites show high values of optical conductivity in the UV region, with an increase of optical conductivity at low wavelengths due to the high absorption of the nanocomposite in that region and an increase in charge transfer excitations.The optical conductivity spectrum shows that the nanocomposites are transmittance in the visible and near-infrared regions[141]. Tables (4.9) and (4.10) display the values of optical conductivity for the prepared nanocomposites at a wavelength of 560 nm**.**

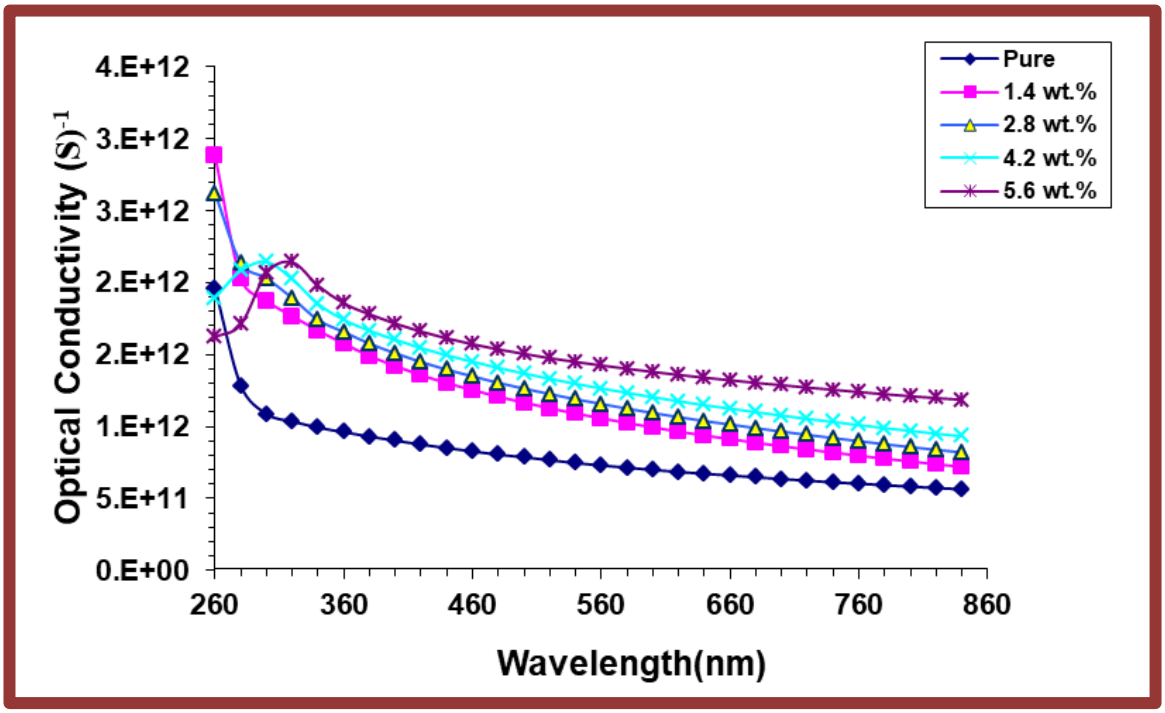

Figure (4.26): Variation of optical conductivity for (PMMA-PC/In_2O_3-GO) nanocomposites with wavelength

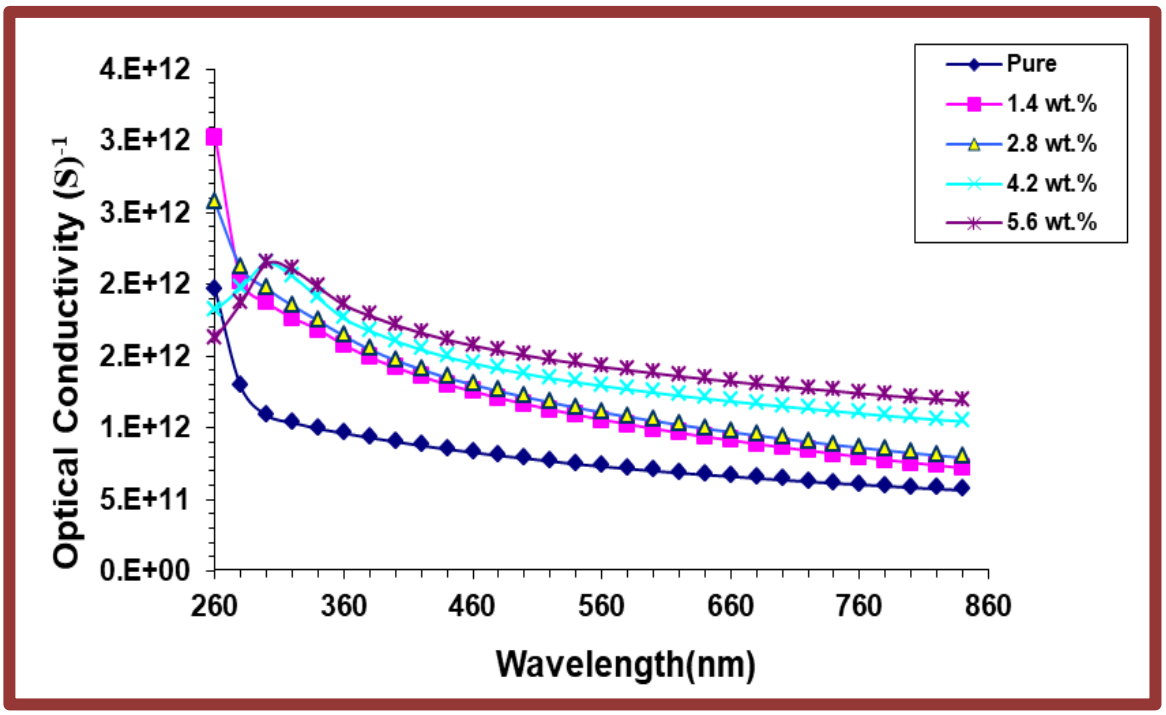

Figure (4.27) Variation of optical conductivity for (PMMA-PC/Sb_2O_3-GO) Nanocomposites with wavelength.

Table (4.9) The optical conductivity values of (PMMA-PC/In_2O_3-GO) Nanocomposites at λ = 560 nm.

Samples	Concentrations of $In_2O_3$and GO NPs wt.%	Optical conductivity $(\Omega.cm)^{-1}$
(PMMA-PC) Blend	0	7.3×10^{11}
(PMMA-PC/In_2O_3-GO) Nanocomposites	1.4	10.5×10^{11}
(PMMA-PC/Sb_2O_3-GO) Nanocomposites	2.8	11.5×10^{11}
(PMMA-PC/In_2O_3-GO) Nanocomposites	4.2	12.6×10^{11}
(PMMA-PC/In_2O_3-GO) Nanocomposites	5.6	14.2×10^{11}

Table (4.10) The optical conductivity values of (PMMA-PC/Sb_2O_3-GO) Nanocomposites at λ = 560 nm.

Samples	Concentrations of Sb_2O_3- GO NPs wt.%	Optical conductivity $(\Omega.cm)^{-1}$
(PMMA-PC) blend	0	7.11×10^{11}
(PMMA-PC/Sb_2O_3-GO) Nanocomposites	1.4	10.6×10^{11}
(PMMA-PC/Sb_2O_3-GO) Nanocomposites	2.8	11.1×10^{11}
(PMMA-PC/Sb_2O_3-GO) Nanocomposites	4.2	12.9×10^{11}
(PMMA-PC/ Sb_2O_3-GO) Nanocomposites	5.6	14.3×10^{11}

4.4 The A.C Electrical Properties of (PMMA-PC/In_2O_3-GO) and (PMMA-PC/Sb_2O_3-GO) Nanocomposites

The A.C electrical properties of (PMMA-PC/In_2O_3-GO) and (PMMA-PC/Sb_2O_3-GO) nanocomposites are involved dielectric constant, dielectric loss and A.C electrical conductivity were studied in frequency rang (100-5×10^6) Hz at room temperature.

4. 4. 1 The Dielectric Constant of (PMMA-PC/In_2O_3-GO) and (PMMA-PC/Sb_2O_3-GO) Nanocomposites.

The figures (4.28) and (4.29) illustrate the impact of In_2O_3,$Sb_2O_3$and GO nanoparticle concentrations on the dielectric constant of (PMMA-PC/In_2O_3-GO) and (PMMA-PC/Sb_2O_3-GO) nanocomposites, respectively, at 100Hz. The

dielectric constant can be determined using equation (2.14). The figures indicate that the dielectric constant of (PMMA-PC/In_2O_3-GO) and (PMMA-PC/Sb_2O_3-GO) nanocomposites increases as the concentration of In_2O_3, Sb_2O_3 and GO nanoparticles increases [142], as indicated in Tables (4.11) and (4.12), respectively. This behavior can be attributed to interfacial polarization within the nanocomposites in the applied alternating electric field and the increase in charge carriers [143].The dielectric constant of (PMMA-PC/In_2O_3-GO) and (PMMA-PC/Sb_2O_3-GO) nanocomposites is higher at 5.6wt% of In_2O_3,$Sb_2O_3$and GO nanoparticle concentration due to the high dielectric constant value of In_2O_3,$Sb_2O_3$and GO nanoparticles. This finding is in agreement with previous studied. Figures (4.30) and (4.31) present the variation of the dielectric constant of (PMMA-PC/In_2O_3-GO) and (PMMA-PC/Sb_2O_3-GO)nanocomposites with frequency, respectively [144]. As depicted in the figures, the dielectric constant of all prepared nanocomposites decreases with increase in the frequency of the applied electric field. This can be explained by the tendency of dipoles in the nanocomposite samples to orient themselves in the direction of the applied electric field and the reduction in space charge polarization to the total polarization [145].

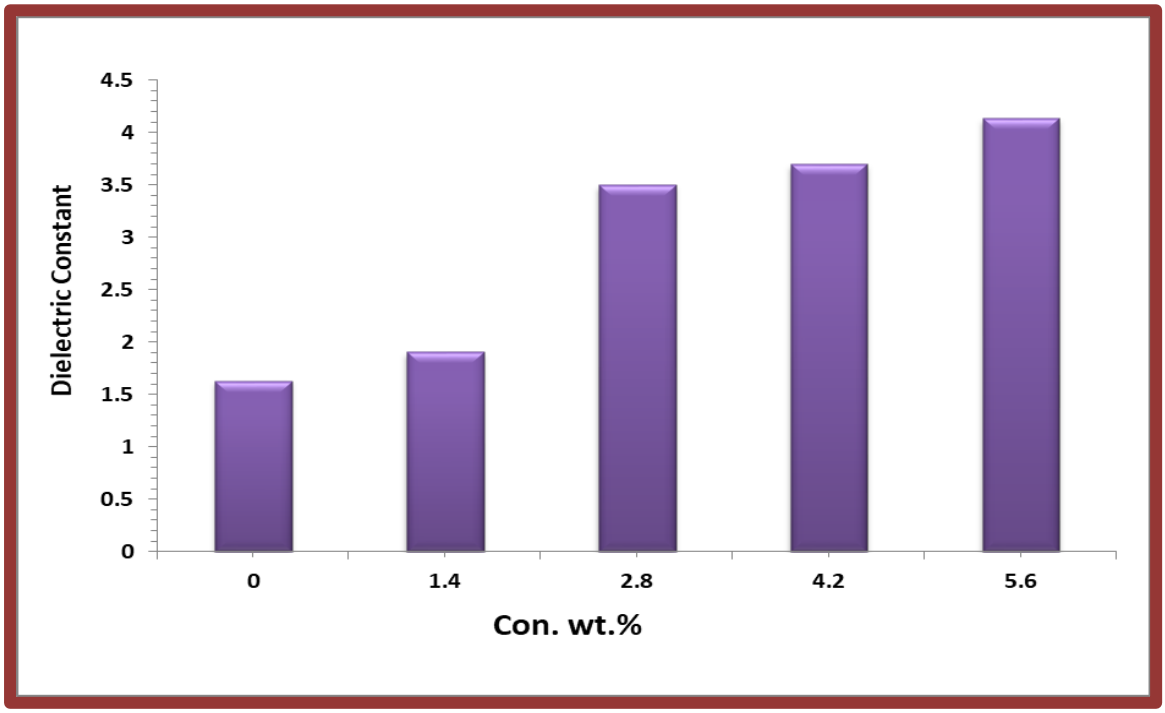

Figure (4.28) Effect of (In_2O_3 -GO)concentrations on dielectric constant for (PMMA-PC) blend at 100Hz

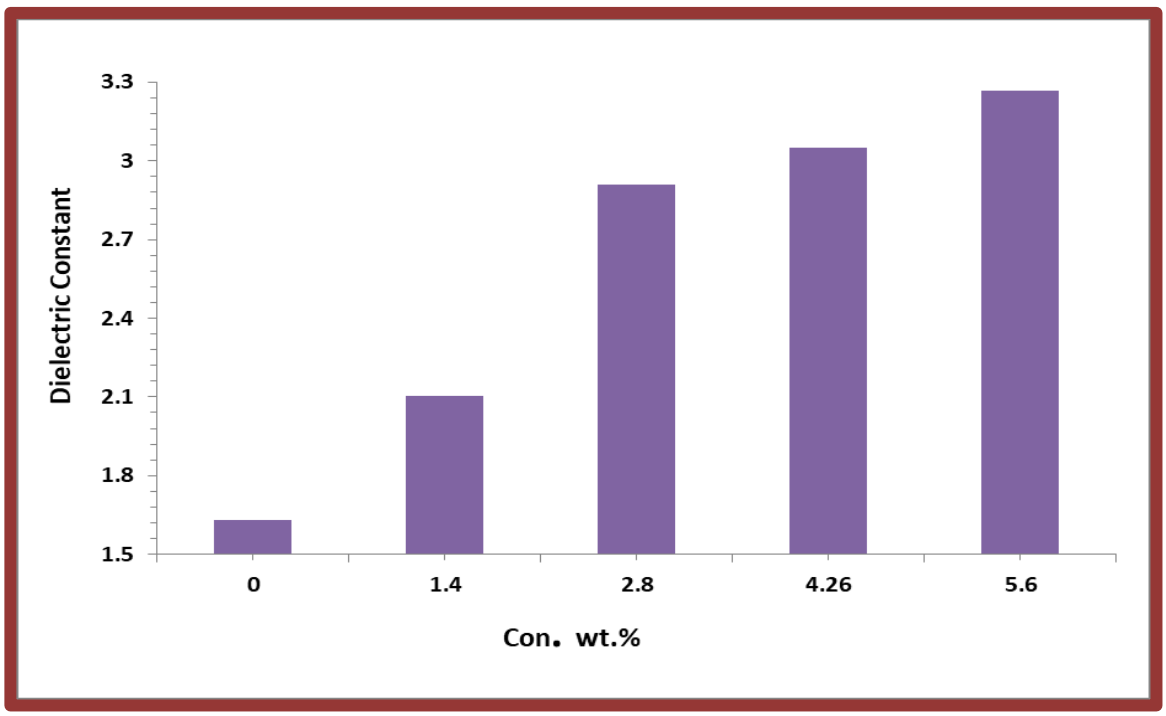

Figure (4.29) Effect of (Sb_2O_3 -GO)concentrations on dielectric constant for(PMMA-PC) blend at 100Hz

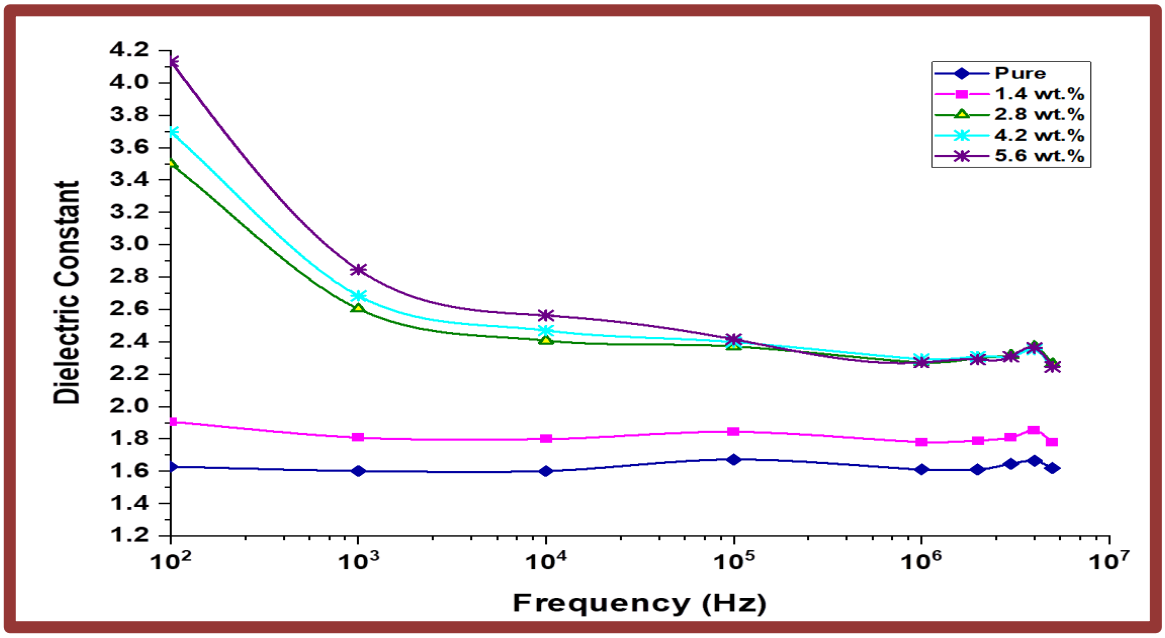

Figure (4.30) Variation of dielectric constants for (PMMA -PC/In_2O_3-GO) Nanocomposites with frequency at room temperature

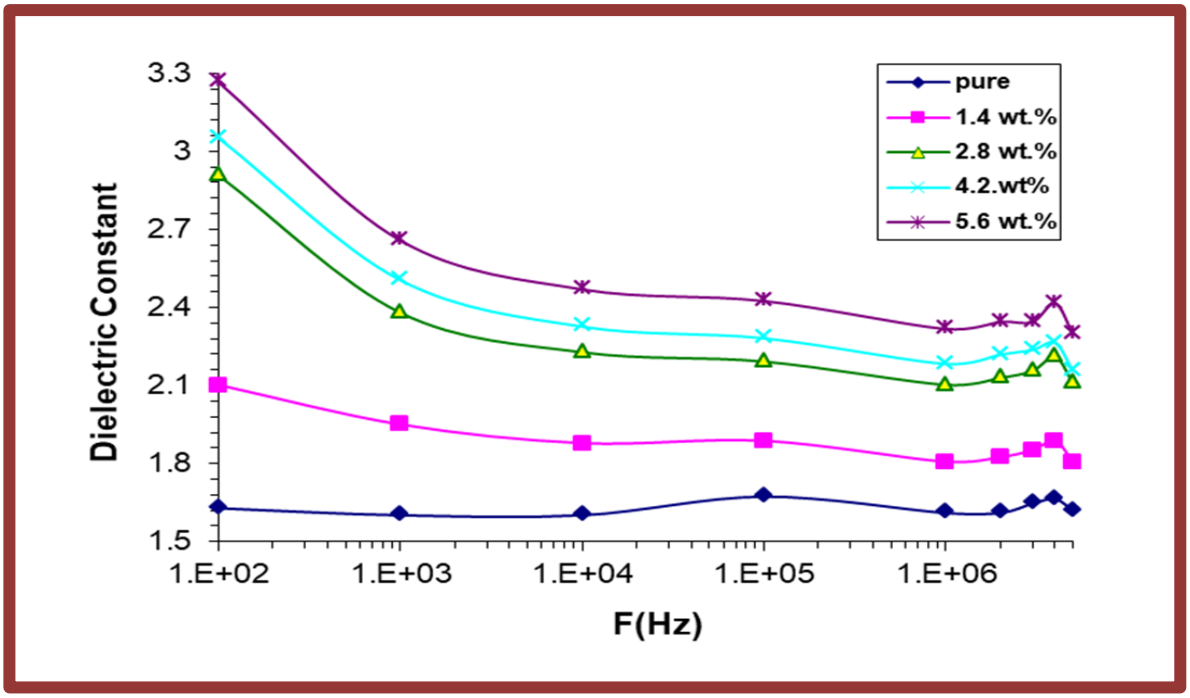

Figure (4.31) Variation of dielectric constants for (PMMA -PC/Sb_2O_3-GO nanocomposites with frequency at room temperature.

Tables (4.11) Values of dielectric constant for ((PMMA-PC/In_2O_3-GO) Nanocomposites at 100 Hz.

Samples	Concentrations of In_2O_3-GO NPs wt.%	Electrical dielectric constant
(PMMA-PC/In_2O_3-GO) Nanocomposites	0	1.63
(PMMA-PC/In_2O_3-GO) Nanocomposites	1.4	1.905
(PMMA-PC/In_2O_3-GO) Nanocomposites	2.8	3.498
(PMMA-PC/In_2O_3-GO) Nanocomposites	4.2	3.695
(PMMA-PC/In_2O_3-GO) Nanocomposites	5.6	4.134

Tables (4.12) Values of dielectric constant for (PMMA-PC/Sb_2O_3-GO) Nanocomposites at 100 Hz.

Samples	Concentrations of Sb_2O_3-GO NPs wt.%	Electrical dielectric constant
(PMMA-PC) blend	0	1.630
(PMMA-PC/Sb_2O_3-GO) Nanocomposites	1.4	2.102
(PMMA-PC/Sb_2O_3-GO) Nanocomposites	2.8	2.908
(PMMA-PC/Sb_2O_3-GO) Nanocomposites	4.2	3.051
(PMMA-PC/Sb_2O_3-GO) Nanocomposites	5.6	3.266

4.4.2 The Dielectric Loss of (PMMA-PC/In_2O_3-GO) and (PMMA-PC/Sb_2O_3-GO) Nanocomposites.

Figures (4.32) and (4.33) display how the concentration of In_2O_3, $Sb_2O_3$and GO nanoparticles affects the dielectric loss of (PMMA-PC/In_2O_3-GO) and (PMMA-PC/Sb_2O_3-GO)nanocomposites at 100Hz. The dielectric loss of these nanocomposites can be measured using equation (2-25). The figures reveal that the dielectric loss increases with the concentration of In_2O_3, $Sb_2O_3$and GO nanoparticles, as depicted in Tables (4.13) and (4.14). The rise in the dielectric loss for (PMMA-PC/In_2O_3-GO) and (PMMA-PC/Sb_2O_3-GO)nanocomposites with increasing of In_2O_3, $Sb_2O_3$and GO nanoparticle concentration is due to an increase in the number of charge carriers for (PMMA-PC/In_2O_3-GO) and (PMMA-PC/Sb_2O_3-GO) nanocomposites. At low concentrations, nanoparticles cluster together, but when In_2O_3, $Sb_2O_3$and GO nanoparticle concentration exceeds 5.6 wt.%, they form a path network in the nanocomposites. Figures (4.34) and (4.35) illustrate how the dielectric loss of (PMMA-PC/In_2O_3-GO) and (PMMA-PC/Sb_2O_3-GO) nanocomposites varies with frequency [146]. For all prepared nanocomposites, the dielectric loss decreases as the frequency of the applied electric field increases. This decrease in dielectric loss with increasing frequency is due to the reduced contribution of space charge polarization. At lower frequencies, the dielectric loss for (PMMA-PC/In_2O_3-GO) and (PMMA-PC/Sb_2O_3-GO) nanocomposites is high, because the electric dipoles have sufficient time to align with the applied electric field before it changes direction [147].

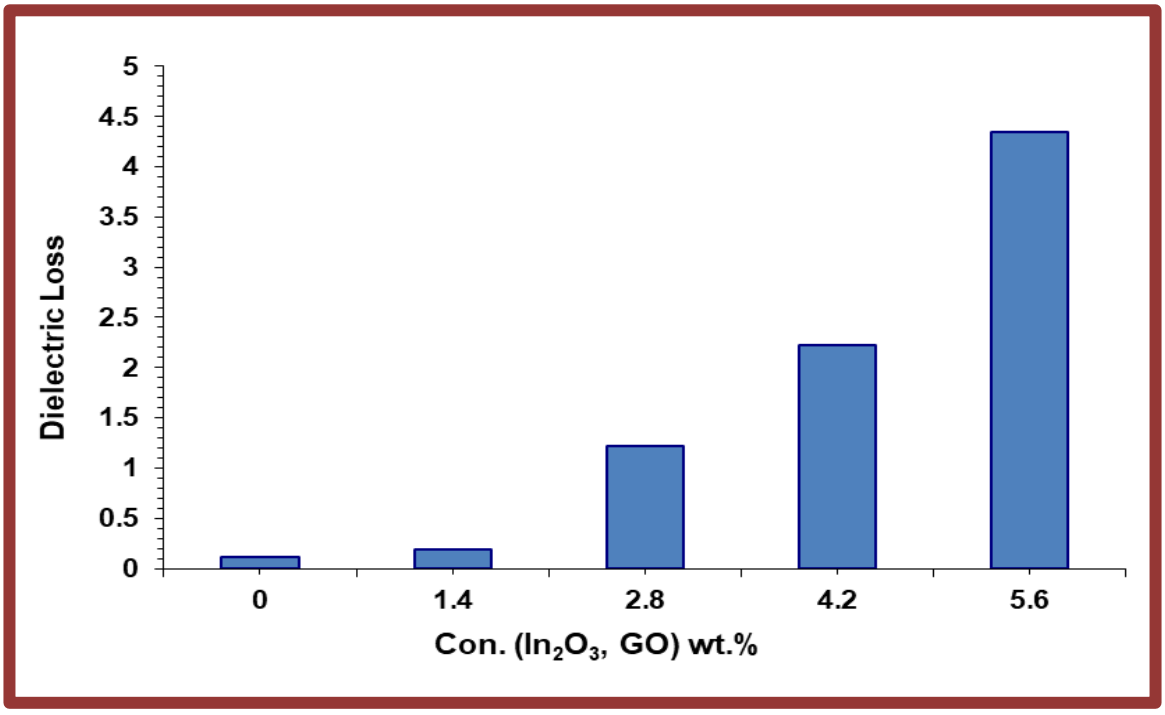

Figure (4.32): Effect of(In_2O_3 - GO) NPs concentrations on dielectric loss for (PMMA- PC) blend at 100Hz.

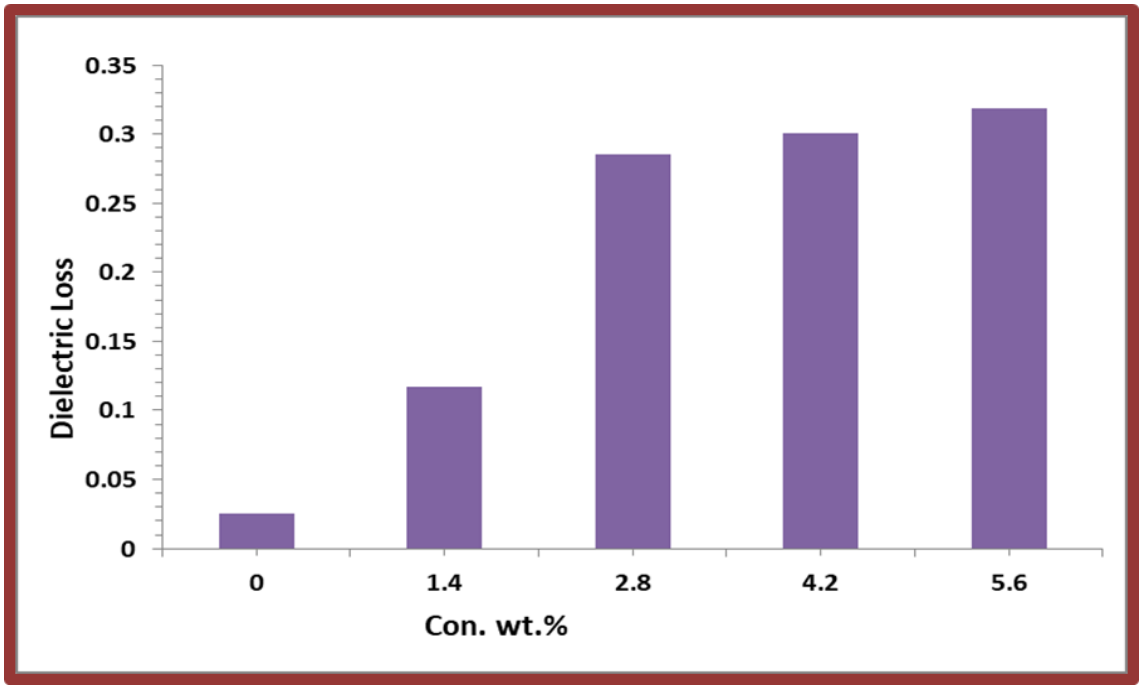

Figure (4.33) Effect of(Sb_2O_3 - GO) NPs concentrations on dielectric loss for (PMMA-PC) blend at 100Hz

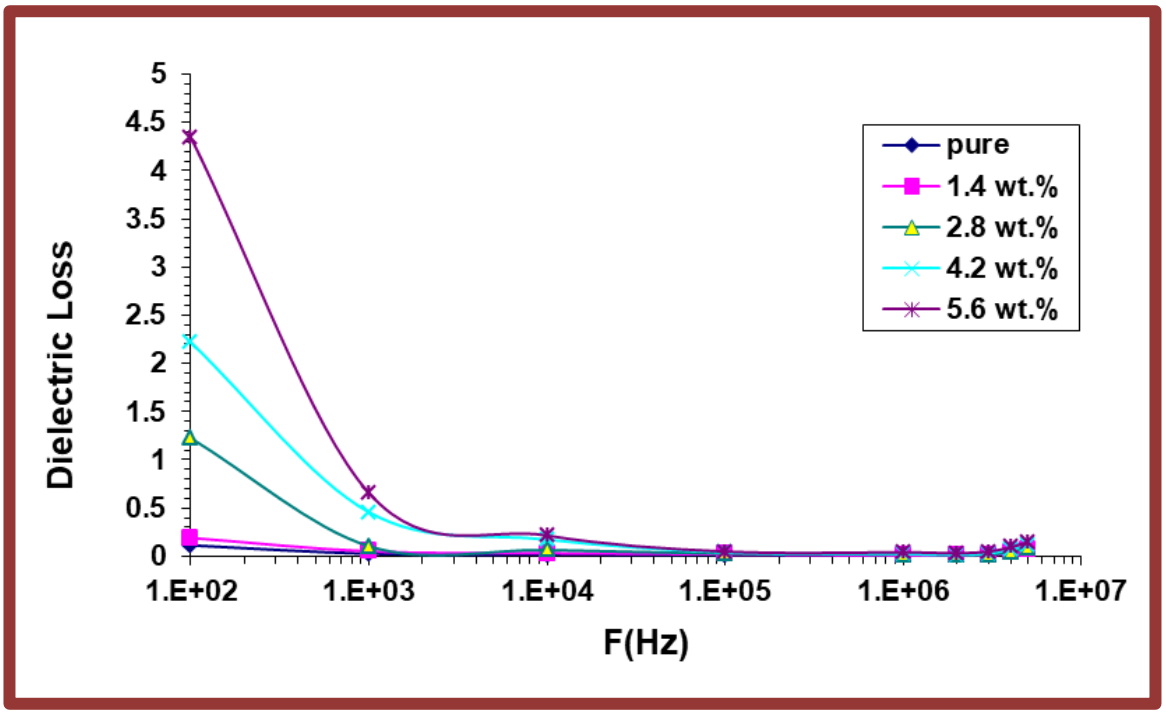

Figure (4.34) Variation of dielectric loss for (PMMA -PC/In_2O_3-GO) Nanocomposites with frequency at room temperature.

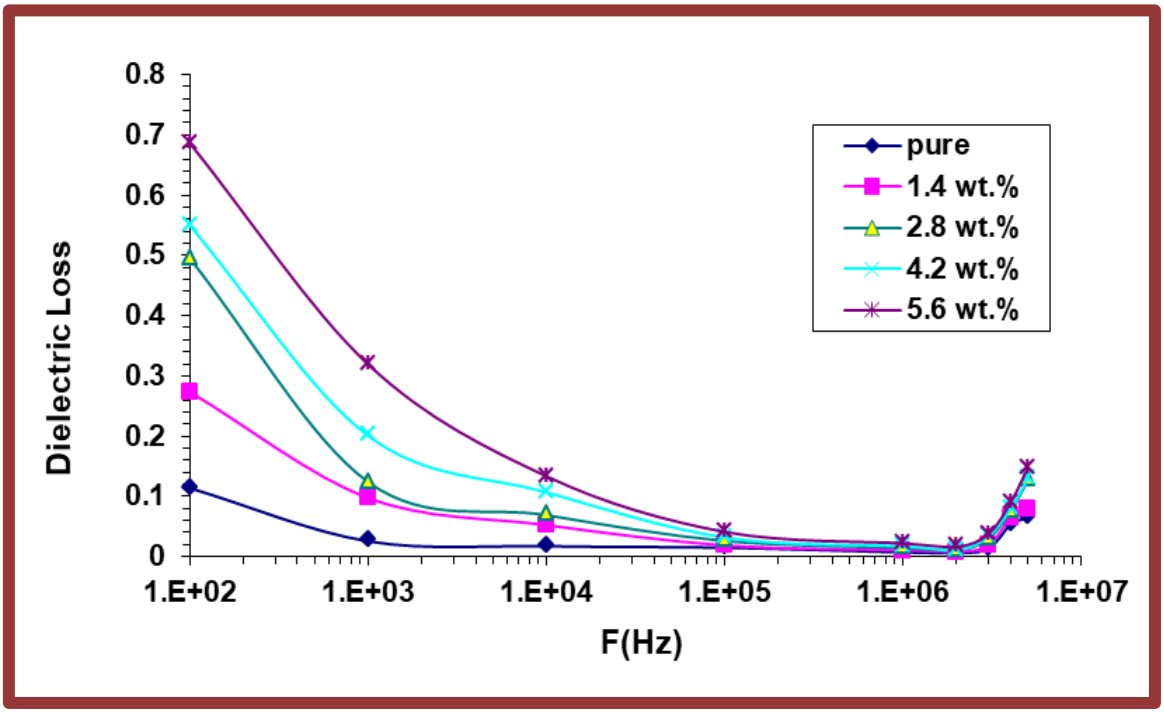

Figure. (4.35) Variation of dielectric loss for (PMMA -PC/Sb_2O_3-GO) Nanocomposites with frequency at room temperature.

Tables (4.13) Values of dielectric loss for (PMMA-PC/In_2O_3-GO) Nanocomposites at 100 Hz.

Samples	Concentrations of In_2O_3 NPs wt.%	Electrical dielectric loss
(PMMA-PC) blend	0	0.114
(PMMA-PC/In_2O_3-GO) Nanocomposites	1.4	0.190
(PMMA-PC/In_2O_3-GO) Nanocomposites	2.8	1.224
(PMMA-PC/In_2O_3-GO) Nanocomposites	4.2	2.217
(PMMA-PC/In_2O_3-GO) Nanocomposites	5.6	4.340

Tables (4.14) Values of dielectric loss for (PMMA-PC/Sb_2O_3-GO) Nanocomposites.

Samples	Concentrations of Sb_2O_3 NPs wt.%	Electrical dielectric loss
(PMMA-PC) blend	0	0.0256
(PMMA-PC/Sb_2O_3-GO) Nanocomposites	1.4	0.1170
(PMMA-PC/Sb_2O_3-GO) Nanocomposites	2.8	0.286
(PMMA-PC/Sb_2O_3-GO) Nanocomposites	4.2	0.301
(PMMA-PC/Sb_2O_3-GO) Nanocomposites	5.6	0.319

4.4.3 The A.C Electrical Conductivity of (PMMA-PC/In_2O_3-GO) and (PMMA-PC/Sb_2O_3-GO) Nanocomposites

Equation (2-20) is utilized to measure the A.C electrical conductivity of nanocomposites, and the effect of In_2O_3, $Sb_2O_3$and GO nanoparticles on A.C electrical conductivity for (PMMA-PC/In_2O_3-GO) and (PMMA-PC/Sb_2O_3-GO) nanocomposites is displayed in figures (4.36) and (4.37), respectively, at 100 Hz. The results depicted in Tables (4.15) and (4.16) demonstrate that the electrical conductivity of nanocomposites increases with increasing In_2O_3, $Sb_2O_3$and GO nanoparticle concentrations [148]. This phenomenon can be attributed to the increase in the number of charge carriers due to the doping effect of the nanoparticles, which gradually decreases the resistance of nanocomposites and increases A.C electrical conductivity. At concentrations of 5.6 wt.% for (PMMA-PC/In_2O_3-GO) and (PMMA-PC/Sb_2O_3-GO) nanocomposites, nanoparticles create a path network within the nanocomposite [149]. Figures (4.38) and (4.39) exhibit the variation of A.C electrical conductivity of (PMMA-PC/In_2O_3-GO) and (PMMA-PC/Sb_2O_3-GO) nanocomposites with frequency at room temperature, respectively. As illustrated, the A.C electrical conductivity of all prepared nanocomposites increases with the frequency of the electric field due to space charge polarization at low frequencies and the mobility of charge carriers by the hopping process. The mobility of charge carriers is boosted in the high-frequency range, leading to an increase in electrical conductivity for (PMMA-PC/In_2O_3-GO) and (PMMA-PC/Sb_2O_3-GO) nanocomposites, as reported by previous researchers [150].

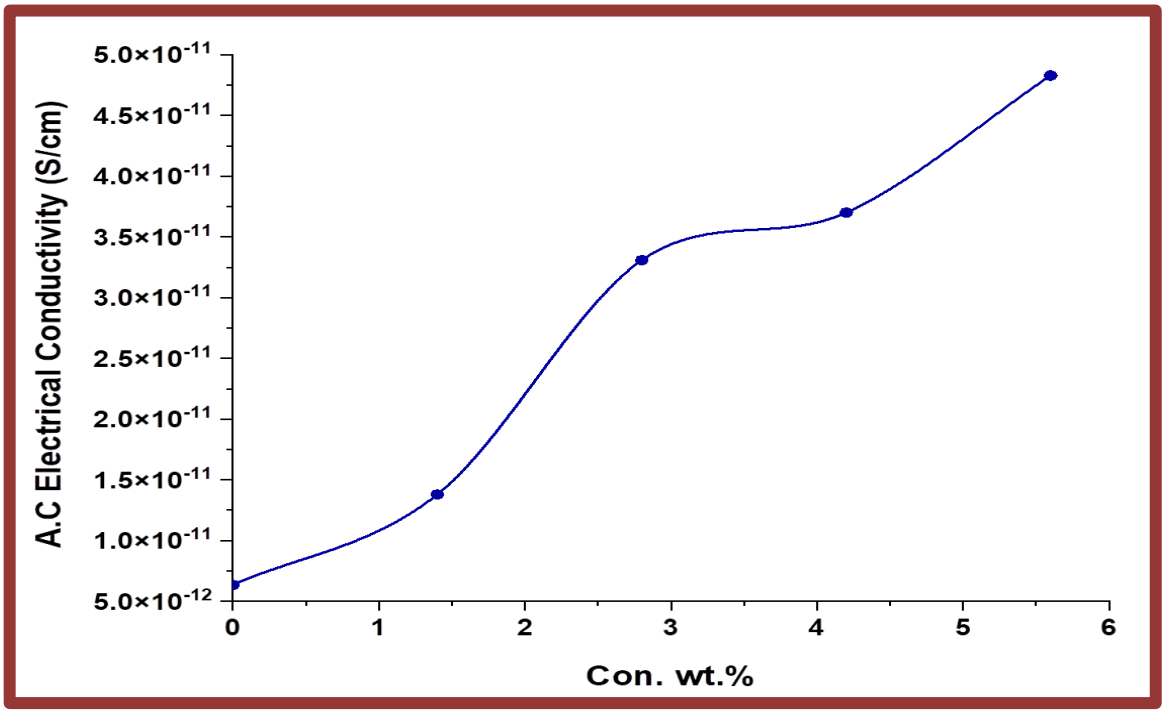

Figure (4.36) effect of (In_2O_3 -GO)concentrations on A.C electrical conductivity for (PMMA-PC) blend at 100Hz.

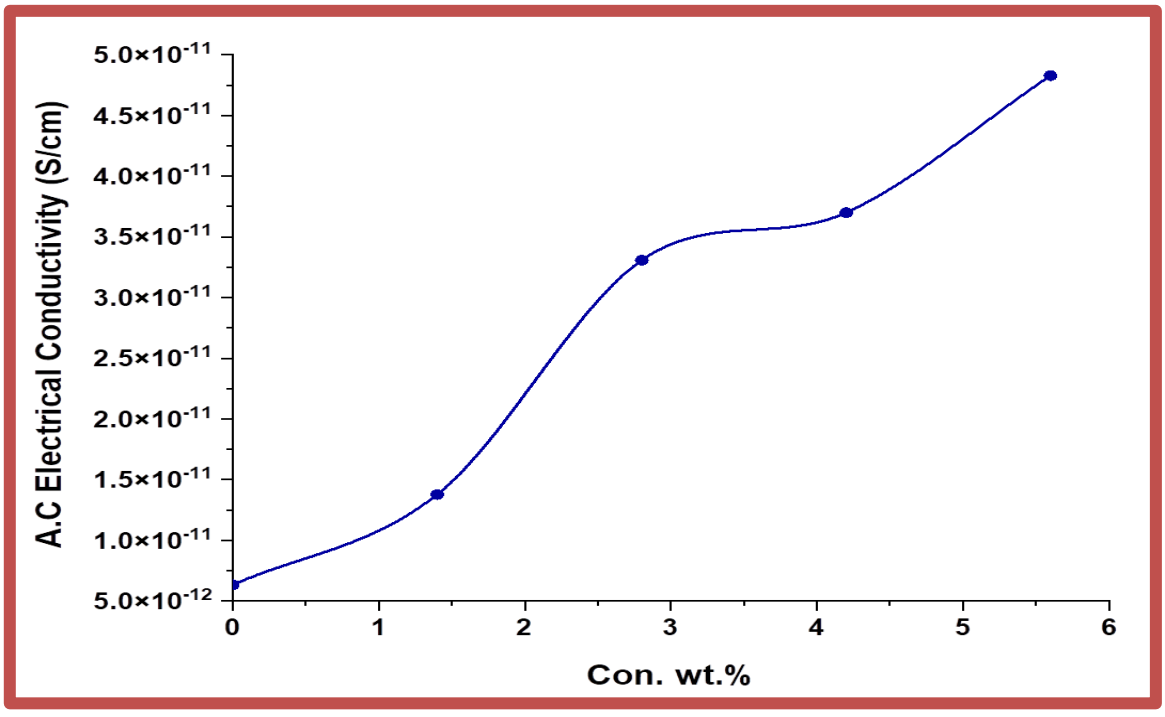

Figure (4.37):effect of (Sb_2O_3 -GO)concentrations on A.C electrical conductivit for (PMMA-PC) blend at 100Hz.

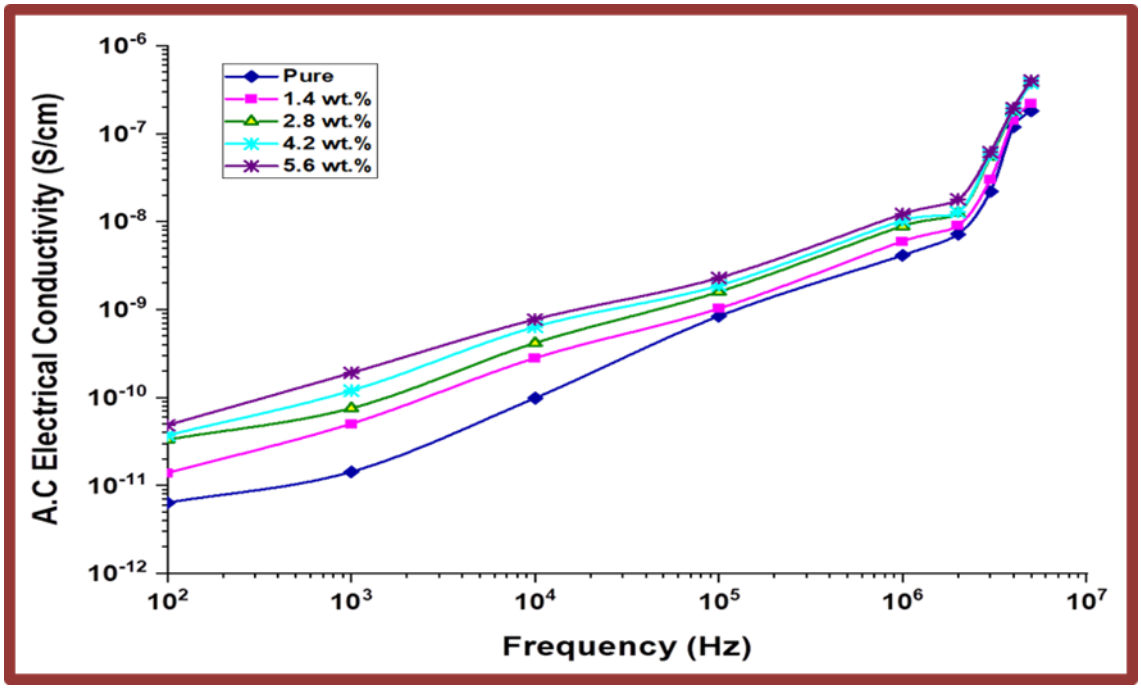

Figure (4.38) Variation of A.C electrical conductivity for (PMMA -PC/In_2O_3- GO) nanocomposites with frequency at room temperature.

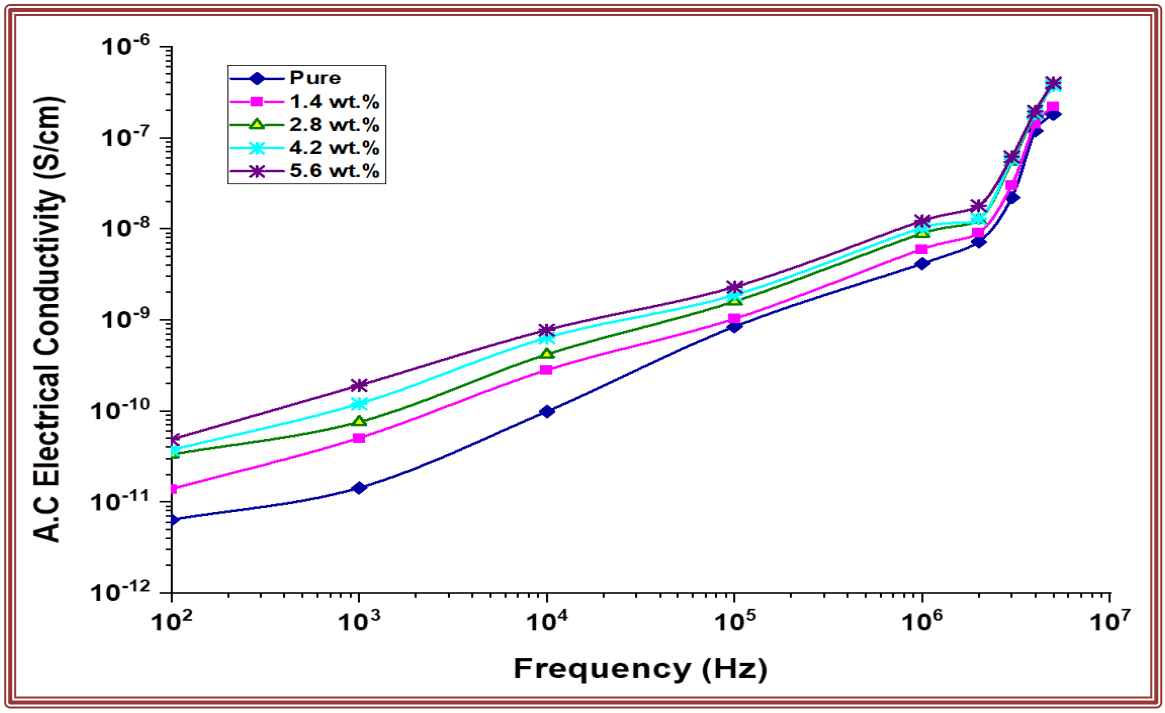

Figure (4.39) Variation of A.C electrical conductivity for (PMMA -PC/Sb_2O_3- GO) nanocomposites with frequency at room temperature.

Tables (4.15) Values of Electrical Conductivity for(PMMA-PC-In_2O_3-GO) Nanocomposites at 100 Hz.

Samples	Concentrations of In_2O_3-GO NPs wt.%	Electrical Conductivity $(\Omega.cm)^{-1}$
(PMMA-PC) blend	0	0.063×10^{-10}
(PMMA-PC/In_2O_3-GO) Nanocomposites	1.4	0.106×10^{-10}
(PMMA-PC/In_2O_3-GO) Nanocomposites	2.8	1.42×10^{-10}
(PMMA-PC/In_2O_3-GO) Nanocomposites	4.2	1.23×10^{-10}
(PMMA-PC/In_2O_3-GO) Nanocomposites	5.6	2.41×10^{-10}

Tables (4.16) Values of Electrical Conductivity for(PMMA-PC-Sb_2O_3-GO) Nanocomposites at 100 Hz.

Samples	Concentrations of Sb_2O_3-GO NPs wt.%	Electrical Conductivity $(\Omega.cm)^{-1}$
(PMMA/PC) blend	0	0.634×10^{-10}
PMMA-PC/Sb_2O_3-GO Nanocomposites	1.4	1.52×10^{-10}
PMMA-PC/Sb_2O_3-GO Nanocomposites	2.8	2.75×10^{-10}
PMMA-PC/Sb_2O_3-GO Nanocomposites	4.2	3.05×10^{-10}
PMMA-PC/Sb_2O_3-GO Nanocomposites	5.6	3.81×10^{-10}

4.5 The Applications (PMMA-PC/In_2O_3-GO) and (PMMA-PC/Sb_2O_3-GO) Nanocomposites.

4.5.1 Application of Nanocomposites for Photocatalytic Activity

Figures (4-40) and (4-41) show the behaviour of absorbance spectra for methylene orange dye with photon wavelength for (PMMA-PC/In_2O_3-GO) and (PMMA-PC/Sb_2O_3-GO) nanostructures samples is shown.The absorbance of MO is used to determine its degradation. Methylene orange dye absorption decreases in the UV region [151].The figures (4-42) and (4-43) depicts the impact of Uv light time on Methylene orange absorption through (PMMA-PC) ,(PMMA-PC/In_2O_3-GO) and (PMMA-PC/Sb_2O_3-GO)nanocomposites at 475 nm . The figures show that the absorbance of methylene orangey dye decreases as the irradiation period increases. The results show that at 5.6 wt.% In_2O_3, Sb_2O_3, and GO NPs, the degradation ratio of methylene orange dye reaches 80% in 90 minutes. The sample of nanocomposites (PMMA-PC/In_2O_3-GO) and (PMMA-PC/Sb_2O_3-GO) nanocomposites with a concentration of 5.6 wt.% In_2O_3, Sb_2O_3, and GO NPs in Tables (4-17) and (4-18) are regarded as the more excellent sample, exhibiting more significant decay in absorption compared to the other samples [152]. The degradation percentages of MO dye were used to assess the photocatalytic activity of (PMMA-PC/In_2O_3-GO) and (PMMA-PC/Sb_2O_3-GO) nanocomposites as illustrated in figures (4.44) and (4.45). The figures clearly shows that as the irradiation time increases, the degradation percentages increase; this behaviour is due to a rise in electron-hole pairs and a reduction in fix replication[153],which causes a surge in the decay percents and, consequently, an rises in photocatalytic activity[154] . Figures (4.46) and (4.47) shows the plot of $ln\ A/A_0$ vs UV irradiation time for (PMMA-PC/In_2O_3-GO) and (PMMA-PC/Sb_2O_3-GO) nanocomposites. The reaction kinetics of MO dye decay using (PMMA-PC/In_2O_3-GO) and (PMMA-PC/Sb_2O_3GO) photocatalysts

were investigated using the Langmuir-Hinshelwood designed kinetics model we also observed a minimum half-life period ($t_{1/2}$) of 38 min[155]. Because of the exact linear patterns between ln A/A_0 and the time, The degradation of MO dye for nanocomposites was found to follow quasi-reaction kinetics[156].

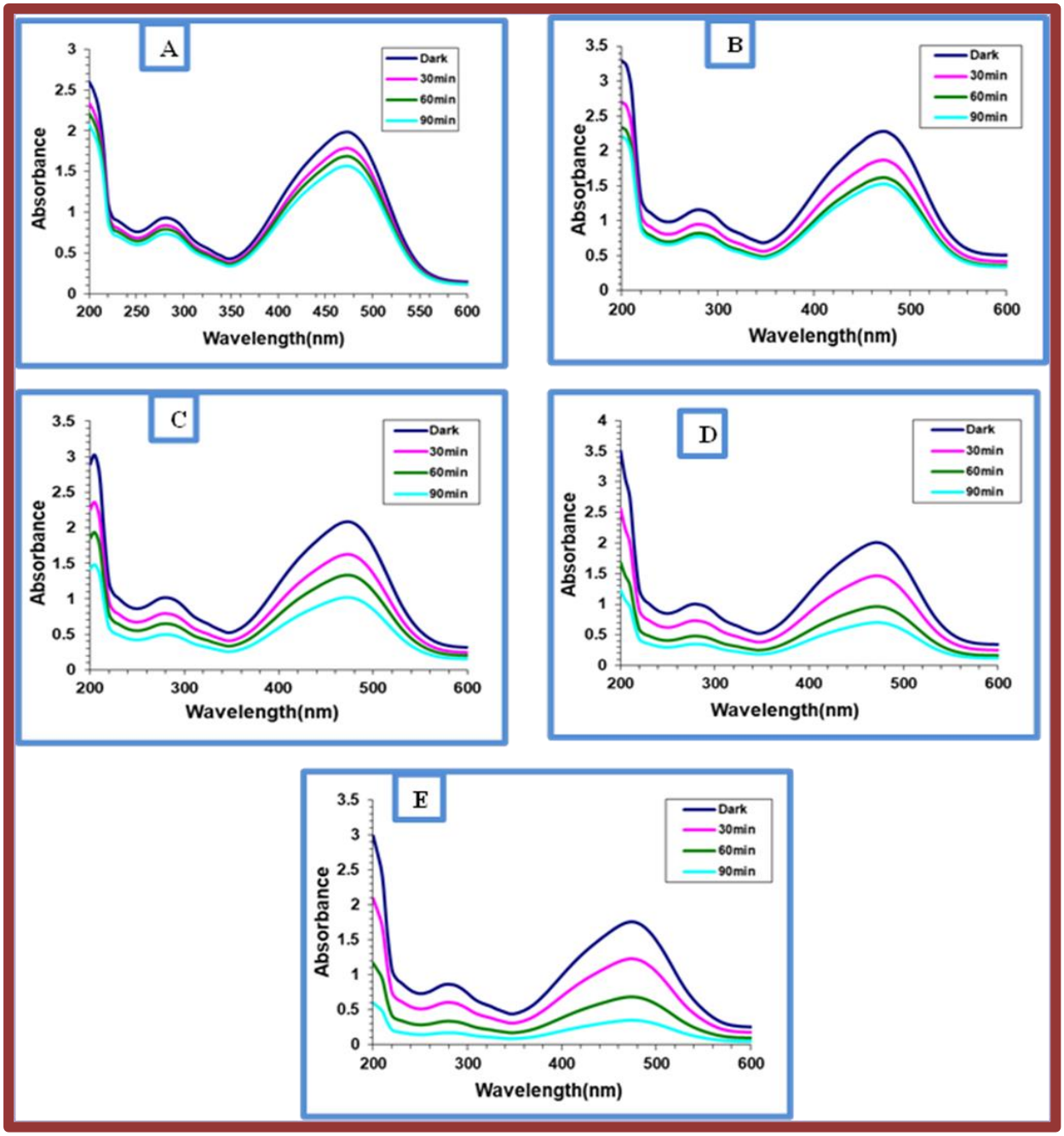

Figure (4.40) Absorbance spectra of MO dye solution for (PMMA-PC/In_2O_3-GO): nanocomposites (A) for (PMMA-PC) blend (B) for 1.4 wt.% In_2O_3-GO NPs (C) for 2.8 wt.% In_2O_3-GO NPs (D) for 4.2 wt In_2O_3-GO NPs (E) for 5.6 wt.% In_2O_3-GO NPs.

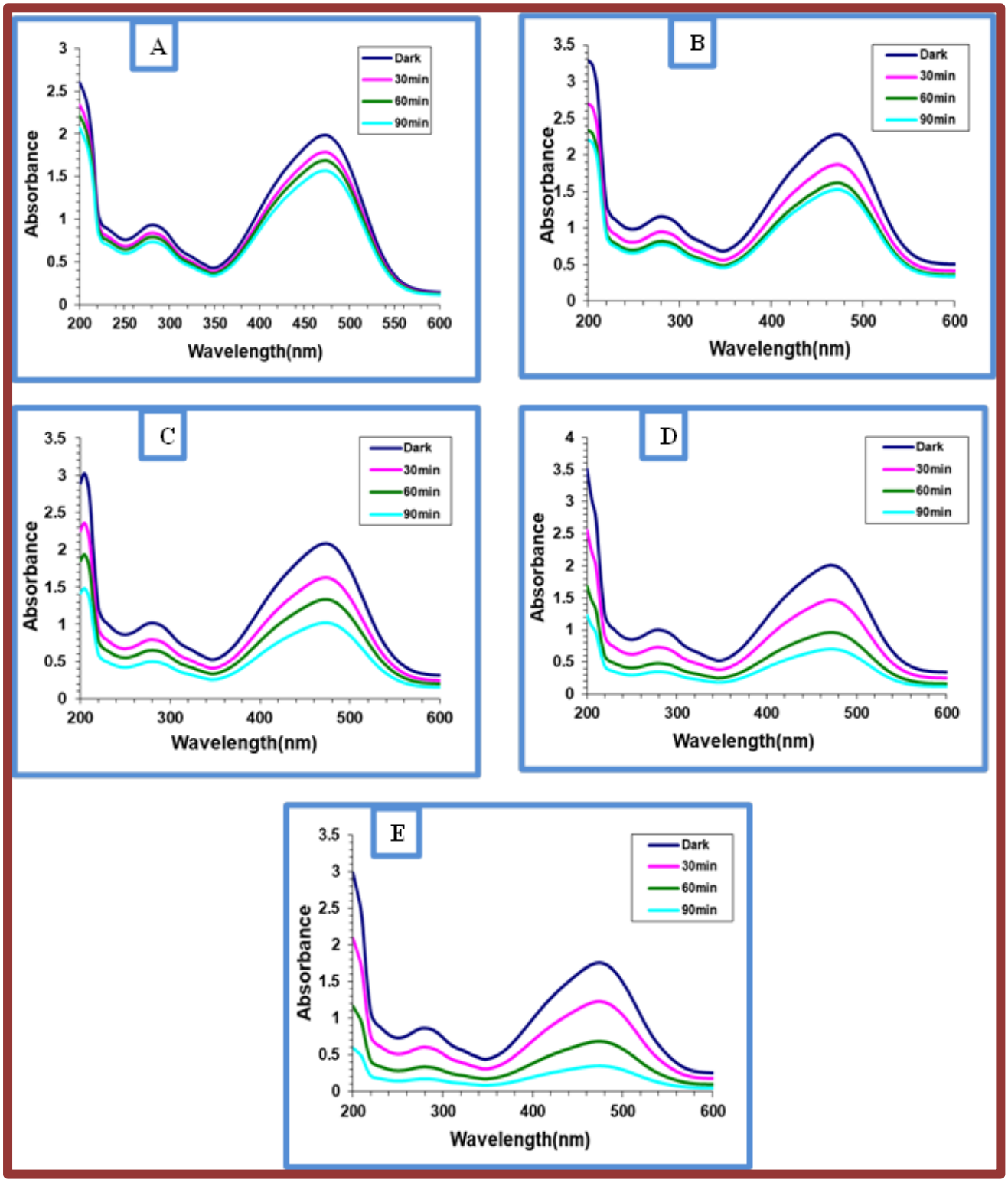

Figure (4.41) Absorbance spectra of MO dye solution for (PMMA-PC/Sb_2O_3-GO): nanocomposites (A) for (PMMA-PC) blend (B) for 1.4 wt.% Sb_2O_3-GO NPs (C) for 2.8 wt.% (D) for 4.2 wt Sb_2O_3-GO NPs (E) for 5.6 wt.% Sb_2O_3-GO NPs.

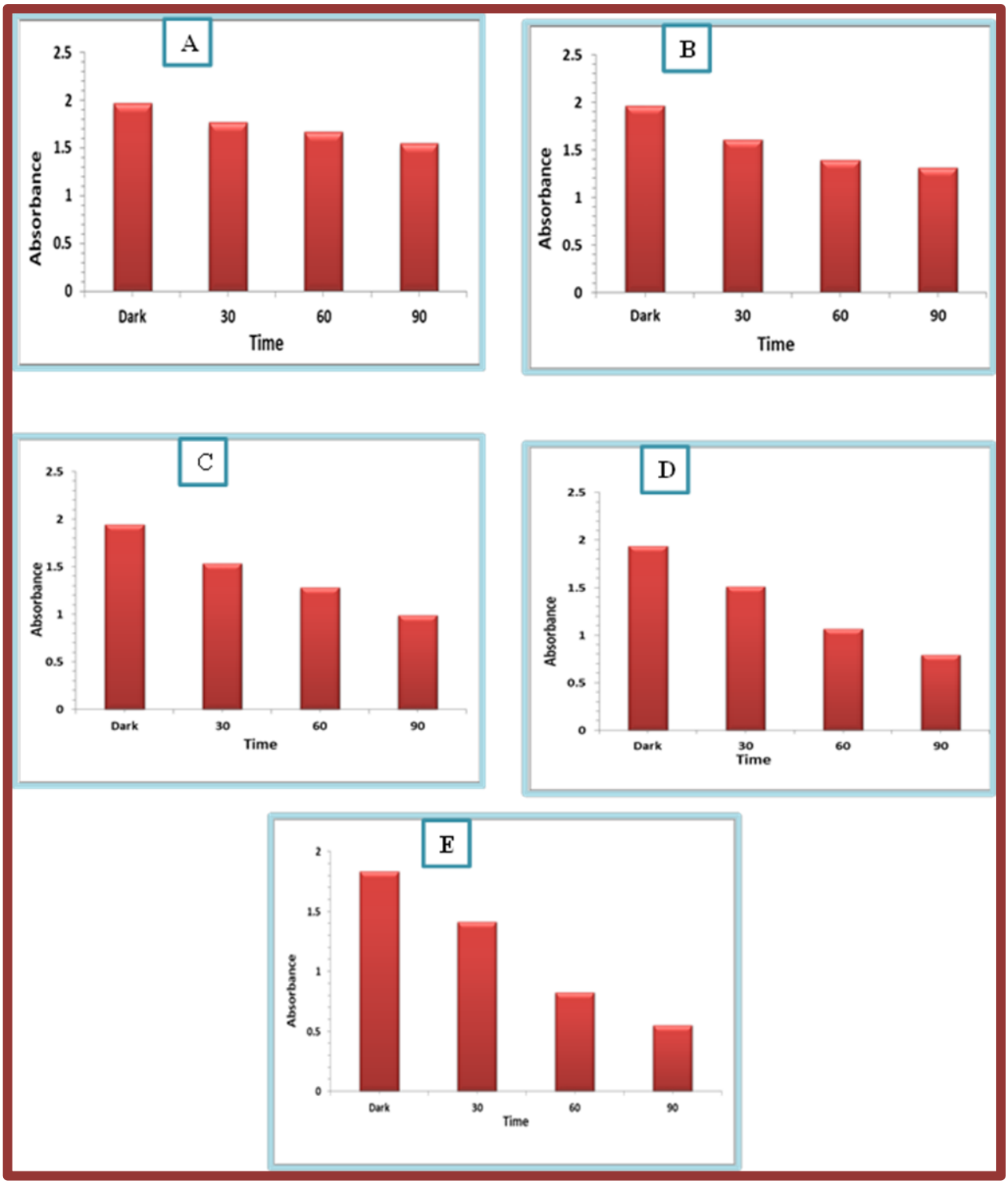

Figure (4.42) Behavior of absorbance spectra of MO dye with UV irradiation time for (PMMA-PC/In_2O_3-GO) nanocomposites: (A) for (PMMA-PC) blend (B) for 1.4 wt.% In_2O_3-GO NPs (C) for 2.8 wt.% In_2O_3-GO NPs (D) for 4.2 wt In_2O_3-GO NPs (E) for 5.6 wt.% In_2O_3-GO NPs.

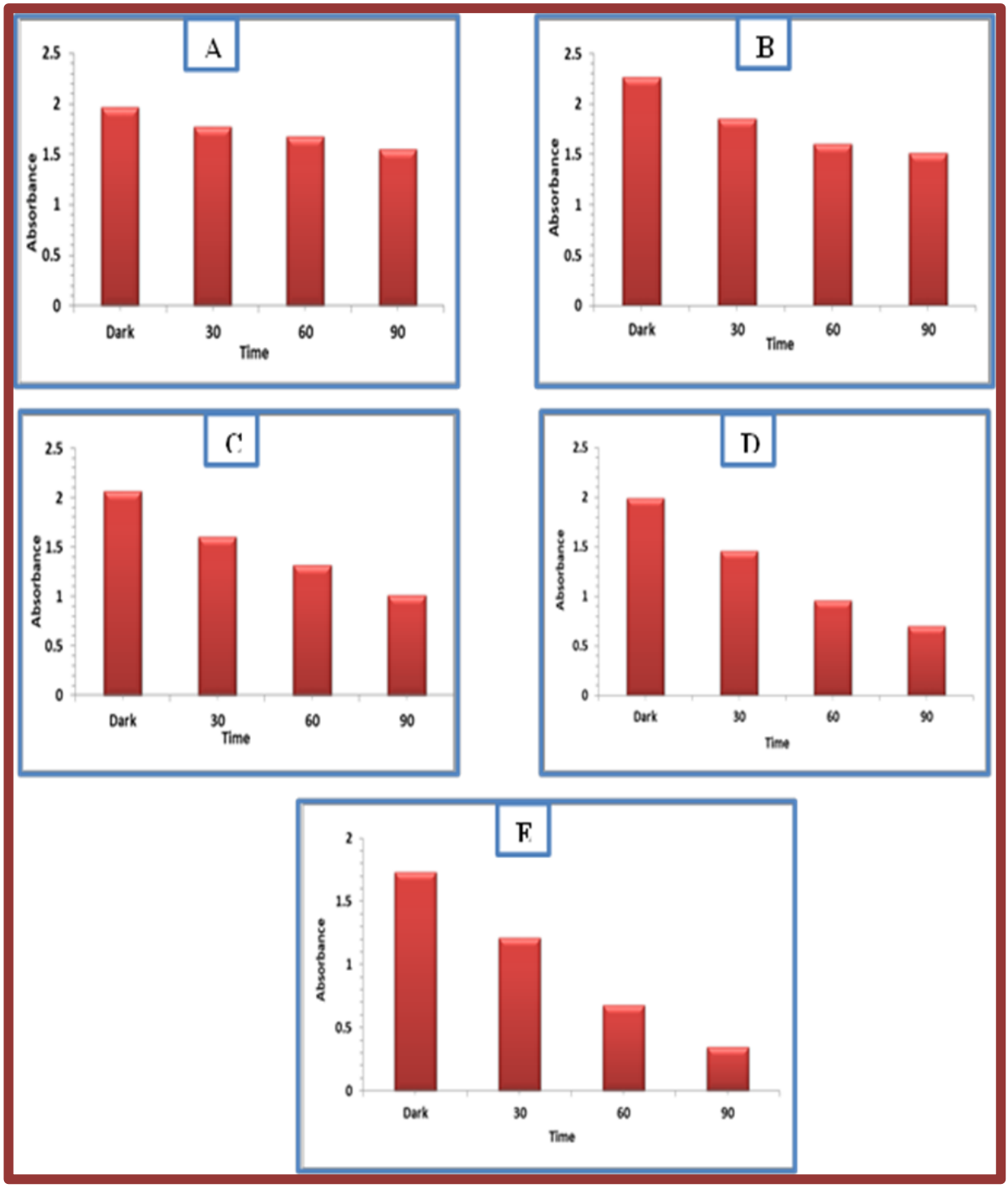

Figure (4.43) the MO dye absorbance spectra activity with UV irradiation time in (PMMA-PC/Sb_2O_3-GO) nanocomposites: (A) for (PMMA-PC) blend (B) for 1.4 wt.% Sb_2O_3-GO NPs (C) for 2.8 wt.% Sb_2O_3-GO NPs (D) for 4.2 wt Sb_2O_3-GO NPs (E) for 5.6 wt.% Sb_2O_3-GO NPs. Sb_2O_3-GO) NPs (D) for 4.2 wt Sb_2O_3-GO NPs (E) for wt.% Sb_2O_3-GO NPs.

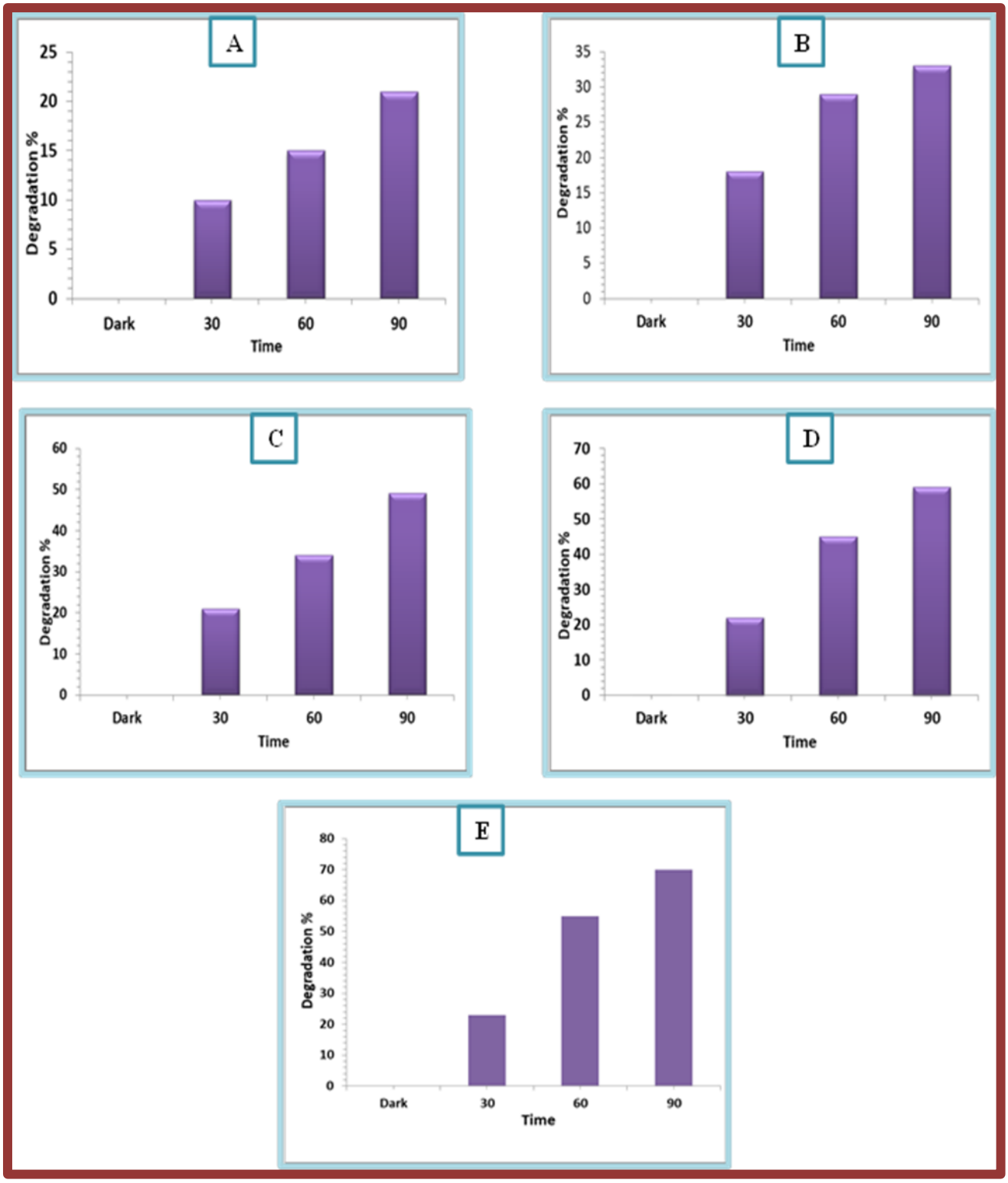

Figure (4.44) Effect of UV-irradiation time on degradation percentage of MO dye solution for (PMMA-PC/In_2O_3-GO) nanocomposites at 475 nm.

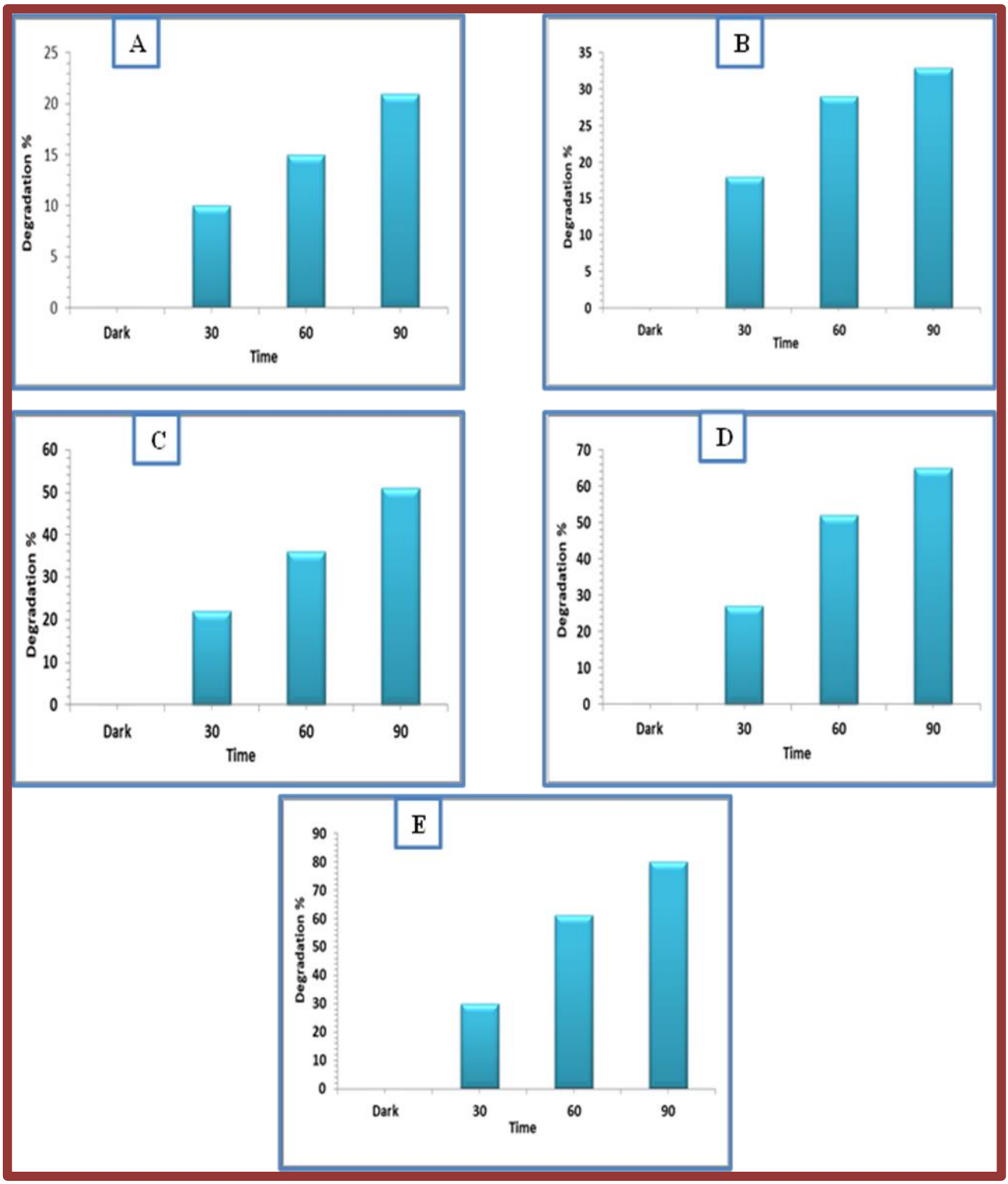

Figure (4.45) Effect of UV-irradiation time on degradation percentage of MO dye solution for (PMMA-PC/Sb_2O_3-GO) nanocomposites at 475 nm.

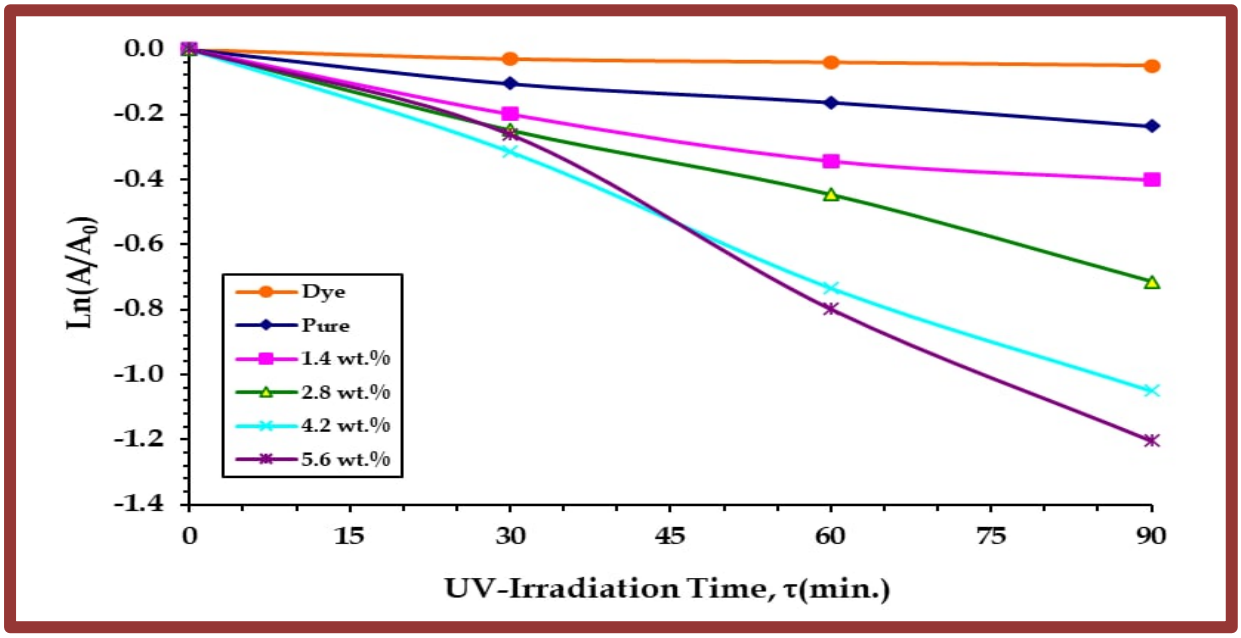

Figure (4-46) Shows the plot of $ln\ A/A_0$ vs UV irradition time for (PMMA-PC/In_2O_3-GO) nanocomposites

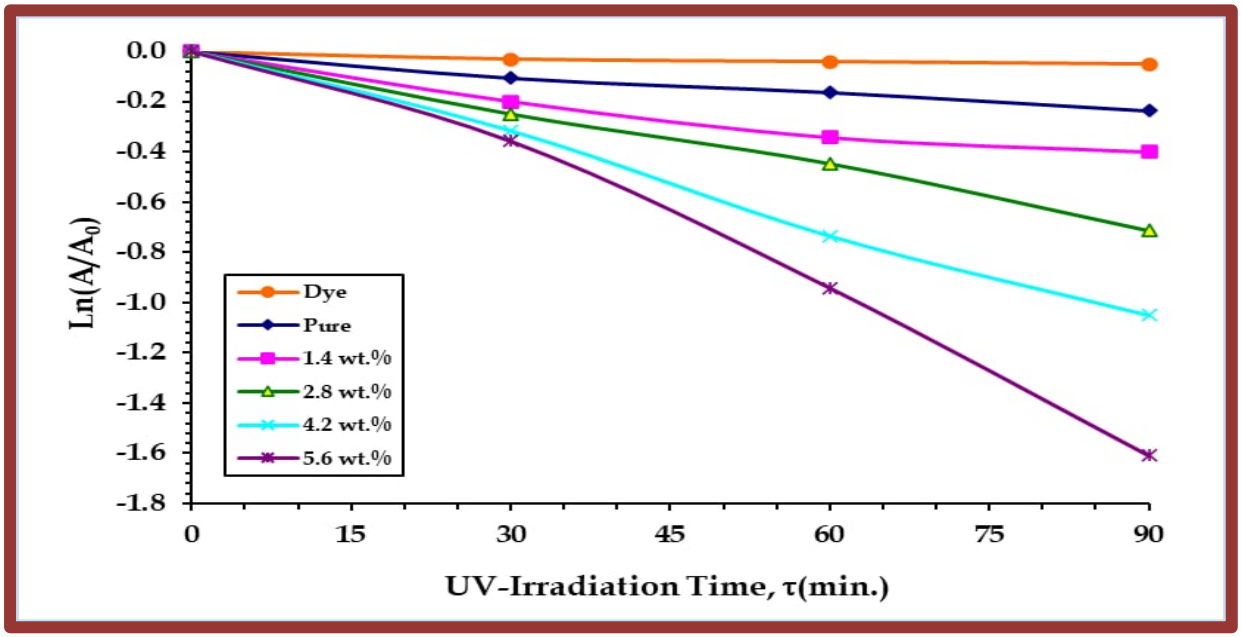

Figure (4-47) Shows the plot of $ln\ A/A_0$ vs UVirradition time for (PMMA-PC/Sb_2O_3-GO) nanocomposites.

Table (4.17) Degradation percentage of (PMMA-PC) blend, and (PMMA-PC/In_2O_3-GO) Nanocomposites at 475 nm.

Duration (min).	MO degradation %					
	MO dye	(PMMA-PC) blend	(In_2O_3-GO) Nanoparticles			
			1.4	2.6	4.2	5.6
0	0	0	0	0	0	0
30	8	10	18	21	22	23
60	7	15	29	34	45	55
90	6	21	33	49	59	70

Table (4.18) Degradation percentage of (PMMA-PC) blend and (PMMA-PC/Sb_2O_3-GO) Nanocomposites at 475 nm.

Duration (min).	MO degradation %					
	MO dye	(PMMA-PC) blend	(PMMA-PC / Sb_2O_3-GO) Nanocomposites			
			1.4	2.8	4.2	5.6
0	0	0	0	0	0	0
30	3	14	18	22	27	30
60	4	19	29	36	52	61
90	5	25	33	51	65	80

4.5.2 Application of Nanocomposites for Antibacterial Activity

Figures (4.48 to 4.53) show that both (PMMA-PC/In_2O_3-GO) and (PMMA-PC/Sb_2O_3-GO) nanocomposites possess antibacterial properties against Staphylococcus aureus and Escherichia coli. The size of the inhibition zone increases with an increase in the concentration of Indium trioxide , antimony trioxide , and graphene oxide nanoparticles in the nanocomposites. The possible mechanism for this antibacterial activity is that the positively charged nanoparticles of the nanocomposites attract the negatively charged bacterial cells through electromagnetic forces [157]. This interaction leads to the oxidation of the bacterial cells, causing their instant death. Another possible mechanism for the antibacterial activity of the nanocomposites involves the release of electron-hole pairs from Indium trioxide , antimony trioxide , and graphene oxide nanoparticles upon exposure to visible or ultraviolet light [158] . Water molecules can interact with these electron-hole pairs, generating hydroxide ions (OH^-) and hydrogen ions (^+H). Oxygen molecules can also react with the nanocomposites to produce peroxide anions ($O^{\cdot -2}$) which can react with hydrogen ions (^+H) to form hydrogen peroxide ($\cdot HO_2$). This hydrogen peroxide can further react with hydrogen ions (^+H) and electrons (e) to produce hydrogen peroxide (H_2O_2) molecules [159]. The concentration of H_2O_2 molecules generated depends on the surface area of the Indium trioxide , antimony trioxide , and graphene oxide nanoparticles. These reactive oxygen species (ROS) can penetrate the bacterial cell wall and cause damage, leading to their death. This process is referred to as ROS Generation by (PMMA-PC/In_2O_3-GO) and (PMMA-PC/Sb_2O_3-GO) nanocomposites [160] :

$$NCs + h\upsilon \rightarrow e^- + h^+$$

$$H_2O + h^+ \rightarrow OH^{\cdot} + H^+$$

$$e^- + O_2 \rightarrow \cdot O^-_2$$

$O^{\cdot -2} + H^{+} \rightarrow OH^{\cdot}$

$2OH^{\cdot} + H^{+} + e^{-} \rightarrow H_2O_2$

Hydrogen peroxide (H_2O_2) can only penetrate and destroy the bacterial membrane. Since the membrane carries negative charges, superoxide anions ($O^{\cdot -}_2$) and hydroxyl radicals ($OH^{\cdot}$) cannot penetrate and remain on the membrane surface. However, the interaction between illumination and these radicals generates oxidative stress, inhibiting bacterial proliferation[161].

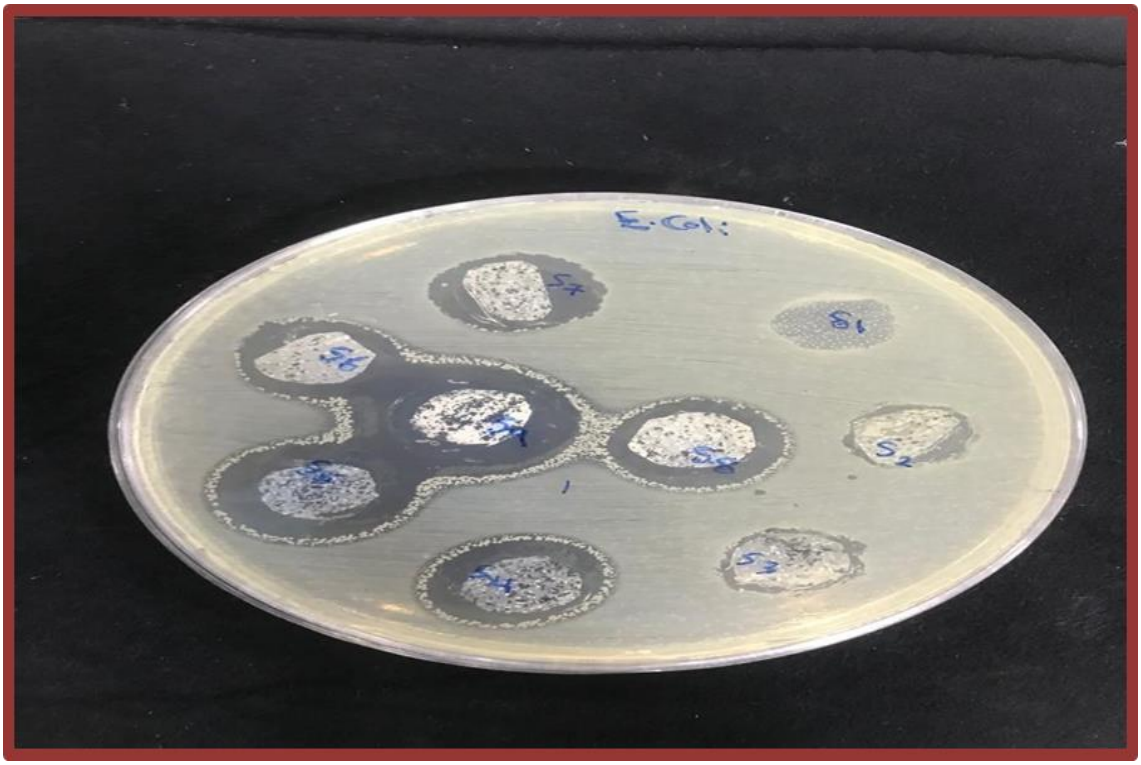

Figure (4.48) Antibacterial activity of (PMMA-PC-In_2O_3-GO) and (PMMA -PC/Sb_2O_3- GO) nanocomposite. Zone of inhibition of (PMMA-PC-In_2O_3-GO) and (PMMA -PC/Sb_2O_3- GO) against Escherichia coli.

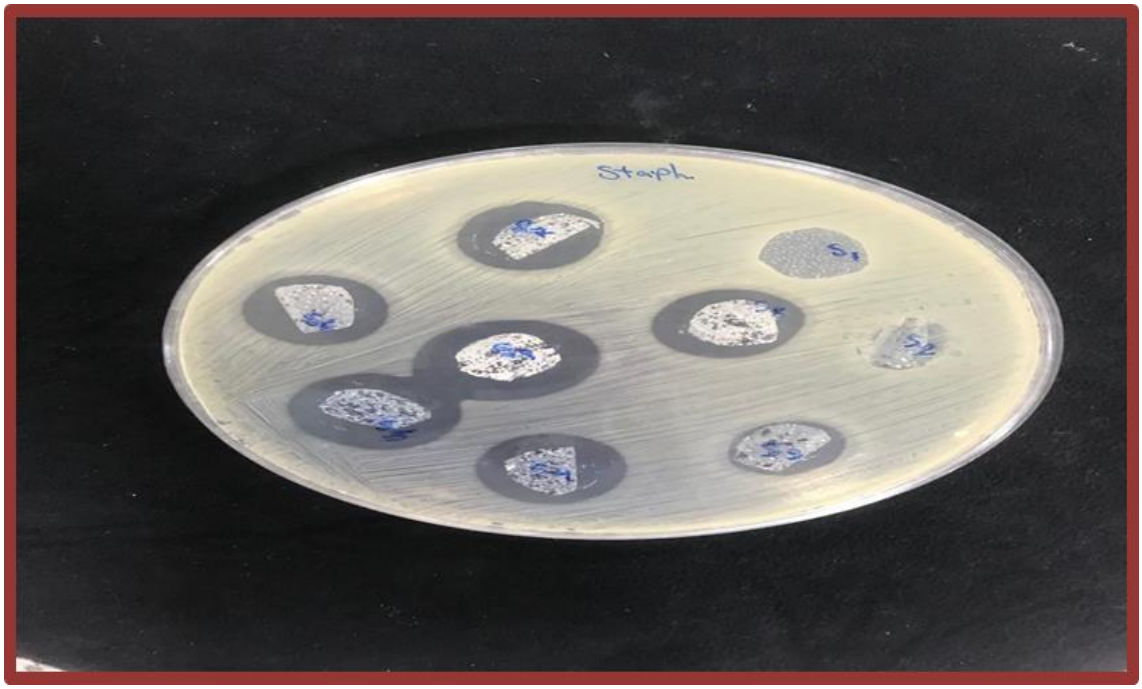

Figure (4.49) Antibacterial activity of (PMMA-PC-In_2O_3-GO) and (PMMA -PC/Sb_2O GO) nanocomposite. Zone of inhibition of (PMMA-PC-In_2O_3-GO) and (PMMA – PC/Sb_2O_3- GO) nanocomposite against Staphylococcus.

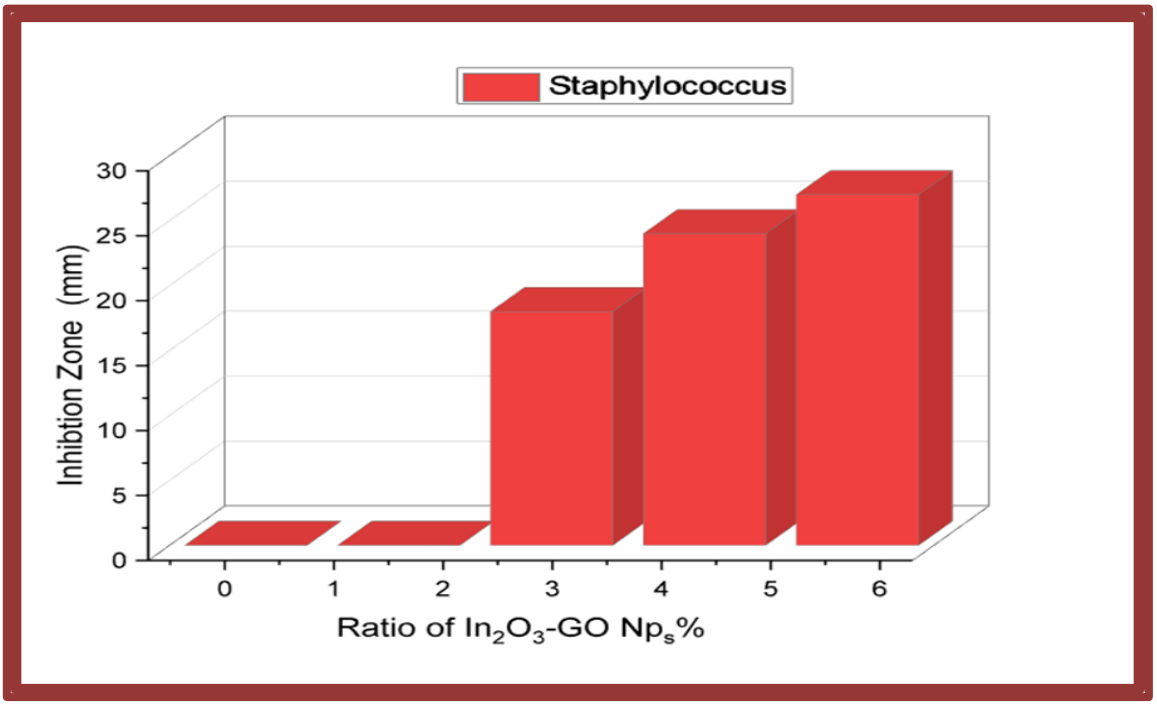

Figure (4-50) Variation of inhibition zone diameter with (In_2O_3-GO)NPs concentrations against Staphylococcus for (PMMA-PC/ In_2O_3-GO) nanocomposites.

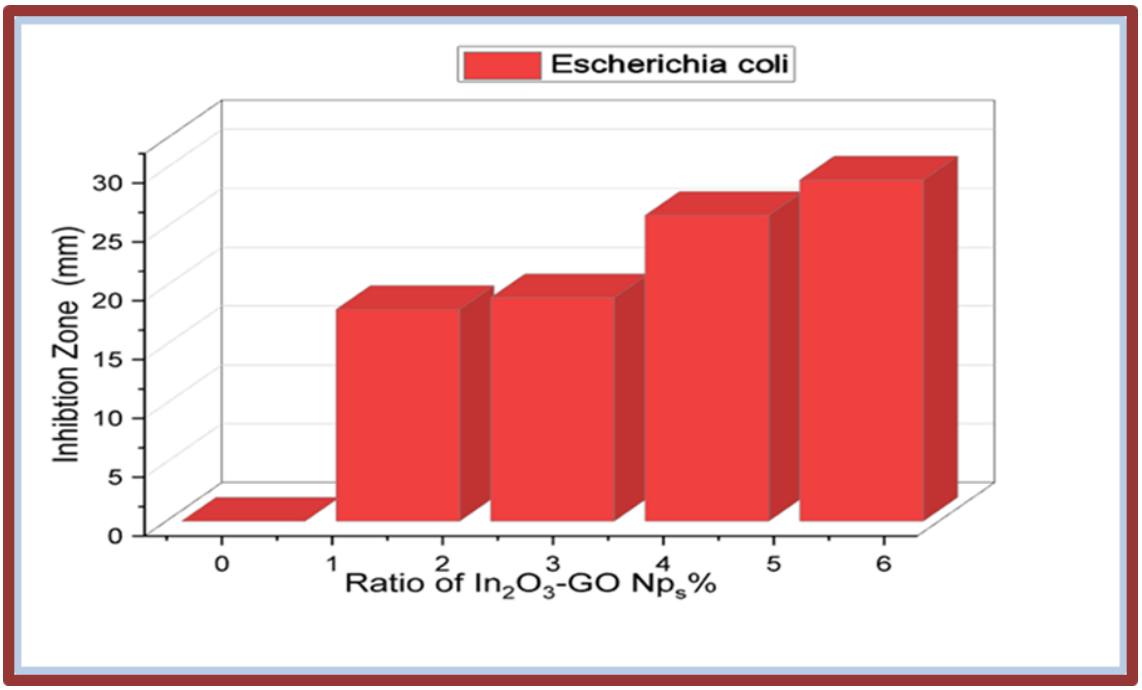

Figure (4-51) Variation of inhibition zone diameter with (In_2O_3-GO)NPs concentrations against Escherichia coli for (PMMA-PC/ In_2O_3-GO) nanocomposites.

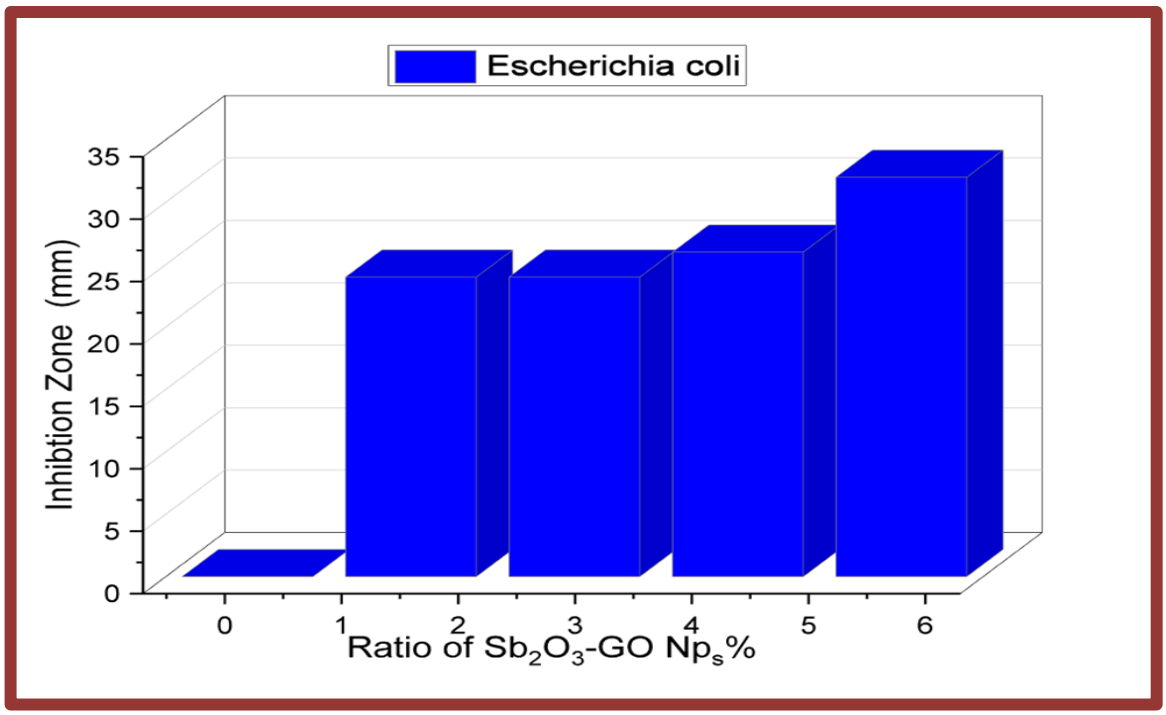

Figure (4-52) Variation of inhibition zone diameter with (Sb_2O_3-GO) -GO)NPs concentrations against Escherichia coli for (PMMA-PC/ Sb_2O_3-GO) nanocomposites

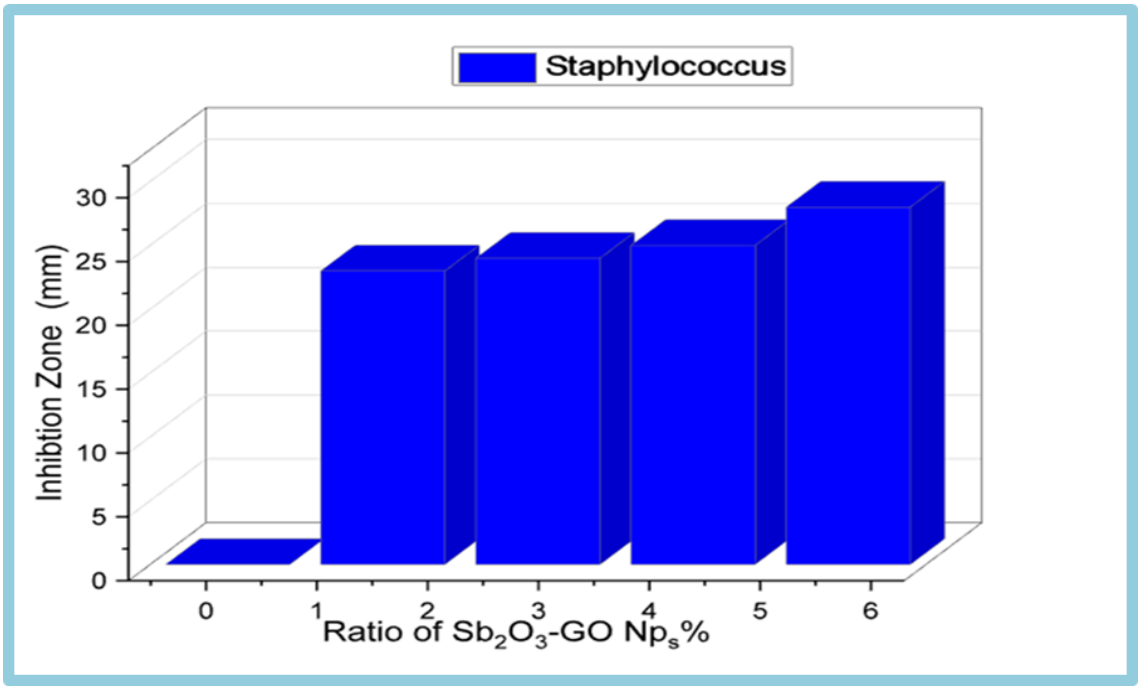

Figure (4-53) Variation of inhibition zone diameter with (Sb_2O_3-GO) -GO)NPs concentrations against Staphylococcus for (PMMA-PC/ Sb_2O_3-GO) nanocomposites.

4.6 Conclusions

In our study, the following results were obtained:

1- The distributions of indium trioxide ,antimony oxide and graphene oxide nanoparticles additives are improved at (4.2 and 5.6) wt.% concentrations by forming a path network inside the (PMMA-PC) blend

2- The XRD patterns of the prepared pure Sb2O3, In2O3, and GO nanoparticles show three peaks near 13.70°, 26°, and 30.8° of (Sb2O3), and three peaks of the cubic In_2O_3 crystal structure which is corresponding to the positions $2\theta = 29.9^o$, 34.1^o, and 47.8^o respectively.The XRD pattern of graphene oxide shows a peak at $2\theta = 10.1°$ (d-spacing of 8.9 Å), the (100) diffraction peak at $2\theta = 43.0°$

3- The optical properties of (PMMA-PC/In_2O_3-GO) and (PMMA-PC/Sb_2O_3-GO) nanocomposites are enhanced as the weight percentages of (In_2O_3, Sb_2O_3, and GO) nanoparticles increase.When 5.6% (In_2O_3, Sb_2O_3, and GO) nanocomposites nanoparticles are added, , while the optical conductivity increases by 48% and 50%, respectively.

4- The energy gaps for allowed transition decreased by 51% and 48%, respectively, and the indirect forbidden energy gaps reduced by 77% and 80%, respectively. Additionally, the refractive index increases by 25% and 22%, respectively.

5- A.C electrical properties of nanocomposites is increased with an increase in concentration of nanapartical.

6- As the irradiation time increases, the absorbance of methylene orange dye solution in (PMMA-PC/In_2O_3-GO) and (PMMA-PC/Sb_2O_3-GO) nanocomposites decreases. the optimal photocatalytic activity occurs at a concentration of 5.6 %wt nanoparticles. The photodegradation percentage of MO dye is 10% within 30 minutes and 67% within 90 minutes.

7- The (PMMA-PC/In_2O_3-GO) and (PMMA-PC/Sb_2O_3-GO)nanocomposites have higher inhibition zone for S. aureus and E. coli bacteria at (4.2 and 5.6) wt.% concentrations.

4.7 Suggestions for Future Work

1- Studying the effect of In_2O_3, Sb_2O_3 and GO nanoparticles on the thermal conductivity of the (PMMA-PC) blend.

2- Studying the mechanical properties of (PMMA-PC/In_2O_3-GO) and (PMMA-PC/Sb_2O_3-GO) nanocomposites.

3- Studying the D.C electrical conductivity at different temperatures of (PMMA-PC/In_2O_3-GO) and (PMMA-PC/Sb_2O_3-GO) nanocomposites.

4- Studying the presser sensors, swelling degree and contact angle /wettability application of (PMMA-PC/In_2O_3-GO) and (PMMA-PC/Sb_2O_3-GO) nanocomposites.

References

1. DiSanto, R.M., Subramanian, V., Gu, Z.: Recent advances in nanotechnology for diabetes treatment. Wiley Interdiscip. Rev. Nanomedicine Nanobiotechnology. 7, 548–564 (2015)
2. Anandharamakrishnan, C., Parthasarathi, S.: Food nanotechnology: principles and applications. CRC Press (2019)
3. Joshi, M., Bhattacharyya, A., Ali, S.W.: Characterization techniques for nanotechnology applications in textiles. (2008)
4. Logothetidis, S.: Nanotechnology: Principles and applications. In: Nanostructured materials and their applications. pp. 1–22. Springer (2011)
5. Luisa, F., Duncan, S.: Nanotechnologies: principles, applications, implications and hands-on activities. Luxemb. Dir. Gen. Res. Innov. Ind. Technol. Eur. Union. (2012)
6. Koodali, R.T., Klabunde, K.J.: Nanotechnology: fundamental principles and applications. In: Handbook of industrial chemistry and biotechnology. pp. 249–263. Springer (2012)
7. Yang, Y., Jiao, P.: Nanomaterials and nanotechnology for biomedical soft robots. Mater. Today Adv. 17, 100338 (2023)
8. Rodriguez-Narvaez, O.M., Peralta-Hernandez, J.M., Goonetilleke, A., Bandala, E.R.: Biochar-supported nanomaterials for environmental applications. J. Ind. Eng. Chem. 78, 21–33 (2019)
9. Meredith, J.C., Karim, A., Amis, E.J.: Combinatorial methods for investigations in polymer materials science. Mrs Bull. 27, 330–335 (2002)
10. Harrison, I.R.: Polymer materials science, Jerold M. Schultz, Prentice-Hall, Englewood Cliffs, NJ, 1974, 524 pp., (1974)
11. Singh, J., Singh, S., Gill, R.: Applications of biopolymer coatings in biomedical engineering. J. Electrochem. Sci. Eng. 13, 63–81 (2023)
12. Biswas, M.C., Jony, B., Nandy, P.K., Chowdhury, R.A., Halder, S.,

Kumar, D., Ramakrishna, S., Hassan, M., Ahsan, M.A., Hoque, M.E.: Recent advancement of biopolymers and their potential biomedical applications. J. Polym. Environ. 1–24 (2021)

13. Dodgson, K.S., Price, R.G.: A note on the determination of the ester sulphate content of sulphated polysaccharides. Biochem. J. 84, 106 (1962)
14. Torres, F.G., Troncoso, O.P., Pisani, A., Gatto, F., Bardi, G.: Natural polysaccharide nanomaterials: an overview of their immunological properties. Int. J. Mol. Sci. 20, 5092 (2019)
15. Houlihan, G., Arangundy-Franklin, S., Holliger, P.: Engineering and application of polymerases for synthetic genetics. Curr. Opin. Biotechnol. 48, 168–179 (2017)
16. Rydz, J., Sikorska, W., Kyulavska, M., Christova, D.: Polyester-based (bio) degradable polymers as environmentally friendly materials for sustainable development. Int. J. Mol. Sci. 16, 564–596 (2014)
17. Chen, G.-Q., Patel, M.K.: Plastics derived from biological sources: present and future: a technical and environmental review. Chem. Rev. 112, 2082–2099 (2012)
18. George, A., Sanjay, M.R., Srisuk, R., Parameswaranpillai, J., Siengchin, S.: A comprehensive review on chemical properties and applications of biopolymers and their composites. Int. J. Biol. Macromol. 154, 329–338 (2020)
19. Van de Velde, K., Kiekens, P.: Biopolymers: overview of several properties and consequences on their applications. Polym. Test. 21, 433–442 (2002)
20. Bhaiswar, J.B., Salunkhe, M.Y., Dongre, S.P., Kumbhare, B.T.: Comparative study on thermal stability and optical properties of PANI/CdS and PANI/PbS nanocomposite. IOSR J. Appl. Phys.(ICAET-2014). 80, 79–82 (2014)
21. Shanshool, H.M., Yahahya, M., Yunus, W.M.M., Abdullah, I.Y.: Optical

properties of PMMA/ZnO nanocomposites as foils prepared by casting method. Aust. J. Bas. Appli. Sci. 9, 401–409 (2015)

22. Ajitha, A.R., Thomas, S.: Compatibilization of polymer blends. Compat. Polym. Blends, Elsevier2019. 640 (2020)
23. Rhim, J.W., Wang, L.F., Hong, S.I.: Preparation and characterization of agar/silver nanoparticles composite films with antimicrobial activity. Food Hydrocoll. 33, 327–335 (2013)
24. Potts, J.R., Dreyer, D.R., Bielawski, C.W., Ruoff, R.S.: Graphene-based polymer nanocomposites. Polymer (Guildf). 52, 5–25 (2011)
25. Sharma, A.K., Kaith, B.S.: Polymer nanocomposite matrices: classification, synthesis methods, and applications. In: Handbook of Polymer and Ceramic Nanotechnology. pp. 403–428. Springer (2021)
26. Hurayra–Lizu, K.M.A., Bari, M.W., Gulshan, F., Islam, M.R.: GO based PVA nanocomposites: tailoring of optical and structural properties of PVA with low percentage of GO nanofillers. Heliyon. 7, e06983 (2021)
27. Samrot, A. V, Saigeetha, S., Shobana, N., Chandrasekaran, K.: Green-synthesized nanoparticle-based polymer nanocomposites: synthesis, characterizations, and applications. In: Biodegradable and Biocompatible Polymer Nanocomposites. pp. 241–270. Elsevier (2023)
28. Gupta, T.K., Kumar, S.: Fabrication of carbon nanotube/polymer nanocomposites. In: Carbon Nanotube-Reinforced Polymers. pp. 61–81. Elsevier (2018)
29. Zadehnazari, A.: Metal oxide/polymer nanocomposites: A review on recent advances in fabrication and applications. Polym. Technol. Mater. 62, 655–700 (2023)
30. Lawal, A.T.: Recent progress in graphene based polymer nanocomposites. Cogent Chem. 6, 1833476 (2020)
31. Ismail, N.M., Ismail, A.F., Mustafa, A., Zulhairun, A.K., Aziz, F., Bolong, N., Razali, A.R.: Polymer clay nanocomposites for gas separation: A

review. Environ. Contam. Rev. 2, 1–5 (2019)

32. Nguyen, T.-P., Yang, S.-H.: Hybrid materials based on polymer nanocomposites for environmental applications. In: Polymer-based Nanocomposites for Energy and Environmental Applications. pp. 507–551. Elsevier (2018)
33. Sivasubramanian, P., Chang, J.-H., Nagendran, S., Dong, C.-D., Shkir, M., Kumar, M.: A review on bismuth-based nanocomposites for energy and environmental applications. Chemosphere. 135652 (2022)
34. Sahani, S., Kim, T.: Metal Nanocomposites for Energy and Environmental Applications. Met. Nanocomposites Energy Environ. Appl. 293–318 (2022)
35. Dixit, M., Mathur, V., Gupta, S., Baboo, M., Sharma, K., Saxena, N.S.: Morphology, miscibility and mechanical properties of PMMA/PC blends. Phase Transitions. 82, 866–878 (2009)
36. Çapan, R., Ray, A.K., Hassan, A.K., Tanrisever, T.: Poly (methyl methacrylate) films for organic vapour sensing. J. Phys. D. Appl. Phys. 36, 1115 (2003)
37. Christensen, R.M.: Mechanics of composite materials. Courier Corporation (2012)
38. Mu, X., Jin, Z., Chu, F., Cai, W., Zhu, Y., Yu, B., Song, L., Hu, Y.: High-performance flame-retardant polycarbonate composites: Mechanisms investigation and fire-safety evaluation systems establishment. Compos. Part B Eng. 238, 109873 (2022)
39. Quereda, J., Kuriakose, S., Munuera, C., Mompean, F.J., Al-Enizi, A.M., Nafady, A., Diez, E., Frisenda, R., Castellanos-Gomez, A.: Scalable and low-cost fabrication of flexible WS2 photodetectors on polycarbonate. npj Flex. Electron. 6, 23 (2022)
40. Petousis, M., Vidakis, N., Mountakis, N., Grammatikos, S., Papadakis, V., David, C.N., Moutsopoulou, A., Das, S.C.: Silicon Carbide Nanoparticles

as a Mechanical Boosting Agent in Material Extrusion 3D-Printed Polycarbonate. Polymers (Basel). 14, 3492 (2022)

41. Zahmatkesh, S., Amiri, M.K., Zaferani, S.P.G., Emami, M.R.S., Hajiaghaei-Keshteli, M., Albaqami, M.D., Tighezza, A.M., Shafahi, M., Han, N.: Machine learning modeling of polycarbonate ultrafiltration membranes at different temperatures, Al_2O_3 nanoparticle volumes, and water ratios. Chemosphere. 313, 137424 (2023)
42. Sabur, D.A., Hashim, A., Habeeb, M.A.: Fabrication and exploration the structural and optical properties of Sb2O3-GO nanostructures doped PMMA-PC for photodegradation of pollutants dyes. Opt. Quantum Electron. 55, 457 (2023)
43. Svensson, C.: The crystal structure of orthorhombic antimony trioxide, Sb2O3. Acta Crystallogr. Sect. B Struct. Crystallogr. Cryst. Chem. 30, 458–461 (1974)
44. Moseley, D.H., Bridges, C.A., Daemen, L.L., Zhang, Q., McGuire, M.A., Cakmak, E., Hermann, R.P.: Structure and Anharmonicity of α-and β-Sb2O3 at Low Temperature. Crystals. 13, 752 (2023)
45. Yamuna, A., Chen, T.-W., Chen, S.-M.: Synthesis and characterizations of iron antimony oxide nanoparticles and its applications in electrochemical detection of carbendazim in apple juice and paddy water samples. Food Chem. 373, 131569 (2022)
46. Aparna, C., Shetty, P.K., Mahesha, M.G.: Investigation on structural, optical and electrical properties of Zn doped indium oxide thin film for gamma dosimetry. Mater. Chem. Phys. 302, 127712 (2023)
47. Noori, F.T.M.: Optical and Structural Properties of (In2O3: ZnO: Au) Nanocomposite Thin Films Prepared by Spray Pyrolysis Method. Eng. Technol. J. 36, (2018)
48. Liu, D., Lei, W.W., Zou, B., Yu, S.D., Hao, J., Wang, K., Liu, B.B., Cui, Q.L., Zou, G.T.: High-pressure x-ray diffraction and Raman spectra study

of indium oxide. J. Appl. Phys. 104, 83506 (2008)

49. Gurlo, A., Kroll, P., Riedel, R.: Metastability of Corundum-Type In2O3. Chem. Eur. J. 14, 3306–3310 (2008)
50. Yang, J., Zhu, X., Yu, Q., He, M., Zhang, W., Mo, Z., Yuan, J., She, Y., Xu, H., Li, H.: Multidimensional In2O3/In2S3 heterojunction with lattice distortion for CO2 photoconversion. Chinese J. Catal. 43, 1286–1294 (2022)
51. Dasari, S.G., Nagaraju, P., Yelsani, V., Tirumala, S., MV, R.R.: Nanostructured indium oxide thin films as a room temperature toluene sensor. ACS omega. 6, 17442–17454 (2021)
52. Majumder, P., Gangopadhyay, R.: Evolution of graphene oxide (GO)-based nanohybrid materials with diverse compositions: an overview. RSC Adv. 12, 5686–5719 (2022)
53. Ghulam, A.N., Dos Santos, O.A.L., Hazeem, L., Pizzorno Backx, B., Bououdina, M., Bellucci, S.: Graphene Oxide (GO) Materials—Applications and Toxicity on Living Organisms and Environment. J. Funct. Biomater. 13, 77 (2022)
54. Goyal, D., Singh, A., Kumar, R.: Synthesis and characterization of ZnO/PMMA nanocomposites. Adv. Sci. Lett. 20, 1321–1324 (2014)
55. Hou, X., Yu, H., Guo, Y., Liang, X., Wang, S., Wang, L., Liu, X.: Polyethylene glycol/graphene oxide coated solid-phase microextraction fiber for analysis of phenols and phthalate esters coupled with gas chromatography. J. Sep. Sci. 38, 2700–2707 (2015)
56. Agarwal, S., Saraswat, Y.K., Saraswat, V.K.: Study of optical constants of ZnO dispersed PC/PMMA blend nanocomposites. Open Phys. J. 3, (2016)
57. Mohammed, M.K., Abass, K.H., Latif, D.M.A.: Improvement in Optical Properties of (PVA-PEG) Composites by the) 3 O 2 Antimony Trioxide (Sb Addition of.
58. Santhosh, G., Nayaka, G.P., Aranha, J.: Investigation on Electrical and

Dielectric Behaviour of Halloysite Nanotube Incorporated Polycarbonate Nanocomposite Films. Trans. Indian Inst. Met. 70, 549–555 (2017)

59. Hamood, F.J., Mohammed, M.K., Abass, K.H.: Study of AC electrical properties of (PVA-PEG-Sb2O3) Composites.
60. Evingür, G.A., Pekcan, Ö.: Optical energy band gap of PAAm-GO composites. Compos. Struct. 183, 212–215 (2018)
61. Liu, Y., Hou, C., Jiao, T., Song, J., Zhang, X., Xing, R., Zhou, J., Zhang, L., Peng, Q.: Self-assembled AgNP-containing nanocomposites constructed by electrospinning as efficient dye photocatalyst materials for wastewater treatment. Nanomaterials. 8, 35 (2018)
62. Patki, A.M., Maharanwar, A.A., Harde, S.K., Goyal, R.K.: Polycarbonate–hexagonal boron nitride composites with better dielectric properties for electronic applications. SN Appl. Sci. 1, 1–8 (2019)
63. Osma, B., Evingür, G.A., Pekcan, Ö.: Effect of temperature and graphene oxide on the swelling of PAAm-GO composite gels. Proc. World Congr. New Technol. 0, 6–10 (2019). https://doi.org/10.11159/icnfa19.146
64. Alver, Ü., Tascıoğlu, M.E., Güler, O., Aslan, M., Yazgan, A., Kaya, H., Duran, C., Çuvalcı, H., Bilgin, S.: Optical and dielectric properties of PMMA/α-Fe 2 O 3–ZnO nanocomposite films. J. Inorg. Organomet. Polym. Mater. 29, 1514–1522 (2019)
65. Guo, N., Liu, H., Fu, Y., Hu, J.: Preparation of Fe2O3 nanoparticles doped with In2O3 and photocatalytic degradation property for rhodamine B. Optik (Stuttg). 201, 163537 (2020)
66. Omar, A., Badry, R., Hegazy, M.A., Yahia, I.S., Elhaes, H., Zahran, H.Y., Ibrahim, M.A., Refaat, A.: Enhancing the optical properties of chitosan, carboxymethyl cellulose, sodium alginate modified with nano metal oxide and graphene oxide. Opt. Quantum Electron. 54, 806 (2022)
67. Ramalingam, G., Nagapandiselvi, P., Priya, A.K., Rajendran, S.: A review of graphene-based semiconductors for photocatalytic degradation of

pollutants in wastewater. Chemosphere. 134391 (2022)

68. Ramazanov, M.A., Shirinova, H.A., Nuriyeva, S.G., Jafarov, M.A., Hasanova, M.R.: Structure and optic properties of the nanocomposites based on polypropylene and amorphous silica nanoparticles. J. Thermoplast. Compos. Mater. 36, 1762–1774 (2023)
69. Al-Shawabkeh, A.F., Elimat, Z.M., Abushgair, K.N.: Effect of non-annealed and annealed ZnO on the optical properties of PVC/ZnO nanocomposite films. J. Thermoplast. Compos. Mater. 36, 899–915 (2023)
70. Yuan, F., Ouyang, C., Yang, M., Shi, W., Ren, W., Shen, Y., Wei, Y., Deng, X., Wang, X.: Regulating the Mechanical and Optical Properties of Polymer-based Nanocomposites by Sub-Nanowires. Angew. Chemie. 135, e202214571 (2023)
71. Badry, R., Hegazy, M.A., Yahia, I.S., Elhaes, H., Zahran, H.Y., Ibrahim, M.A.: Effect of Zinc Oxide on the Optical Properties of Polyvinyl Alcohol/Graphene Oxide Nanocomposite. Biointerface Res. Appl. Chem. 13, 39 (2023)
72. Li, F., Shen, T., Wang, C., Zhang, Y., Qi, J., Zhang, H.: Recent advances in strain-induced piezoelectric and piezoresistive effect-engineered 2D semiconductors for adaptive electronics and optoelectronics. Nano-Micro Lett. 12, 1–44 (2020)
73. Zanatta, A.R.: Revisiting the optical bandgap of semiconductors and the proposal of a unified methodology to its determination. Sci. Rep. 9, 11225 (2019)
74. Chteoui, R., Lotfy, K., El-Bary, A.A., Allan, M.M.: Hall Current Effect of Magnetic-Optical-Elastic-Thermal-Diffusive Non-Local Semiconductor Model during Electrons-Holes Excitation Processes. Crystals. 12, 1680 (2022)
75. Brem, S., Ekman, A., Christiansen, D., Katsch, F., Selig, M., Robert, C., Marie, X., Urbaszek, B., Knorr, A., Malic, E.: Phonon-assisted

photoluminescence from indirect excitons in monolayers of transition-metal dichalcogenides. Nano Lett. 20, 2849–2856 (2020)

76. Peng, X., Wei, Q., Copple, A.: Strain-engineered direct-indirect band gap transition and its mechanism in two-dimensional phosphorene. Phys. Rev. B. 90, 85402 (2014)
77. Ahmed, D.S., Al-Baidhani, M., Adil, H., Bufaroosha, M., Rashad, A.A., Zainulabdeen, K., Yousif, E.: Recent study of PF/ZnO nanocomposites: Synthesis, characterization and optical properties. Mater. Sci. Energy Technol. 6, 29–34 (2023)
78. Suresh, B., Ramachandran, S., Shanmugam, G.: Effect of Cerium dopant on third-order nonlinear optical properties of CdS/PEG self-standing nanocomposite films. Opt. Mater. (Amst). 135, 113299 (2023)
79. Sengwa, R.J., Dhatarwal, P.: Toward multifunctionality of PEO/PMMA/MMT hybrid polymer nanocomposites: Promising morphological, nanostructural, thermal, broadband dielectric, and optical properties. J. Phys. Chem. Solids. 166, 110708 (2022)
80. Vyshakh, K., Ramesan, M.T.: Enhanced optical properties, thermal transitions, temperature-dependent electrical properties and modelling studies of poly (diphenylamine)/NiO nanocomposites. J. Mater. Sci. 57, 18385–18405 (2022)
81. Ebrahimi Naghani, M., Neghabi, M., Zadsar, M., Abbastabar Ahangar, H.: Synthesis and characterization of linear/nonlinear optical properties of graphene oxide and reduced graphene oxide-based zinc oxide nanocomposite. Sci. Rep. 13, 1496 (2023)
82. Alrebdi, T.A., Ahmed, H.A., Alkallas, F.H., Mwafy, E.A., Trabelsi, A.B.G., Mostafa, A.M.: Structural, linear and nonlinear optical properties of NiO nanoparticles–multi-walled carbon nanotubes nanocomposite for optoelectronic applications. Radiat. Phys. Chem. 195, 110088 (2022)
83. Joshi, H., Annapoorni, S.: Tuning Optical Properties in Nanocomposites.

Int. J. Nanosci. 19, 1950026 (2020)

84. Sadek, E.M., Ahmed, S.M., El-Nashar, D.E., Mansour, N.A.: Effect of modified graphite nanoflakes on curing, mechanical and dielectric properties of nitrile rubber nanocomposites. Polym. Bull. 80, 847–863 (2023)
85. Mohamed, M.B., Abdel-Kader, M.H.: Effect of excess oxygen content within different nano-oxide additives on the structural and optical properties of PVA/PEG blend. Appl. Phys. A. 125, 1–11 (2019)
86. Kaur, D., Bharti, A., Sharma, T., Madhu, C.: Dielectric properties of ZnO-based nanocomposites and their potential applications. Int. J. Opt. 2021, 1–20 (2021)
87. Tao, Y., Yan, B., Fan, D., Zhang, N., Ma, S., Wang, L., Wu, Y., Wang, M., Zhao, J., Zhang, H.: Structural changes of starch subjected to microwave heating: A review from the perspective of dielectric properties. Trends Food Sci. Technol. 99, 593–607 (2020)
88. Tian, T., Scullion, D., Hughes, D., Li, L.H., Shih, C.-J., Coleman, J., Chhowalla, M., Santos, E.J.G.: Electronic polarizability as the fundamental variable in the dielectric properties of two-dimensional materials. Nano Lett. 20, 841–851 (2019)
89. Al-Muntaser, A.A., Pashameah, R.A., Saeed, A., Alwafi, R., Alzahrani, E., AlSubhi, S.A., Yassin, A.Y.: Boosting the optical, structural, electrical, and dielectric properties of polystyrene using a hybrid GNP/Cu nanofiller: Novel nanocomposites for energy storage applications. J. Mater. Sci. Mater. Electron. 34, 678 (2023)
90. Zhang, W., Jiang, M., Guan, F., Liu, S., Wang, L., Li, Y., Yue, D., Li, J., Liu, X., Feng, Y.: Influence of the acceptor-fillers on the dielectric properties of polyimide composites. Polym. Test. 108025 (2023)
91. Chien, H.-C., Lin, S.-Y., Chen, E.-C., Wu, T.-M.: Synthesis and dielectric properties of polyimide/hollow silica nanofiber composite. J. Mater. Sci.

Mater. Electron. 34, 64 (2023)

92. Liu, K., Zhang, H., Liu, C., Shi, L., Wang, X., Li, J., Liao, Y., Zhang, D.: Structure evolution of wolframite-type ZnZrC2O8 (C= Nb, Ta) ceramics in relation to microwave dielectric properties. J. Am. Ceram. Soc. 106, 1089–1101 (2023)
93. Arun, J., Nachiappan, S., Rangarajan, G., Alagappan, R.P., Gopinath, K.P., Lichtfouse, E.: Synthesis and application of titanium dioxide photocatalysis for energy, decontamination and viral disinfection: A review. Environ. Chem. Lett. 21, 339–362 (2023)
94. Alwera, S., Talismanov, V.S., Alwera, V., Domyati, D.: Synthesis and Characterization of Sn-Doped CeO2-Fe2O3 Nanocomposite and Application in Photocatalytic Degradation of Sudan I. Biointerface Res. Appl. Chem. 13, 179 (2023)
95. Elanthamilan, E., Elizabeth, I.B., Wang, S.-F., Lydia, I.S.: Strontium hexaferrite microspheres: synthesis, characterization and visible-light-driven photocatalytic activity towards the degradation of methylene blue dye. Opt. Mater. (Amst). 137, 113565 (2023)
96. Krishnan, M., Subramanian, H., Ramachandran, S.K., Muthukumarasamy, A., Ramadoss, D., Mahalingam, A., Rathinam, A.J., Dahms, H.-U., Hwang, J.-S.: Synthesis of Bimetallic BiPO4/ZnO Nanocomposite: Enhanced Photocatalytic Dye Degradation and Antibacterial Applications. Int. J. Mol. Sci. 24, 1947 (2023)
97. Ishfaq, M., Hassan, W., Sabir, M., Somaily, H.H., Hachim, S.K., Kadhim, Z.J., Lafta, H.A., Alnassar, Y.S., Rheima, A.M., Ejaz, S.R.: Wet-chemical synthesis of ZnO/CdO/CeO2 heterostructure: A novel material for environmental remediation application. Ceram. Int. 48, 34590–34601 (2022)
98. Ng, L.Y., Chua, H.S., Ng, C.Y.: Incorporation of graphene oxide-based nanocomposite in the polymeric membrane for water and wastewater

treatment: A review on recent development. J. Environ. Chem. Eng. 9, 105994 (2021)

99. Hussien, H.A.J., Kadhim, R.G., Hashim, A.: Investigating the low cost photodegradation performance against organic Pollutants using CeO2/MnO2/polymer blend nanostructures. Opt. Quantum Electron. 54, 704 (2022)
100. Pogrebnjak, A.D., Kong, C.-H., Webster, R.F., Tilley, R.D., Takeda, Y., Oyoshi, K., Bondar, O. V, Buranich, V. V, Konstantinov, S. V, Baimoldanova, L.S.: Antibacterial effect of Au implantation in ductile nanocomposite multilayer (TiAlSiY) N/CrN coatings. ACS Appl. Mater. Interfaces. 11, 48540–48550 (2019)
101. Nirmala, M.J., Durai, L., Gopakumar, V., Nagarajan, R.: Anticancer and antibacterial effects of a clove bud essential oil-based nanoscale emulsion system. Int. J. Nanomedicine. 6439–6450 (2019)
102. Canaparo, R., Foglietta, F., Giuntini, F., Della Pepa, C., Dosio, F., Serpe, L.: Recent developments in antibacterial therapy: Focus on stimuli-responsive drug-delivery systems and therapeutic nanoparticles. Molecules. 24, 1991 (2019)
103. Alavi, M., Thomas, S., Sreedharan, M.: Modification of silica nanoparticles for antibacterial activities: mechanism of action. Micro Nano Bio Asp. 1, 49–58 (2022)
104. Tabandeh-Khorshid, M., Kumar, A., Omrani, E., Kim, C., Rohatgi, P.: Synthesis, characterization, and properties of graphene reinforced metal-matrix nanocomposites. Compos. Part B Eng. 183, 107664 (2020)
105. Nepal, D., Kang, S., Adstedt, K.M., Kanhaiya, K., Bockstaller, M.R., Brinson, L.C., Buehler, M.J., Coveney, P. V, Dayal, K., El-Awady, J.A.: Hierarchically structured bioinspired nanocomposites. Nat. Mater. 22, 18–35 (2023)
106. Duan, X., Siew, W.H., Given, M., Liggat, J., He, J.: Effect of different

surface treatment agents on the physical chemistry and electrical properties of polyethylene nano-alumina nanocomposites. High Volt. 5, 397–402 (2020)

107. Zhao, J., Ge, S., Pan, D., Pan, Y., Murugadoss, V., Li, R., Xie, W., Lu, Y., Wu, T., Wujcik, E.K.: Microwave hydrothermal synthesis of In2O3-ZnO nanocomposites and their enhanced photoelectrochemical properties. J. Electrochem. Soc. 166, H3074–H3083 (2019)
108. Zhu, Y., Iroh, J.O., Rajagopolan, R., Aykanat, A., Vaia, R.: Optimizing the synthesis and thermal properties of conducting polymer–montmorillonite clay nanocomposites. Energies. 15, 1291 (2022)
109. Chin, H.S., Cheong, K.Y., Razak, K.A.: Review on oxides of antimony nanoparticles: synthesis, properties, and applications. J. Mater. Sci. 45, 5993–6008 (2010)
110. Nistor, M., Seiler, W., Hebert, C., Matei, E., Perrière, J.: Effects of substrate and ambient gas on epitaxial growth indium oxide thin films. Appl. Surf. Sci. 307, 455–460 (2014)
111. Ain, Q.T., Haq, S.H., Alshammari, A., Al-Mutlaq, M.A., Anjum, M.N.: The systemic effect of PEG-nGO-induced oxidative stress in vivo in a rodent model. Beilstein J Nanotechnol 10: 901–911, (2019)
112. Hajipour, P., Bahrami, A., Eslami, A., Hosseini-Abari, A.: Chemical bath synthesis of CuO-GO-Ag nanocomposites with enhanced antibacterial properties. J. Alloys Compd. 821, 153456 (2020)
113. Mwafy, E.A., Hasanin, M.S., Mostafa, A.M.: Cadmium oxide/TEMPO-oxidized cellulose nanocomposites produced by pulsed laser ablation in liquid environment: synthesis, characterization, and antimicrobial activity. Opt. Laser Technol. 120, 105744 (2019)
114. Bashir, B., Khalid, M.U., Aadil, M., Zulfiqar, S., Warsi, M.F., Agboola, P.O., Shakir, I.: CuxNi1-xO nanostructures and their nanocomposites with reduced graphene oxide: synthesis, characterization, and photocatalytic

applications. Ceram. Int. 47, 3603–3613 (2021)

115. Turki Jalil, A., Hussain Dilfy, S., Oudah Meza, S., Aravindhan, S., M Kadhim, M., M Aljeboree, A.: CuO/ZrO2 nanocomposites: facile synthesis, characterization and photocatalytic degradation of tetracycline antibiotic. J. Nanostructures. 11, 333–346 (2021)
116. Sabur, D.A., Habeeb, M.A., Hashim, A.: Fabrication and Tailoring the Structural and Dielectric Characteristics of GO/Sb2O3/PMMA/PC Quaternary Nanostructures For Solid State Electronics Nanodevices. Phys. Chem. Solid State. 24, 173–180 (2023)
117. Fahad, N.K., Sabry, R.S.: Study of some mechanical and physical properties of PMMA reinforced with (TiO2 and TiO2-GO) nanocomposite for denture bases. J. Polym. Res. 29, 439 (2022)
118. Kaur, R., Singh, K.P., Tripathi, S.K.: Electrical, linear and non-linear optical properties of MoSe2/PVA nanocomposites as charge trapping elements for memory device applications. J. Alloys Compd. 905, 164103 (2022)
119. Kumar, S., Choudhary, R.B.: Influence of MnO2 nanoparticles on the optical properties of polypyrrole matrix. Mater. Sci. Semicond. Process. 139, 106322 (2022)
120. Alzahrani, H.S., Al-Sulami, A.I., Alsulami, Q.A., Rajeh, A.: A systematic study of structural, conductivity, linear, and nonlinear optical properties of PEO/PVA-MWCNTs/ZnO nanocomposites films for optoelectronic applications. Opt. Mater. (Amst). 133, 112900 (2022)
121. Rahman, M.T., Hoque, M.A., Rahman, G.T., Gafur, M.A., Khan, R.A., Hossain, M.K.: Study on the mechanical, electrical and optical properties of metal-oxide nanoparticles dispersed unsaturated polyester resin nanocomposites. Results Phys. 13, 102264 (2019)
122. Soliman, T.S., Vshivkov, S.A.: Effect of Fe nanoparticles on the structure and optical properties of polyvinyl alcohol nanocomposite films. J. Non.

Cryst. Solids. 519, 119452 (2019)

123. Aly, A.H., Malek, C., Elsayed, H.A.: Transmittance properties of a quasi-periodic one-dimensional photonic crystals that incorporate nanocomposite material. Int. J. Mod. Phys. B. 32, 1850220 (2018)
124. Kassab, Z., Boujemaoui, A., Ben Youcef, H., Hajlane, A., Hannache, H., El Achaby, M.: Production of cellulose nanofibrils from alfa fibers and its nanoreinforcement potential in polymer nanocomposites. Cellulose. 26, 9567–9581 (2019)
125. Mergen, Ö.B., Arda, E.: Determination of optical band gap energies of CS/MWCNT bio-nanocomposites by Tauc and ASF methods. Synth. Met. 269, 116539 (2020)
126. Jebur, Q., Hashim, A., Habeeb, M.: Fabrication, Structural and Optical properties for (Polyvinyl Alcohol–Polyethylene Oxide–Iron Oxide) Nanocomposites. Egypt. J. Chem. 63, 611–623 (2020)
127. Pepe, Y., Karatay, A., Donar, Y.O., Sınağ, A., Unver, H., Elmali, A.: Tuning the energy bandgap and nonlinear absorption coefficients of CdO nanocomposite films with doping and annealing process. Opt. Mater. (Amst). 103, 109880 (2020)
128. Abed, A.N., Abed, R.N.: Characterization effect of copper oxide and cobalt oxide nanocomposite on poly (vinyl chloride) doping process for solar energy applications. Prog. Color. Color. Coatings. 15, 235–241 (2022)
129. Mahdi, S.M., Habeeb, M.A.: Synthesis and augmented optical characteristics of PEO–PVA–SrTiO3–NiO hybrid nanocomposites for optoelectronics and antibacterial applications. Opt. Quantum Electron. 54, 1–17 (2022)
130. Zaidi, B., Smida, N., Althobaiti, M.G., Aldajani, A.G., Almdhaibri, S.D.: Polymer/Carbon Nanotube Based Nanocomposites for Photovoltaic Application: Functionalization, Structural, and Optical Properties.

Polymers (Basel). 14, 1093 (2022)

131. Donya, H., Taha, T.A., Alruwaili, A., Tomsah, I.B.I., Ibrahim, M.: Micro-structure and optical spectroscopy of PVA/iron oxide polymer nanocomposites. J. Mater. Res. Technol. 9, 9189–9194 (2020)
132. Abouhaswa, A.S., Taha, T.A.: Tailoring the optical and dielectric properties of PVC/CuO nanocomposites. Polym. Bull. 77, 6005–6016 (2020)
133. Liu, S., Islam, M.D., Ku, Z., Boyd, D.A., Zhong, Y., Urbas, A.M., Smith, E., Derov, J., Nguyen, V.Q., Kim, W.: Novel computational design of high refractive index nanocomposites and effective refractive index tuning based on nanoparticle morphology effect. Compos. Part B Eng. 223, 109128 (2021)
134. Tamta, S., Dahiya, A., Kumar, P.S.: Modified Stöber synthesis of SiO2@ Ag nanocomposites and their enhanced refractive index sensing applications. Phys. B Condens. Matter. 638, 413971 (2022)
135. Bin-Dahman, O.A., Rahaman, M., Khastgir, D., Al-Harthi, M.A.: Electrical and dielectric properties of poly (vinyl alcohol)/starch/graphene nanocomposites. Can. J. Chem. Eng. 96, 903–911 (2018)
136. Jebur, Q.M., Hashim, A., Habeeb, M.A.: Structural, electrical and optical properties for (polyvinyl alcohol–polyethylene oxide–magnesium oxide) nanocomposites for optoelectronics applications. Trans. Electr. Electron. Mater. 20, 334–343 (2019)
137. Arya, A., Sadiq, M., Sharma, A.L.: Effect of variation of different nanofillers on structural, electrical, dielectric, and transport properties of blend polymer nanocomposites. Ionics (Kiel). 24, 2295–2319 (2018)
138. Zhang, B., Chen, X., Lu, W., Zhang, Q.M., Bernholc, J.: Morphology-induced dielectric enhancement in polymer nanocomposites. Nanoscale. 13, 10933–10942 (2021)
139. Xia, X., Wang, Y., Zhong, Z., Weng, G.J.: A frequency-dependent theory

of electrical conductivity and dielectric permittivity for graphene-polymer nanocomposites. Carbon N. Y. 111, 221–230 (2017)

140. Xia, X., Zhong, Z., Weng, G.J.: Maxwell–Wagner–Sillars mechanism in the frequency dependence of electrical conductivity and dielectric permittivity of graphene-polymer nanocomposites. Mech. Mater. 109, 42–50 (2017)
141. Hashim, A., Hadi, Q.: Synthesis of novel (polymer blend-ceramics) nanocomposites: structural, optical and electrical properties for humidity sensors. J. Inorg. Organomet. Polym. Mater. 28, 1394–1401 (2018)
142. Zeraati, A.S., Arjmand, M., Sundararaj, U.: Silver nanowire/MnO2 nanowire hybrid polymer nanocomposites: materials with high dielectric permittivity and low dielectric loss. ACS Appl. Mater. Interfaces. 9, 14328–14336 (2017)
143. Chen, J., Wang, X., Yu, X., Yao, L., Duan, Z., Fan, Y., Jiang, Y., Zhou, Y., Pan, Z.: High dielectric constant and low dielectric loss poly (vinylidene fluoride) nanocomposites via a small loading of two-dimensional Bi 2 Te 3@ Al 2 O 3 hexagonal nanoplates. J. Mater. Chem. C. 6, 271–279 (2018)
144. Kumar, S., Supriya, S., Kar, M.: Enhancement of dielectric constant in polymer-ceramic nanocomposite for flexible electronics and energy storage applications. Compos. Sci. Technol. 157, 48–56 (2018)
145. Ravindran, A.R., Feng, C., Huang, S., Wang, Y., Zhao, Z., Yang, J.: Effects of graphene nanoplatelet size and surface area on the AC electrical conductivity and dielectric constant of epoxy nanocomposites. Polymers (Basel). 10, 477 (2018)
146. Mirkhani, S.A., Shayesteh Zeraati, A., Aliabadian, E., Naguib, M., Sundararaj, U.: High dielectric constant and low dielectric loss via poly (vinyl alcohol)/Ti3C2T x MXene nanocomposites. ACS Appl. Mater. Interfaces. 11, 18599–18608 (2019)

147. Thakur, Y., Zhang, T., Iacob, C., Yang, T., Bernholc, J., Chen, L.Q., Runt, J., Zhang, Q.M.: Enhancement of the dielectric response in polymer nanocomposites with low dielectric constant fillers. Nanoscale. 9, 10992–10997 (2017)
148. Aguilar-Bolados, H., Lopez-Manchado, M.A., Brasero, J., Avilés, F., Yazdani-Pedram, M.: Effect of the morphology of thermally reduced graphite oxide on the mechanical and electrical properties of natural rubber nanocomposites. Compos. Part B Eng. 87, 350–356 (2016)
149. Hemalatha, K.S., Sriprakash, G., Ambika Prasad, M.V.N., Damle, R., Rukmani, K.: Temperature dependent dielectric and conductivity studies of polyvinyl alcohol-ZnO nanocomposite films by impedance spectroscopy. J. Appl. Phys. 118, 154103 (2015)
150. Ladani, R.B., Wu, S., Kinloch, A.J., Ghorbani, K., Zhang, J., Mouritz, A.P., Wang, C.H.: Improving the toughness and electrical conductivity of epoxy nanocomposites by using aligned carbon nanofibres. Compos. Sci. Technol. 117, 146–158 (2015)
151. Singh, P., Shandilya, P., Raizada, P., Sudhaik, A., Rahmani-Sani, A., Hosseini-Bandegharaei, A.: Review on various strategies for enhancing photocatalytic activity of graphene based nanocomposites for water purification. Arab. J. Chem. 13, 3498–3520 (2020)
152. Taufique, M.F.N., Haque, A., Karnati, P., Ghosh, K.: ZnO–CuO nanocomposites with improved photocatalytic activity for environmental and energy applications. J. Electron. Mater. 47, 6731–6745 (2018)
153. Rana, P.S.: Structural, optical, electrical, and photocatalytic application of NiFe2O4@ NiO nanocomposites for methylene blue dye. Ceram. Int. 49, 13520–13530 (2023)
154. Osgouei, M.S., Khatamian, M., Kakili, H.: Improved visible-light photocatalytic activity of Mn3O4-based nanocomposites in removal of methyl orange. Mater. Chem. Phys. 239, 122108 (2020)

155. Zinatloo-Ajabshir, S., Mortazavi-Derazkola, S., Salavati-Niasari, M.: Nd2O3-SiO2 nanocomposites: a simple sonochemical preparation, characterization and photocatalytic activity. Ultrason. Sonochem. 42, 171–182 (2018)
156. Munawar, T., Iqbal, F., Yasmeen, S., Mahmood, K., Hussain, A.: Multi metal oxide NiO-CdO-ZnO nanocomposite–synthesis, structural, optical, electrical properties and enhanced sunlight driven photocatalytic activity. Ceram. Int. 46, 2421–2437 (2020)
157. Al-Shawi, S.G., Andreevna Alekhina, N., Aravindhan, S., Thangavelu, L., Elena, A., Viktorovna Kartamysheva, N., Rafkatovna Zakieva, R.: Synthesis of NiO nanoparticles and sulfur, and nitrogen co doped-graphene quantum dots/nio nanocomposites for antibacterial application. J. Nanostructures. 11, 181–188 (2021)
158. Preethi, S., Abarna, K., Nithyasri, M., Kishore, P., Deepika, K., Ranjithkumar, R., Bhuvaneshwari, V., Bharathi, D.: Synthesis and characterization of chitosan/zinc oxide nanocomposite for antibacterial activity onto cotton fabrics and dye degradation applications. Int. J. Biol. Macromol. 164, 2779–2787 (2020)
159. Deshmukh, S.P., Dhodamani, A.G., Patil, S.M., Mullani, S.B., More, K. V, Delekar, S.D.: Interfacially interactive ternary silver-supported polyaniline/multiwalled carbon nanotube nanocomposites for catalytic and antibacterial activity. ACS omega. 5, 219–227 (2019)
160. Xie, Y.-Y., Hu, X.-H., Zhang, Y.-W., Wahid, F., Chu, L.-Q., Jia, S.-R., Zhong, C.: Development and antibacterial activities of bacterial cellulose/graphene oxide-CuO nanocomposite films. Carbohydr. Polym. 229, 115456 (2020)
161. Merino, D., Gutiérrez, T.J., Mansilla, A.Y., Casalongué, C.A., Alvarez, V.A.: Critical evaluation of starch-based antibacterial nanocomposites as agricultural mulch films: Study on their interactions with water and light.

ACS Sustain. Chem. Eng. 6, 15662–15672 (2018)

الخلاصة

تضمنت هذه الدراسة تحضير نوعين من المتراكبات النانوية (PMMA-PC-In_2O_3-GO) and (PMMA-PC-Sb_2O_3-GO). حضر الخليط البوليمري من (البولي ميثيل ميثاكريلات والبولي كربونات) وقد تم اضافة المواد النانوية من اكسيد الانديوم الثلاثي واوكسيد الانتيمون الثلاثي واكسيد الكرافين بطريقة صب المحلول و بنسب وزنية مختلفة من المواد المضافة. كما تم دراسة تأثير المواد النانوية المضافة على الخصائص التركيبية والكهربائية والبصرية للمركبات النانوية ، بالإضافة إلى نشاطها التحفيزي الضوئي والمضاد للبكتيريا. وقد اظهرت صورالمجهر الضوئي وصور الماسح الالكتروني ان اكاسيد الانديوم الثلاثي والانتيمون الثلاثي والكرافين النانوية تتوزع بشكل متجانس في الخليط البوليمري .

وضحت أنماط XRD للجسيمات النانوية النقية Sb_2O_3 و In_2O_3 و GO ثلاث قمم قريبة من 13.70 درجة و 26 درجة و 30.8 درجة والتي تتوافق مع (111) و (222) و (400) انعكاسات لـ (Sb_2O_3) على التوالي ، وثلاث قمم تقابل اتجاهات (100) و (400) و (440) من الهيكل البلوري المكعب In_2O_3 والذي يتوافق مع المواضع ^{o} 29.9 و $^{\circ}$34.1 و $^{\circ}$47.8 على التوالي. يُظهر نمط XRD لأكسيد الجرافين ذروة عند θ = 10.12 درجة (تباعد d يبلغ 8.9 Å) .

كما اظهرت منحيات تحويلات فورير للاشعة تحت الحمراء انه لا يوجد تفاعل كيميائي بين الخليط البوليمري والجسيمات النانوية المضافة. بينما وضحت النتائج التجريبية للخصائص البصرية للمتراكبات النانوية زيادة الامتصاصية ، ومعامل الامتصاص ، ومعامل الانقراض ، ومعامل الانكسار ، وثوابت العزل الحقيقي مع زيادة تراكيز الجسيمات النانوية ، بينما تقل النفاذية وفجوة الطاقة للانتقال غير المباشر(المسموح والممنوع) بزيادة تركيز الجسيمات النانوية . و تم دراسة الخواص الكهربائية المتناوبة في مدى ترددات (100Hz-5MHz) حيث اظهرت النتائج التجريبية ازدياد كل من ثابت العزل وفقدان العزل الكهربائي والتوصيلية الكهربائية المتناوبة للخليط البوليمري (PMMA-PC) بزيادة تراكيز الجسيمات النانوية.

وبينت النتائج التجريبية للتحفيز الضوئي ان هذه المتراكبات النانوية (PMMA-PC/In_2O_3-GO) و

(PMMA-PC/Sb_2O_3-GO) لها كفاءة كبيرة كمحفزات ضوئية لانحلال صبغة المثيل البرتقالي MO ، ويمكن تحسين نشاطها التحفيزي الضوئي عن طريق التحكم في تركيز الجسيمات النانوية, حيث ينخفض امتصاص محلول صبغة MO مع زيادة وقت التشعيع ، مما يشير إلى أن نشاط التحفيز الضوئي للمركبات النانوية يتزايد بزيادة تراكيز المواد النانوية. ويرجع ذلك إلى زيادة نسبة التحلل الضوئي لصبغة

MO ، والتي تحدث نتيجة تفاعل الذي يحدث اثناء التحفيز الضوئي . وقد تم دراسة عمر النصف لتحلل صبغة الميثيل البرتقالي ووجد ان عمر النصف لتحلل الصبغة عند الدقيقة 38 من بدء التشعيع . تم تحليل حركية انحلال صبغة برتقال الميثيل (MO) باستخدام نموذج Langmuir-Hinshelwood ،كمااختبرت المتراكبات النانوية (PMMA-PC/In_2O_3-GO),(PMMA-PC/Sb_2O_3-GO) كمضادات للجراثيم ضد البكتيريا موجبة الجرام(المكورات العنقودية الذهبية) وسالبة الجرام (الاشريشيا) حيث زادت منطقة التثبيط مع زيادة تركيز الجسيمات النانوية.

جمهورية العراق
وزارة التعليم العالي والبحث العلمي
جامعة بابل – كلية التربية للعلوم الصرفة
قسم الفيزياء

تصنيع وتحليلات متراكبات نانوية جديدة تستخدم في التطبيقات البيئية الاحيائية

اطروحة مقدمة
إلى مجلس كلية التربية للعلوم الصرفة في جامعة بابل وهي جزء من متطلبات
نيل درجة دكتوراه فلسفة في التربية/ الفيزياء

من قبل
ضي علي صبر علي
بكالوريوس تربية (فيزياء)
جامعة بابل 2009 م
ماجستير علوم فيزياء
جامعة بوخارست 2018 م

بإشراف

أ.د. مجيد علي حبيب **أ.د. احمد هاشم محيسن**

١٤٤٥هـ ٢٠٢٣ م